Report
P-17-03
February 2018

Modelling the interaction between engineered and natural barriers

Task 8 of SKB Task Forces EBS and GWFTS

Daniel Malmberg

Mattias Åkesson

SVENSK KÄRNBRÄNSLEHANTERING AB

SWEDISH NUCLEAR FUEL
AND WASTE MANAGEMENT CO

Box 3091, SE-169 03 Solna
Phone +46 8 459 84 00
skb.se

SVENSK KÄRNBRÄNSLEHANTERING

ISSN 1651-4416
SKB P-17-03
ID 1587141

February 2018

Modelling the interaction between engineered and natural barriers

Task 8 of SKB Task Forces EBS and GWFTS

Daniel Malmberg, Mattias Åkesson
Clay Technology AB

Abstract

In this report the modelling of 1) the BRIE water-uptake-laboratory experiment and 2) the BRIE field experiment, carried out within SKBs Task Force on Engineered Barrier Systems (SKB TF-EBS), is described. Both experiments were modelled using the FEM code Code_Bright. The main goals were to verify our hydraulic model of the bentonite clay used in the BRIE experiment, as well as to develop and test our conceptualization of the water-transport properties of the host rock near the BRIE boreholes.

The water-uptake experiment modelled consisted of a single, confined bentonite block, which was allowed to hydrate via free access to water at the outer vertical boundary (the surrounding steel container was not included in the model). The modelling results showed that the hydraulic evolution was well reproduced and that the parameters suggested in the task definition provided a good representation of the behavior of the used bentonite blocks.

The BRIE field experiment was modelled in full 3D using two sets of geometries: i) a large-scale geometry with both the TASO and TASD tunnels included, as well as a large volume of the surrounding host rock and ii) a local-scale geometry with the borehole and just the nearby rock included. Using Code_Bright it is not possible to implement a discrete fracture network, and as such the transport properties of the rock around the experimental boreholes had to be handled in a simplified way. Except just around the boreholes the host rock was treated as a homogeneous material with an effective hydraulic conductivity, which was set so as to represent the heterogeneous fracture and matrix flow in a homogeneous flow with the same magnitude. Only just around the boreholes was the host rock treated in a more detailed way; with a cylinder of low-permeability rock matrix intersected by fractures. The geometry and transport properties of these fractures were taken from the characterization done in the field prior to installation of the bentonite and in later models calibrated to reproduce the relative-humidity evolution and measured water-content data after dismantling.

The results of the modelling of the field experiment showed that with the characterization data available to us in Task 8D it was possible to predict the evolution in the field reasonably well in one of the boreholes (borehole 17), while the prediction of the evolution in borehole 18 was rather poor.

Using updated models, calibrated both during the experiment from relative-humidity data, as well as after dismantling using water content data and updated fracture geometries, it was possible to achieve an excellent match between modelled and experimental data for borehole 17 and an acceptable match in borehole 18.

Sammanfattning

I denna rapport beskrivs modellering av BRIE experimentet i Äspö HRL; dels vattenupptagsförsöket och dels själva fältförsöket. Modelleringen utfördes inom SKB:s ”Task Force on Engineered Barrier Systems” (SKB TF EBS) med hjälp av finita elementkoden Code_Bright. Huvudmålen med modelleringen var att 1) verifiera vår hydrauliska materialmodell av bentonitlera samt 2) att utveckla och testa vår konceptualisering av vattentransportsegenskaper hos berget i nära anslutning till BRIE experimentet. Syftet med dessa mål var att förbättra vår förståelse av bevätningsprocessen i det planerade slutförvaret i Forsmark.

Vattenupptagsförsöket bestod av enskilda bentonitblock (cylinderformade) inneslutna i metallbehållare. Bentonitblocken hade fri tillgång till vatten via filter som omgav den yttre randen, varken filtren eller metallbehållarna var dock inkluderade i modellen. Resultaten från modelleringen av försöket överensstämde mycket väl med de experimentella resultaten, vilket visade att parametrarna angivna i taskdefinitionen gav en god representation av de använda bentonitblocken.

Fältexperimentet modellerades med två olika tre-dimensionella geometrier: i) en storskalig geometri som inkluderade både TASO och TASD tunnlarna samt en stor volym av omgivande berg, samt ii) en småskalig geometri där enbart själva borrhålet och det närliggande berget var inkluderade. Modelleringsverktyget som användes (Code_Bright) kan inte inkludera diskreta spricknätverk, varför det inte var möjligt att modellera vattentransport genom sprickor i berget över stora avstånd. Istället modellerades berget som ett homogent material med en effektiv hydraulisk konduktivitet överallt förutom närmast borrhålen. Värdet på den effektiva hydrauliska konduktiviteten sattes så att flödet genom berget var ungefär lika stort som flödet genom spricknätverket och bergmatrisen. Endast i en liten volym omkring borrhålet användes en mer detaljerad representation av berget: en cylinderformad bergsvolym med samma egenskaper som bergmatrisen omgav deponeringshålet och matrisvolymen genomskars av ett antal diskreta sprickor. Sprickornas egenskaper kalibrerades i de tidiga modellerna från de uppmätta egenskaperna i fältet och i senare modeller för att så gott som möjligt efterskapa det uppmätta fuktupptaget i bentoniten.

Med hjälp av den karakteriseringsdata som fanns tillgänglig visade modellresultaten att det var möjligt att prediktera utvecklingen relativt bra i ett av borrhålen (nr 17), medan utvecklingen i det andra borrhålet (nr 18) skiljde sig signifikant från modellprediktionen.

Med uppdaterade modeller, förfinade med hjälp av dels sensorsdata (relativ fuktighet) och dels brytningsdata från fältexperimentet (vattenkvoter och uppdaterade sprickgeometrier), var det möjligt att uppnå en mycket god matchning mellan den modellerade utvecklingen och den uppmätta i fältexperimentet i borrhål 17 och en acceptabel matchning i borrhål 18.

Contents

1 Introduction

Clay Technology AB is a consulting agency (whose primary contractor is Svensk Kärnbränslehantering AB; SKB) that primarily specializes in studying the behavior of the engineered bentonite barrier in the repository design for spent nuclear fuel in Sweden. The BRIE experiment, which is funded by SKB, was made into a modelling task in the SKB Äspö Task Force on Engineered Barrier Systems (SKB TF EBS) which Clay Technology has been taken part of since its formation. Modelling the BRIE experiment (both the laboratory and in-situ tests) can provide us with valuable information with respect to how the bentonite behaves when subjected to natural wetting from the rock. The experiment is considerably easier to model than other in-situ experiments with natural wetting, such as for example the Prototype Repository, as it is isothermal and since the experiment has been constructed so as to minimize the influence of mechanical processes. Furthermore, the modelling exercises has given us the change to develop and test a, with the numerical tool at hand, numerically feasible conceptualization of the host rock which mimics the natural wetting conditions that can be expected in the field.

The main goals of the modelling is 1) to verify and, if needed, improve the material models used to simulate bentonite using our primary numerical tool, Code_Bright, and 2) to develop our ability to simulate natural wetting from the rock.

The modelling presented here concerns Task 8a (including sensitivity analyses), Task 8c/d/f as well as the BRIE water-uptake experiment. The modelling of Task 8 did not follow the task definition strictly, as 1) with our simplified representation of the rock material we were not able to predict the deposition-borehole inflows, and 2) as Clay Technology was in part responsible for the installation and excavation of BRIE, additional information from the field experiment was used in the modelling such that the results could provide help in the decision making regarding when to dismantle the field experiment.

2 Model setup

2.1 Conceptual model of the system

In order to understand how we construct our models it is helpful to start with a brief overview of our understanding of the physical system. It is useful to first (briefly) describe our current understanding of the true physical system which is to be modelled (True system). Thereafter we describe a hypothetical perfect conceptualization of this system – the reified model. Finally the actual model conceptualization is discussed, and how it differs to the reified model.

A brief description of the True system (regarding bentonite and rock, respectively) is given in Table 2-1, with focus on *structures, forces* and *potentials*, thus emphasizing *fundamental processes*. Distinctions are made between: structure (macroscopic), pore space (i.e. microscopic structure), water-holding capacity, water saturated flow and unsaturated flow. As the rock and bentonite are two fundamentally different materials, they are discussed separately. Our description of the true system is here limited to the description in Table 2-1.

Table 2-1. True system.

	Bentonite	**Rock**
Structure	• Essentially homogenous.	• Matrix intersected by a network of fractures. • The fracture network at Äspö show fractal properties on the 10 m scale and above (Darcel 2003). • Fracture transmissivity-aperture relation is scale dependent (i.e. fractures with high transmissivity are larger and rarer than low-transmissivity fractures).
Pore space	• Water-filled interlayer. • Air-filled voids between grains (unsaturated conditions).	• Voids between grains (?) • Voids in fractures.
Water-holding capacity	• Repulsive (osmotic) forces.[1] • Attractive (e.g. van der Waals) forces.[1] • Major hysteretic effects.	• Capillary forces.
Saturated flow	• Gradients in chemical potential[2] • Due to gradients in interlayer distance and counter-ion concentration (pressure gradients insignificant).	• Gradients in pore pressure.
Unsaturated flow	• Gradients in chemical potential (liquid flow) and vapor density (vapor flow). • Due to gradients in interlayer distance and counter-ion concentration (pressure gradients insignificant).	• Gradients in capillary pressure and vapor density.

[1] Hedström et al. (2016).
[2] Birgersson and Karnland (2014).

Corresponding descriptions of a Reified and an Actual model are shown in Table 2-2 and Table 2-3, respectively. Both are focused on *properties* which can be determined in independent experiments. The reified models is formulated as *physically consistent* as possible, while the formulations used when discussing the actual model was chosen so as to *facilitate an implementation in the numerical tool* at hand. When discussing the reified and actual model, distinctions are made for the following properties: structure, porosity, water-retention curve, intrinsic permeability and relative permeability. In Figure 2-1 a schematic illustration of how the description of the rock material varies between the True system and the Reified and Actual models is shown. It is beyond the scope of this report to discuss the True system beyond what is state in Table 2-1, however, the Reified and Actual models are discussed in some detail in the following sections.

Table 2-2. Reified model.

	Bentonite	Rock
Structure	- Including gap and mechanics.	- Matrix and resolved fracture network in an zone of influence around the borehole. - Homogenized treated rock outside zone.
Porosity	- Evaluated from dry density. - ~ 40 % - Influenced by mechanics.	- Evaluated from drying measurements. - ~ 0.3 %
Water-retention curve	- $s = s_{free}(w,dw/dt) - p$ - Free swelling curve evaluated from jar tests.	- Van Genuchten curve evaluated from BRIE lab tests.
Intrinsic permeability	- $k = f(n)$ - Evaluated from hydraulic conductivity. measurements and water uptake tests.	- Matrix permeability evaluated from BRIE lab tests. - Fracture transmissivities, evaluated from bore hole inflow. - Equivalent permeability for homogenized rock evaluated from TASO inflow and pore pressure.
Relative permeability	- $k_r = f(S_l)$ - Evaluated from water uptake tests.	- $k_r = f(S_l)$ - Evaluated from vapor permeability measurements.

Table 2-3. Actual model.

	Bentonite	Rock
Structure	- Homogenous.	- Matrix and a few resolved fractures in a high-resolution cylinder around borehole. - Homogenized treated rock outside zone.
Porosity	- Evaluated from dry density. - 44 %	- Evaluated from drying measurements. - 0.3 %
Water-retention curve	- Van Genuchten curve. - Evaluated from jar tests and supported by BRIE WUT.	- Van Genuchten curve evaluated from BRIE lab tests.
Intrinsic permeability	- $k = 6.4 \times 10^{-21}\ m^2$ - Evaluated from hydraulic conductivity measurements and supported by BRIE WUT.	- Matrix permeability evaluated from BRIE lab tests. - Fracture transmissivities, evaluated from bore hole inflow. - Equivalent permeability for homogenized rock evaluated from Prototype inflow and pore pressure.
Relative permeability	- $k_r = S_l^3$ - Supported by BRIE WUT.	- Van Genuchten curve. - Evaluated from Grimsel tests.

2.1.1 Reified model

The description of the Reified model basically incorporate properties which can be determined in independent experiments and are formulated as physically consistent as possible, see Table 2-2. When constructing the reified model our goal was to construct a model which incorporates all the known properties of the modelled site (i.e. a deterministic model), keeping the introduction of features which cannot be directly characterized (such as the network of fractures which do not intersect the borehole) and hence are only known statistically, to a minimum.

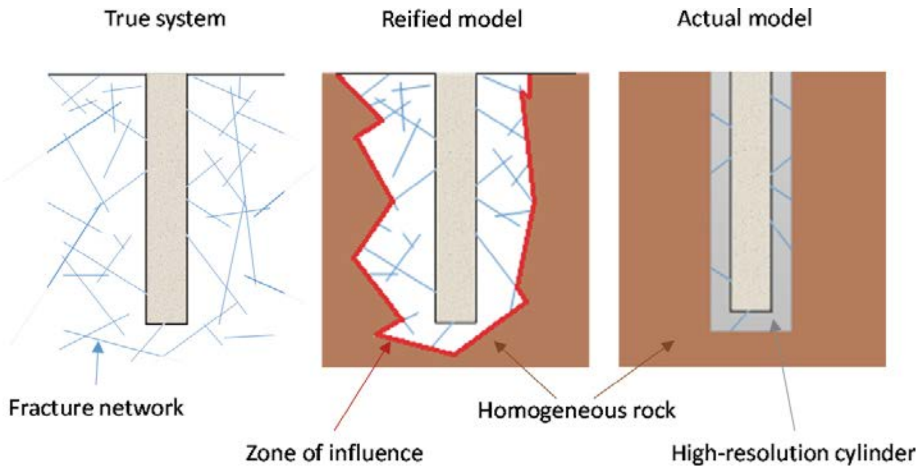

Figure 2-1. *Schematic overview of the difference between the True system, Reified model and Actual model, where only the different conceptualizations of the rock has been illustrated. In the true system the water transport in the rock takes place in the fracture network. However, in the Reified model only fractures within the zone of influence is kept, while the rock outside is treated as a homogeneous material (see* ***Hydraulic properties of the rock*** *in this section). The zone of influence is the volume of rock around a given bore/deposition hole within which the liquid pressure/liquid flow is perturbed. The exact size of this volume is of course highly situation dependent; for example, more fractures would in general lead to a smaller zone of influence. Also the flow situation in the borehole has an effect: a material with high suction could lead to a change in the size of the zone of influence. Hence, it is reasonable to assume that in the reified model, the size of the zone of influence is time dependent, and is presumably at its largest some time after installation of the bentonite. The actual model schematically depicts how we have implemented this conceptual model into our numerical solver (Code_Bright), with the zone of influence replaced by a high-resolution cylinder through which only fractures found to intersect the bore/deposition holes are kept.*

Hydraulic properties of bentonite

The bentonite in the reified model should include both hydraulic and mechanical processes. Simulating mechanical processes allows for a detailed and realistic handling of the behavior of the bentonite near the rock wall, where some swelling room was available. It also includes a build-up of swelling-pressure in the bentonite. A detailed description of hydro-mechanical constitutive laws and properties is, however, beyond the scope of this report. The following remarks can be made for the hydraulic properties (see e.g. Åkesson et al. 2010):

- The *porosity* describes the total amount of water which the material can hold, and can be directly evaluated from the dry density.
- The water-holding capacity is described by a *water-retention curve* which is a relation between the water content and the RH or suction at equilibrium. An experimentally simple method used for the determination of retention curves is the method with jars, in which a free swelling specimen is placed in a jar above a salt solution (generating a specific RH). Such curves display a strong path dependence (hysteresis) which ideally should be taken into account (see, for example, Dueck 2004). In addition, at confined conditions the suction value is basically reduced by the value of the pressure. At full saturation, when the bentonite is in equilibrium with free water, this means than the swelling pressure equals the suction value at free-swelling conditions for the water content in question.
- The *intrinsic permeability* can be evaluated from measured hydraulic conductivity values. Such data generally exhibits a strong dependence on the dry density which can be expressed using, for example, an exponential function. Since hydraulic conductivity data usually exhibit a scatter, is can be useful to investigate the validity of such function for the bentonite in question using independent water-uptake tests of the material used in the experiment in question (e.g. BRIE field test).
- Finally, Darcy's law can be generalized to unsaturated conditions by introducing a *relative permeability*, which is usually defined as a function of the degree of saturation. This function has to be indirectly evaluated, using for instance the results of water-uptake tests, after the adoption of a permeability and retention curve.

Hydraulic properties of the rock

In order to construct an ideal model of the BRIE field experiment a very detailed characterization of the water transport into the borehole is needed. A problem here is that it is not, to our knowledge, possible to map the fracture network in the rock without disturbing it via, for example, drilling to obtain and characterize borehole cores. However, by conducting careful inflow measurements and fracture mapping on the borehole wall it should be possible to identify all the fractures which intersect the borehole down to a lower cut-off in transmissivity.

Hence, it seems to us that there are at least two ways to conceptualise the rock:

1) Implement a "global" fracture network based on a statistical description of the fracture network in the region and identify those realisations that best agree with the observed system near the borehole.
2) Implement a "local" fracture network determined from the fractures identified on borehole wall, and use the statistical description of the fracture network to determine the distance to which all these water-bearing-borehole-intersecting fractures are connected to another fracture with higher transmissivity.

It would seem to us that using approach 1) means that the reified model requires a very large (or even infinite) number of realisations to represent the true system as accurately as possible, even though in practise it is of course such that only a limited number of models is used.

Using approach 2) it is only necessary to construct a limited amount of models of the system to be sure that the effect of the uncertainty in the size of the zone-of-influence is taken into account. In practise this can be done by checking the most likely size, as well as lower and upper bound. Hence, in our view the latter approach seems as a more convenient way of representing the true system as accurately as possible and thus we have chosen to use that.

By modelling the fractures out to a distance where they have free access to water, we by definition model them out to the maximum distance where the pressure may be affected by the conditions in the borehole (atmospheric/high suction) – this volume is called the "zone of influence". The fractures are then implemented as thin discs cutting through this zone-of-influence (see Figure 2-1), connecting them to a homogeneous rock mass outside this zone. The fractures with transmissivity lower than the cut-off limit in the characterization is included via a "matrix hydraulic conductivity" applied to the rock material between the fractures within the zone of influence.

The *porosity* of rock samples can be determined through a drying step followed by water saturation. *Water-retention curves* can be quantified using a method with containers and salt solutions, similar to the one used for bentonite.

The hydraulic properties of rock are not as easily studied as those of bentonite, and may change when the rock sample is removed from its original place and tested in a laboratory.

For example, measurements of the hydraulic conductivity of borehole cores shows a dependence on the level of confining stress, with high compression stresses (about 15 MPa) leading to a significant reduction in conductivity (up to several orders of magnitude, see e.g. Vilks 2007a, b).

At least in our view, the water transport of the rock takes place in fractures which comes in a large variety of scales: from the micro-meter level up to kilometer size. The small-scale fractures are probably rather homogeneously distributed, while larger fractures have a very heterogeneous distribution. To accurately predict the water-saturation process in bore/deposition holes, the water-transport properties, as well as distribution, of all types of fractures must be characterized for the site in question.

Similarly to bentonite, also the rock's hydraulic properties depends on the water content/saturation. However, the exact behavior, at least in case of Äspö granite, does not appear to be as well understood as that of bentonite. This is particularly true for rock volumes which are not visibly intersected by fractures, but through which a matrix flow can still be measured. Both the retention and permeability of this rock matrix appears to be rather sparsely studied. One important question is, for example, if the permeability exhibits a strong dependence on the degree of saturation in the rock, as is suggested in vapor permeability measurements on other types of granite (see e.g. Hedenblad 1996 and discussion in Section 3.4).

In summary, the water transport properties of rock are, to our understanding, still a bit uncertain. This is something that will often be reflected in the rest of this document.

2.1.2 Actual model

While a detailed description of the actual models used to analyze the different subtasks of Task 8 are given in Appendix B – Appendix E, an overview is given here. The description of the Actual model also incorporate properties from independent experiments, but in this case they are formulated in order to *facilitate an implementation in the numerical tool* at hand, see Table 2-3.

The models presented here were primarily simulated using Code_Bright (the models presented in Section 3.4 were simulated using Comsol Multiphysics), which is as a finite-element solver developed to study THM processes in unsaturated media, with a high degree of specialization towards bentonite. It was not developed to model groundwater flow in rock and cannot, for example, be used to simulate a complicated fracture network. However, individual fractures can of course be modelled as a porous medium with a small aperture (≈0.05 m) and specified permeability values.

At the start our modelling we had two primary goals:

1) To participate in Task 8 (as part of EBS TF) in order to improve our modeling capabilities of the natural wetting of bentonite in repository-like conditions.
2) To aid in the decision making of the field experiment, i.e. to give guidance on when to, for example, terminate the experiment and excavate.

As such it seemed prudent to carry out the models using the large-scale 3D geometry (which includes TASO/D and a large volume of surrounding rock) defined in the task description. This was also the one which we initially employed. By analyzing the results from the models using the large-scale geometry we were, however, able to use a much smaller local-scale 3D geometry in some of the later models, which only contained the borehole with bentonite and the near-field rock. Using these local-scale geometries we were able to focus on solving particular issues regarding the water content distribution in the bentonite as measured after the field experiment had been dismantled, which could not be analyzed using the large-scale geometry due to the numerical complexity.

Both geometries were simulated by only considering hydraulic processes. The rock was treated as a homogeneous medium outside a cylinder with radius of 0.3 m, and which extended 0.3 m below the bottom of the two boreholes. Inside the *high-resolution cylinder* the rock was treated as a low-conductivity material intersected by one or more fractures. Hence, we assume that the *zone of influence* of the bentonite only extends about 15 cm outside the borehole.

In the first set of models done in Task 8D only the fractures identified in borehole 17 during the pre-characterization was included, borehole 18 was assumed to be free of intersecting fractures. In both models a matrix flow was included, the value depending on the model in question. In models constructed after the field experiment had been started, additional fractures were included, as motivated by both the measured relative-humidity evolution and the measured final state.

The porosity of the bentonite was assumed constant (mechanical processes were not modelled) and the outer gap was not included. The effect of the water filling of the outer gap was, however, investigated in one model, described in Section 3.2.3. A simplified treatment was also used in the bottom of the deposition hole, where the bottom sand filling was not included, and the bottom plate was given the same radius as the borehole. Also the effect of this simplification was investigated in one model, presented in Section 3.3.

The retention properties of both rock and bentonite was implemented using a standard van Genuchten retention curve, and the hysteresis behavior of the bentonite was not accounted for. The permeability was assumed to be dependent on the degree of saturation, with a power-law dependence in the bentonite. In the rock a van Genuchten relation was used.

2.2 Geometry

2.2.1 Large-scale model

The geometry consists of a cubic rock volume (side length of 30 m) which encompass parts of the TASD tunnel as well as the entire TASO tunnel. Three main deformation zones were identified in the task description as intersecting this volume of rock, however, only the two that also intersects the tunnels were included in our model. Aside from the inclusion of the two deformation zones the rock was modelled as a homogeneous material everywhere except near the two BRIE boreholes, as is illustrated in Figure 2-2.

Near the boreholes the rock is divided into "Deposition-hole rock", with a low hydraulic conductivity, and fractures. The fractures included are those identified in the pre-installation site-characterization. Some updates were made to the initial fracture calibration, both with respect to the number of fractures as well as to their shape (see Figure 2-2), and also to their hydraulic properties. These changes were motivated by the measured RH evolution during the field experiment.

2.2.2 Local-scale model

Models using the large-scale geometry in general had rather long simulation times (from several days up to a week), modifications to the geometry were tedious and they could only incorporate rather simple fracture geometries due to meshing issues. As such, a local-scale model was developed, with the goal of creating a more flexible geometry with much shorter simulation times, without the loss of any significant accuracy in terms of reproducing the evolution in the field experiment. Only borehole 18 was simulated using the local-scale models, as the modelled evolution in borehole 17 in the large-scale model was considered to be close enough to the actual evolution that no further analysis was warranted.

In Figure 2-3 the geometry constructed for the local-scale model of borehole 18 is shown. It consists of the borehole with buffer, the surrounding deposition-hole rock out to a radius of 0.3 m, and around this a cylindrical volume of fractured rock out to a radius of 0.6 m. The DHR material is intersected by two fractures in this particular version of the geometry, which was developed in order to better match the measured water content in the buffer after dismantling.

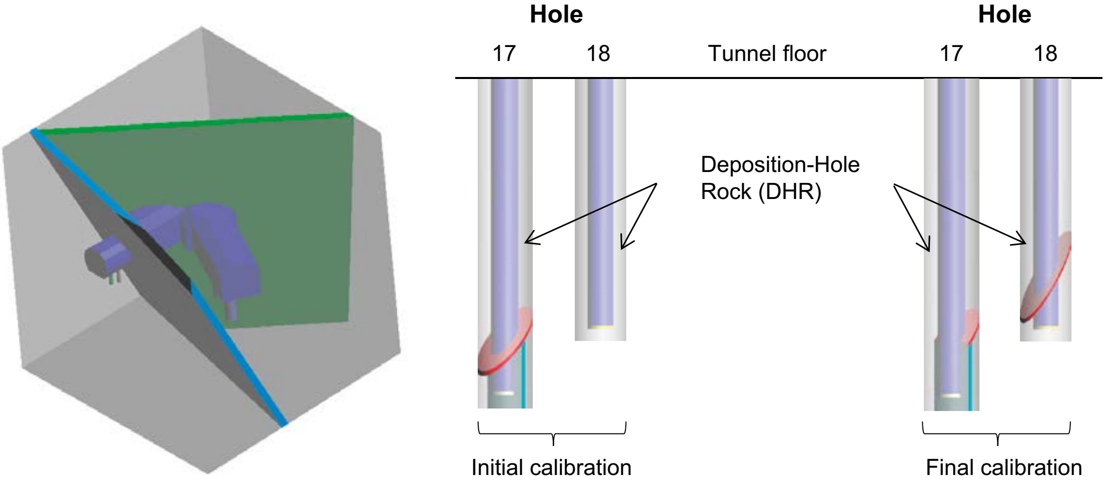

Figure 2-2. *Geometry used in the large-scale models. The left panel shows the entire 3D geometry, while the right panel illustrates the geometry around the boreholes. The two different calibrations illustrates how the model geometry changed during the course of the modelling due to input from the field experiment.*

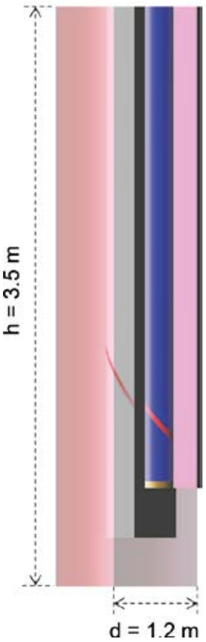

Figure 2-3. *Local-scale model geometry.*

2.3 Material properties and boundary conditions

An overview of the parametrization of the bentonites' hydraulic behavior is given in Table 2-4. With few exceptions, this parameterization was used in all models of the field experiment. During the modeling of the water-uptake experiment, however, some parameters were varied.

As for the hydraulic parametrization of the rock an overview is also given in Table 2-4. Here, however, some uncertainty is present, especially considering the intrinsic permeability, k_0, of the DHR material. Several different values of the intrinsic permeability were evaluated during the course of the modelling, as well as different relative permeability relations.

The boundary conditions used in the large-scale geometry was a prescribed liquid pressure of 3.3 MPa on the outer surfaces of the rock volume, except for at the side which intersects TASD, where a no-flow condition was prescribed instead. On the inner-open surfaces, that is the tunnel and open bore/deposition holes, atmospheric pressure conditions were prescribed.

In the local model the liquid pressure was prescribe at the top and bottom surfaces of the high-conductivity rock material. On top atmospheric boundary conditions were prescribed, while at the bottom the liquid pressure was taken from that measured in the large-scale model simulations (about 0.12 MPa).

Table 2-4. Parameter values used to describe the hydralic properties of the buffer and rock.

		Buffer	**DHR**	**Rock**
Permeability	k_0 [m^2]	6.4×10^{-21}	$5 \times 10^{-20} - 10^{-21}$	10^{-17}
	k_{rl} [-]	S^3	van Genuchten	
Retention			$S_l = \left[1 + \left(\Psi/P_0\right)^{\frac{1}{1-\lambda}}\right]^{-\lambda}$	
	P_0 [MPa]	9.23	1.74	
	λ [-]	0.3	0.6	
Initial conditions	Porosity	0.438	0.001	0.001
	Liquid pressure	−99.9	0.1	2.0

3 Results

Only the most important modelling results are presented and discussed here. For a more comprehensive discussion of all the model results see Appendix B – Appendix G. We begin by briefly discussing the results of the modelling of the water-uptake test in Section 3.1. Thereafter, in Section 3.2, we present the results of the large-scale models constructed to simulate the field experiment and discuss how these were updated as data from the experiment became available. In Section 3.3 we discuss the results of the local-scale models, which were constructed after the dismantling operation and were used to evaluate the effect of additional fractures and the effect of the bottom plate, and finally in Section 3.4 the effect of a different relative-permeability relation for the DHR material is analyzed.

3.1 Water-uptake test

Several models of the water-uptake test were constructed with the aim to determine 1) the effect of the outer gap, and 2) the validity of the hydraulic parameterization of the bentonite. As the water-uptake experiment was performed in laboratory conditions, with water flow only allowed over the vertical outer surfaces, the models, which were simulated using a 1D axisymmetric geometry (see Appendix B for details), can be expected to represent the evolution accurately. When modelling the outer gap it is needed to also simulate mechanical processes, as the gap will close very early on due to swelling of the bentonite.

Modelling the effect which the outer gap may have on the evolution of the buffer is important, as if it is small, the gap can be neglected in the 3D models of the field experiment, which 1) means that mechanical effects can be neglected, and 2) leads to a simpler geometry. Two models were done: one purely hydraulic model with a homogenized buffer density (i.e. no gap included) and one hydro-mechanical model with the gap. In Figure 3-1 the cumulative water inflow in both models is shown. As can be seen the difference between the two models is exceedingly small, which strongly suggests that the outer gap does not need to be included if one only wants to capture the wetting of the buffer.

As the water-uptake test is a very well defined experiment, it also provides an excellent opportunity to evaluate the hydraulic parameterization of the buffer used in our models.

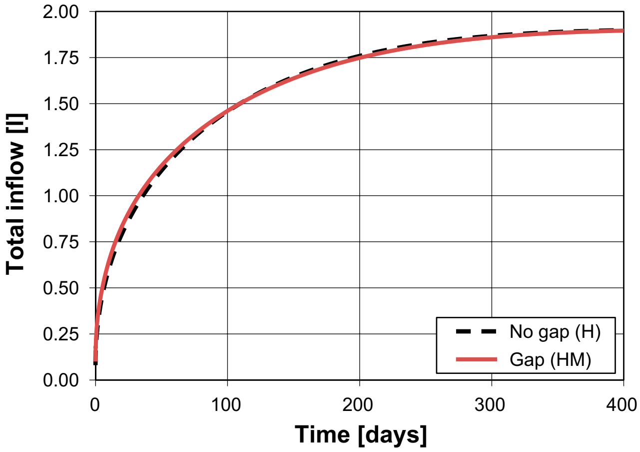

Figure 3-1. *The cumulative water inflow in the models of the water-uptake experiment. In the no-gap model only hydraulic processes were simulated, with the buffer in the final (radially homogenized) state, while in the gap model, both hydraulic and mechanical processes were simulated, with the buffer starting in the real initial state (see Appendix B for details).*

The water uptake tests resulted in three major sets of experimental data: i) evolutions of the cumulative water uptake; ii) evolutions of the relative humidity and stresses; and iii) profiles of degree of saturation and void ratio (Figure 3-2). A hydraulic evaluation of these tests were initially performed through: i) the optimization of two saturation dependent moisture diffusivity functions, which either were based on the water-uptake data (i.e. inflows) or on the water-saturation data (measured after dismantling); ii) the adoption of two in-situ retention curves (van Genuchten and square law type), which were based on initial and final data from RH sensors and measured degrees of saturation; and iii) the evaluation of saturation dependent permeability functions from the diffusivity functions and retention curves (see Fransson et al. 2016).

The tests were subsequently modelled with Code_Bright as a purely hydraulic problem with a 1D axisymmetric geometry (see Appendix B). The block was described as homogenized with a single constant porosity. The initial water filling of the outer slot was taken into account by applying water saturated conditions from the start in the outer 5 mm of the bentonite. The liquid pressure at the outer boundary was kept constant at an atmospheric level throughout the calculations (203 days). Four different model cases (with two retention curves and two relative permeability relations) were analysed.

The main experimental and model results regarding cumulative water-uptake, saturation profiles and RH evolution at sensor positions are illustrated in Figure 3-2. These tests have independently resulted in a parameter set which generally is consistent with the current material model for MX-80 bentonite (Åkesson et al. 2010) and the data sets provided in the Task 8 definitions. Some minor inconsistency in the overall water balance for the tests implies that slightly different transport coefficients can be evaluated from different data sets. Still, the results show that the hydraulic model for the bentonite is sufficiently accurate for the BRIE field test.

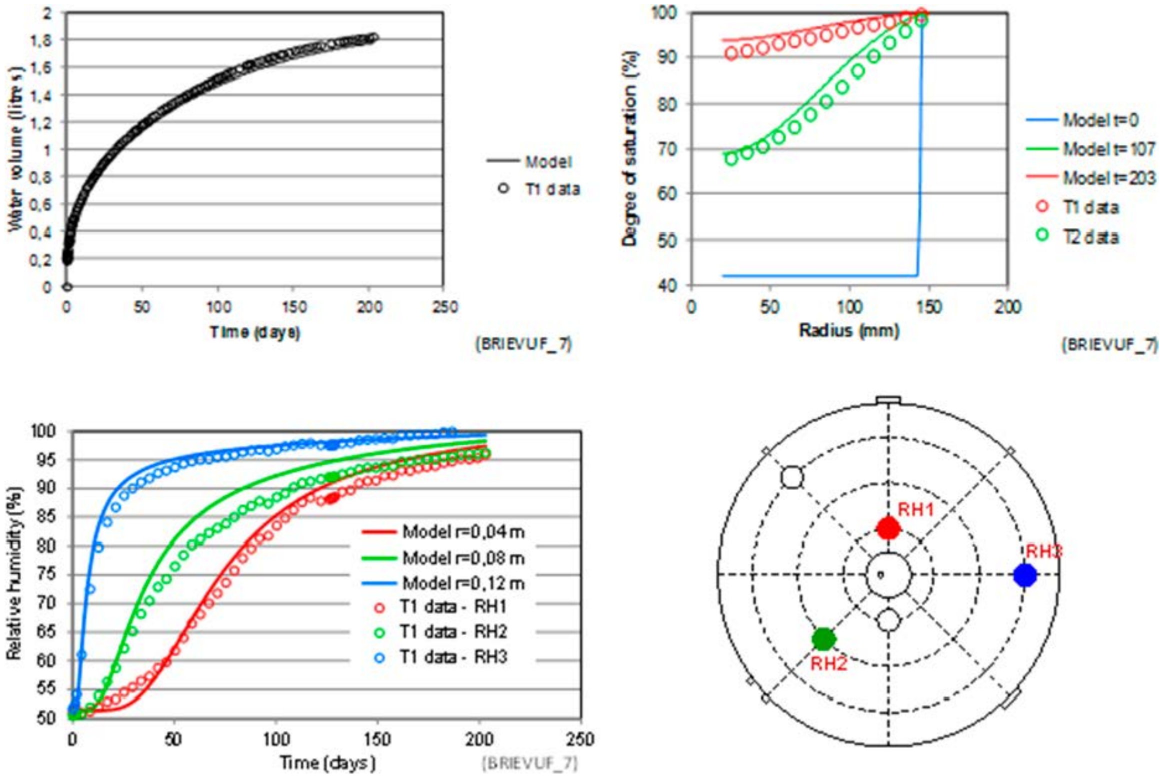

***Figure 3-2.** Experimental (symbols) and model results (lines) of cumulative water uptake (upper left), radial distribution of degree of saturation (upper right), and evolution of relative humidity (lower left). Sensor position indicated (lower right).*

3.2 Large-scale models of the field experiment

Several different models were simulated using the large-scale geometry of the BRIE field experiment. Here we discuss two sets of models: T8D_1a&b and T8D_2a&b (see Appendix J for more details). The first set of these models were simulated before the installation of the field experiment, and was thus a blind prediction of the outcome. However, as detailed characterization data from the site prior to installation was used it should probably be identified as a class B rather than a class A prediction (Lambe 1973). The second set of models were calibrated using data from the relative-humidity sensors in the field experiment, and hence was a class B1 prediction of the experiment.

3.2.1 Class B prediction models

Models T8D_1a&b only differed in the value of the hydraulic conductivity of the DHR material (see Section 2.2.1), in model T8D_1a a hydraulic conductivity equal to $K_{DHR} = 5 \times 10^{-13}$ m/s was chosen, while in T8D_1b a value of $K_{DHR} = 1 \times 10^{-13}$ m/s was set. It should be noted that the sensor positions were those assumed correct at the time, however, as is discussed later on in this section, this later proved to be somewhat incorrect. The prediction of the evolution in the boreholes 17 and 18 is here only analyzed in terms of its ability to predict the measured RH evolution.

In Figure 3-3 the RH evolution in in model T8D_1a ($K_{DHR} = 5 \times 10^{-13}$ m/s) is shown while Figure 3-4 depicts the RH evolution in model T8D_1b ($K_{DHR} = 1 \times 10^{-13}$ m/s). In both figures the evolution in borehole 17 is shown in the top panel and the evolution in borehole 18 is shown in the bottom. The models only simulated the evolution during the first 300 days and as such the graphs does not extend beyond this time. Solid lines identify experimental data, while dashed lines identify model data.

Borehole 17

The relative-humidity evolution in the buffer in borehole 17 with the higher value of the matrix conductivity (upper panel of Figure 3-3) shows a relatively good agreement at the depth of the main fracture ($d = 2.6$ m). However, in the dry instrumented part ($d = 2.3$ m) the model is considerably wetter than what is seen in the sensor data.

At a first glance, however, the agreement between modelled and experimental data appears to be rather good for the lower value of K_{DHR} (i.e. Figure 3-4 upper panel), even in the dry lower dry zone. However, this agreement does not hold to closer inspection. In the experiment the relative humidity in all sensors increased sharply during the first week from the starting point of 58 % and after a few weeks settled at a value of about 65 %. This increase (which was probably caused by the artificial wetting of the outer slot; see Section 3.2.3 for a discussion on this) is not included in the model. Instead the matrix inflow in model T8D_1a gives an increase in relative humidity which after 300 days is rather similar to the experimental values. However, in the experiment, the RH values are rather constant after the initial increase; no discernible matrix inflow is seen[1]. Hence, while the predicted RH values after 300 days agrees reasonable well with experimental values, the time evolution up until then is quite different in the experiment as compared to the model.

---

[1] The increase in RH seen after about 250 days is, as will be discussed later probably not matrix flow, but instead axial flow from the fracture situated at the 2.6 m level.

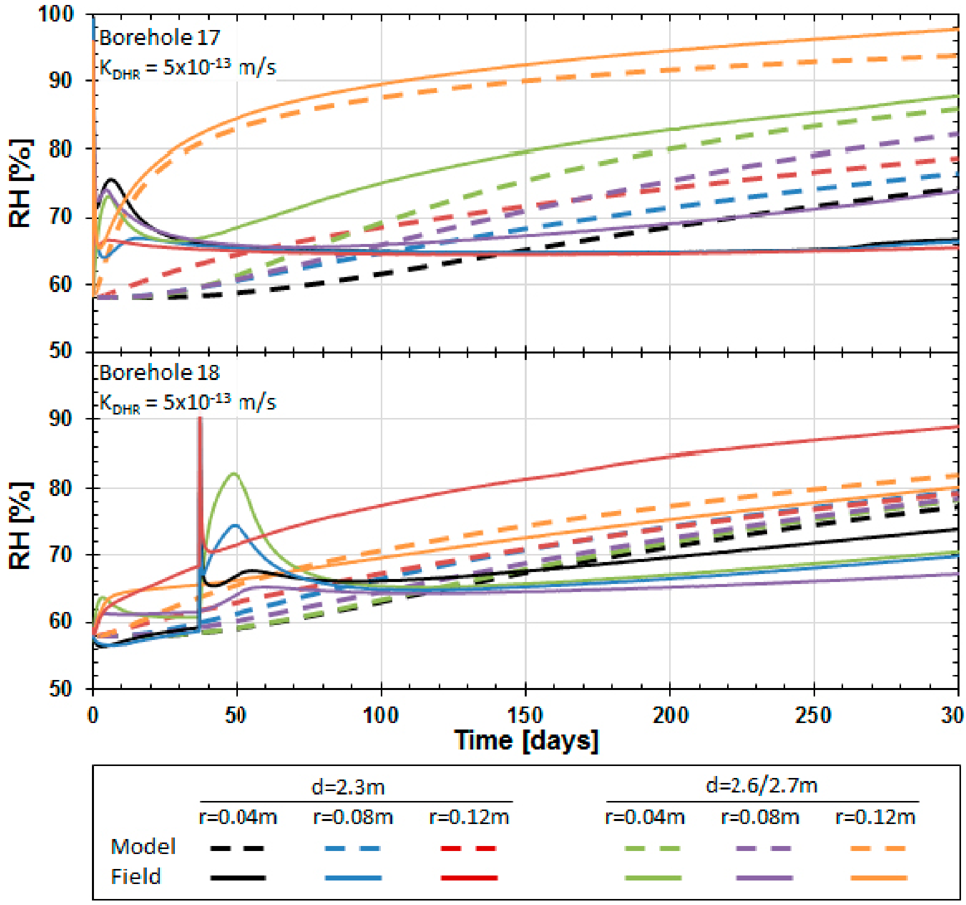

***Figure 3-3**. Model T8D_1a – RH evolution at the original sensor positions in borehole 17 (top) and borehole 18 (bottom). Solid lines identify experimental data, while dashed lines identify model data.*

Borehole 18

At a first glance one might think that model T8D_1a (i.e. with $K_{DHR} = 5 \times 10^{-13}$ m/s, shown in the lower panel of Figure 3-3) matches the evolution in borehole 18 rather well, however, at closer inspection this proves incorrect. In model T8D_1a the water inflow is only matrix flow (no fracture was included in the model), however the field data strongly suggests that the water inflow comes through a fracture (which was identified in the site characterization, but thought to provide very little water. In Figure 3-5 the position of the relative-humidity sensors with respect to the fracture identified in the site characterization (not included in the model) is shown. As is seen it can be expected that if the inflowing water mostly comes via the detected fracture, one would expect the two RH sensors situated at r = 0.12 m to show increased values first, followed by the sensors at r = 0.04 cm at d = 2.3 m, which should more or less simultaneously be followed by the sensor at r = 0.08 m on the same depth. Except for the last mentioned RH sensor this is exactly the evolution seen in the field. That the RH sensors at r = 0.08 m, d = 2.3 m shows a rather slow increase in RH is somewhat surprising; but this is probably due to heterogeneities in the fracture flow.

In general it can be said that, aside from the lack of a fracture, the evolution in the other sensors (i.e. those at r = 0.04 and 0.08 m at d = 2.7 m) is slightly to fast in model T8D_1a, in that the RH values in the model increase faster than the measured values. In model T8D_1b on the other hand (see Figure 3-4) the relative humidity increase in all sensors is slower than the experimental values.

The observation that the low-value matrix conductivity gives the best match to sensors data in borehole 17, while it is too dry in borehole 18, indicates that fracture wetting was significant also in borehole 18 and that the lack of any fractures in the model is the reason for the poor match with experimental data.

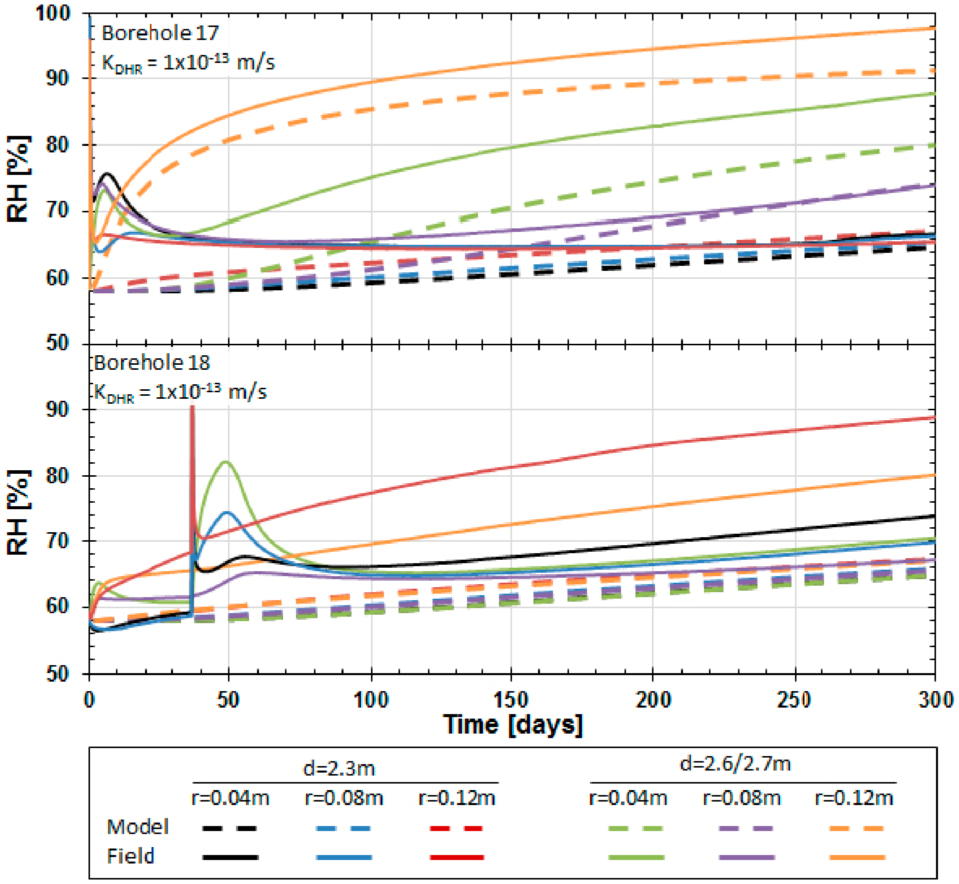

Figure 3-4. *Model T8D_1b – RH evolution at the original sensor positions in borehole 17 (top) and borehole 18 (bottom). Solid lines identify experimental data, while dashed lines identify model data.*

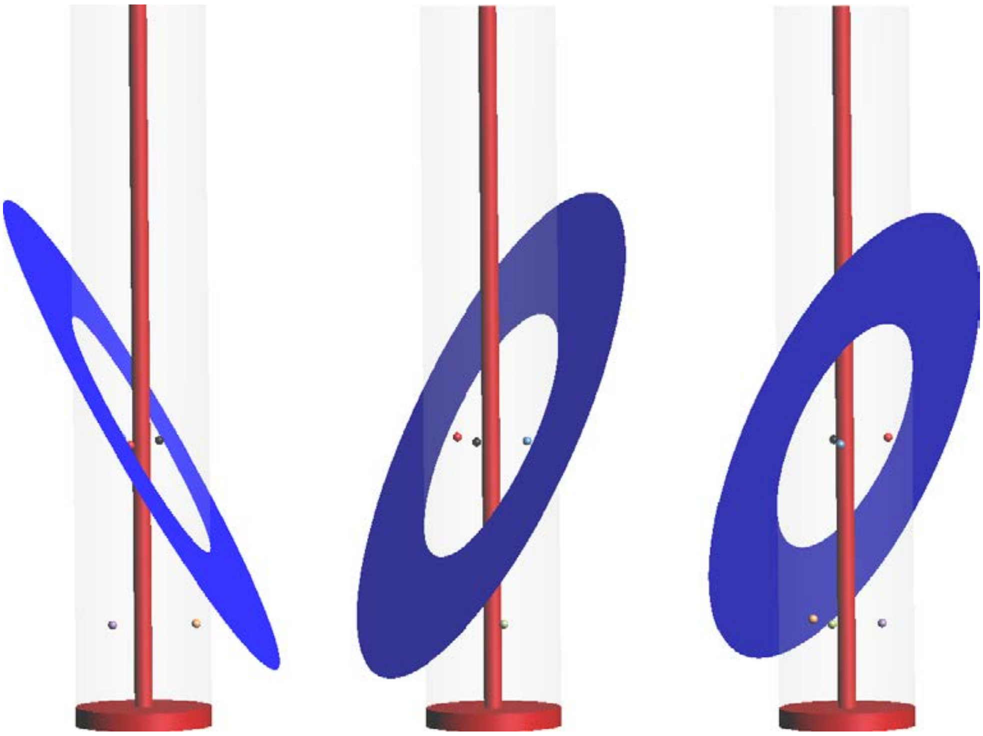

Figure 3-5. *Illustration of the position of the RH sensors with respect to the fracture found in the site characterization of borehole 18. The colors used to identify the different RH sensors corresponds to the colors used in Figure 4-3 and Figure 4-4.*

3.2.2 Class B1 prediction models

Several updated models were constructed after the Class B prediction models discussed above in Section 3.2.1. Two of these models will be discussed here; T8D_2a, which was constructed to improve the predicted evolution in borehole 17, and T8D_2b, which was constructed to improve the predicted evolution in borehole 18.

The model focusing on borehole 17, T8D_2a, was constructed and simulated in April 2013, i.e. before dismantling data became available to us. The model focusing on borehole 18, T8D_2b was constructed and simulated in February 2014; the model was in fact finalized about one week after borehole 18 was excavated. However, no dismantling data was available to us during the construction of the model. As such, by definition, both models constitute class B1 predictions, since we used data from the ongoing experiment when constructing them, but no dismantling data (Lambe 1973).

The most important changes with respect to the models discussed in Section 3.2.1 are:

- A reduction in the matrix hydraulic conductivity to $K_{DHR} = 10^{-14}$ m/s.
- Several additional fractures intersecting the boreholes were added.
- The properties of the existing fractures were updated. For example, a part of the fracture of main interest in borehole 17 was removed.

All these changes were motivated by the measured RH evolution (matrix conductivity due to the slow response in the dry section of borehole 17 and additional fractures/change in fracture properties due to the sensor response in the wet sections of both borehole 17 and 18).

Aside from these changes to the model itself, it was also realized rather early on that the position of the RH sensors relative to the main borehole-intersecting fractures, as given in the task description, were incorrect. This was caused by incorrectly measured orientations and depths of the borehole-intersecting fractures. As the wetting of the bentonite was dominated by fracture flow and thus was highly heterogeneous, calibrating the model using sensor data from incorrect relative positions is a hopeless task. Unfortunately, the correct orientations and depths of the fractures were not accurately determined until after the field experiment had been dismantled.

As the models discussed here were simulated before the dismantling data was available, and we did not have the opportunity to re-build the large-scale geometry, the problem was handled by a new post-processing of the model results so that the relative humidity was read out at the correct positions relative to the main fractures in both boreholes. In the following two section we first present and discuss the original post-processing and thereafter the final post-processing in borehole 17 and 18 respectively.

Borehole 17

In Figure 3-6 the relative-humidity evolution in borehole 17 from the original post-processing of model T8D_2a is shown. The evolution is shown for the entire duration of the field experiment. Solid lines identify sensors data from the field experiment while the dashed lines identify model data. As the relative-humidity time evolution is very different at the two instrumented depths we will discuss them separately.

The dry zone (d = 2.3 m)

The relative-humidity evolution in both the model and field experiment is very slow in this zone. In the experiment almost no increase in the relative humidity values is seen until 250 days after installation, except from the very early increase in relative humidity due to the artificial water filling of the outer slot. Aside from that the model does not reproduce the initial increase in relative humidity (since the initial slot between the rock and buffer is not included) it agrees rather well with the measured evolution. Hence, the apparent difference in relative humidity of about 7 percentage points between measured and modelled values is due to the simplifications in the model. However, after about 250 days the measured relative humidity shows a slow but significant increase; this feature is not seen in the model data.

The wet zone (d = 2.6 m)

The relative-humidity evolution in this region shows a significant increase in relative humidity in all sensors (solid lines). The fastest and largest increase in seen in the outermost sensor (r = 0.12 m), which is followed by the innermost (r = 0.04 m) sensor. The middle sensor (situated at r = 0.08 m) shows the slowest and smallest increase in relative humidity at this depth.

This somewhat counterintuitive behavior is due to the position of the sensors with respect to the fracture; since the fracture has a rather large dip and the sensor plane is situated at the top of the fracture the buffer block with sensors in it is effective "fed" water at only one point. Due to the orientation of the sensors this means that the distance between the sensors and the source of water is smallest for the sensor at r = 0.12 m, followed by the sensor at r = 0.04 m. The middle sensor (r = 0.08 m is actually situated furthest away from the source of water and hence it is not surprising that this shows the slowest and smallest increase in relative humidity.

As can be seen in Figure 3-6 the general trends in the measured RH evolution is rather well matched by the model event though the absolute values are a bit too low. At the time of modelling no further attempt was done to improve the match in relative humidity by, for example, calibrating the transmissivity of the fracture, as it was already known at this time that the position of the sensors were uncertain.

After the excavation of the bentonite in borehole 17; the fractures' positions and orientations could be determined; and it turned out that fracture depth should be shifted about 8 cm upwards. To account for this the model data was post processed again, but instead of moving the fracture, the sensor planes were shifted 8 cm downwards in the model. This means that the sensors in the wet (lower) section are somewhat too close to the bottom of the borehole, however, as we treat this as a closed boundary it has a rather small effect on the model results. Had the gap between bottom plate and rock wall been included, the model data would probably have shown to much wetting.

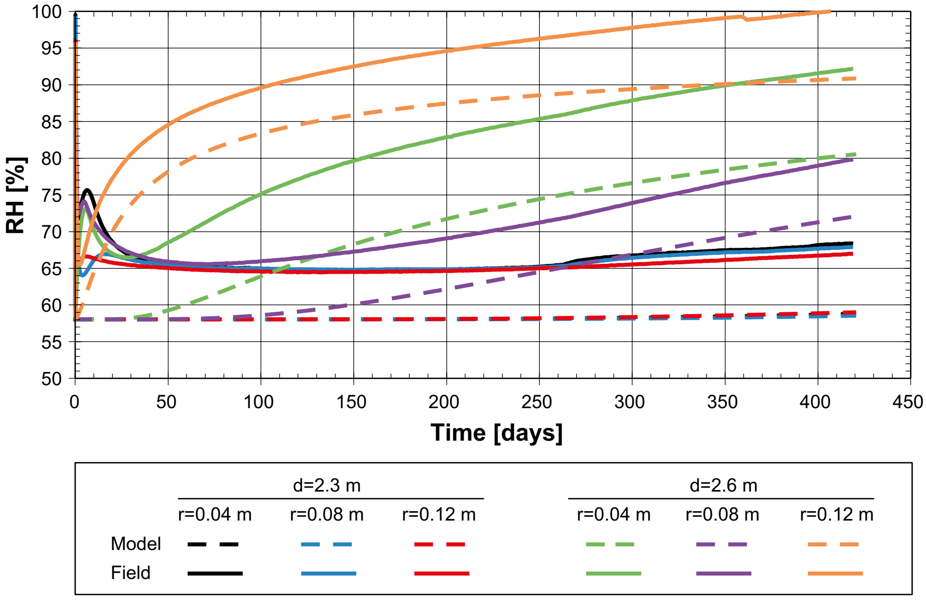

__Figure 3-6.__ The RH evolution in the field (solid lines) and model T8D_2a (dashed lines) in borehole 17. The model data is read off at the positions where the RH sensors were originally thought to be situated with respect to the main fracture.

In Figure 3-7 the model results (dashed lines) from the new post processing is shown; as can be the agreement between model and experimental data improved rather significantly compared to the original post processing. The most significant changes are:

- In the wet section the absolute relative-humidity values now agree rather well with the measured values.
- In the dry section an increase in relative humidity, which starts between 200 and 250 days after installation is now seen, which agrees rather well with the increase in experimentally measured values at this point in time. It should be mentioned that the increase in relative humidity in the model is due to axial water transport in the bentonite from the wet section situated further down, and hence emanates from the main fracture that intersects the borehole. That this is seen in the new post-processing is caused by the decreased axial distance to the top of the fracture.

In general it can be said that the model reproduce the measured relative-humidity values in borehole 17 rather well. However, a more important check of the model's ability to predict the evolution in the field is how well the final water content in the buffer from the model agrees with the measured values.

In Figure 3-8 the water content in the buffer emplaced in borehole 17 is shown in the final state of the buffer (i.e. at the time of excavation). Only the part of the buffer situated between the bottom plate and up to a height of 1.5 m is shown, as the water content in the buffer situated above 1.5 m was not analyzed. Both experimental results and model data are included; the red-dashed rectangles identify model results. The graphs showing model results are offset with respect to the experimental data. This is in order to make the main horizontal fracture level in the graphs.

As can be seen the agreement is rather good in the depicted region, in particular up to a height of approximately 1 m. The model is able to accurately reproduce the water content variations in most directions except for φ=216°, and close to the bottom. The latter discrepancy is probably caused by the omission of the small open column between the bottom plate and rock wall which was present in the field and which allowed water to enter the bentonite from below.

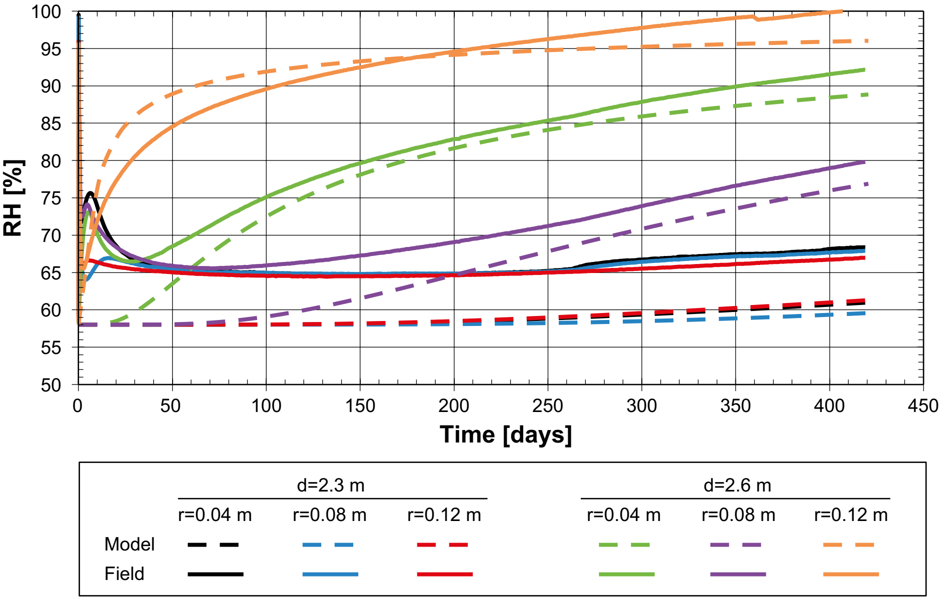

***Figure 3-7.** The RH evolution in the field (solid lines) and model T8D_2a (dashed lines) in borehole 17. The model data is read off at the positions where the RH sensors were actually placed with respect to the main fracture as determined during the excavation and dismantling of the BRIE field experiment.*

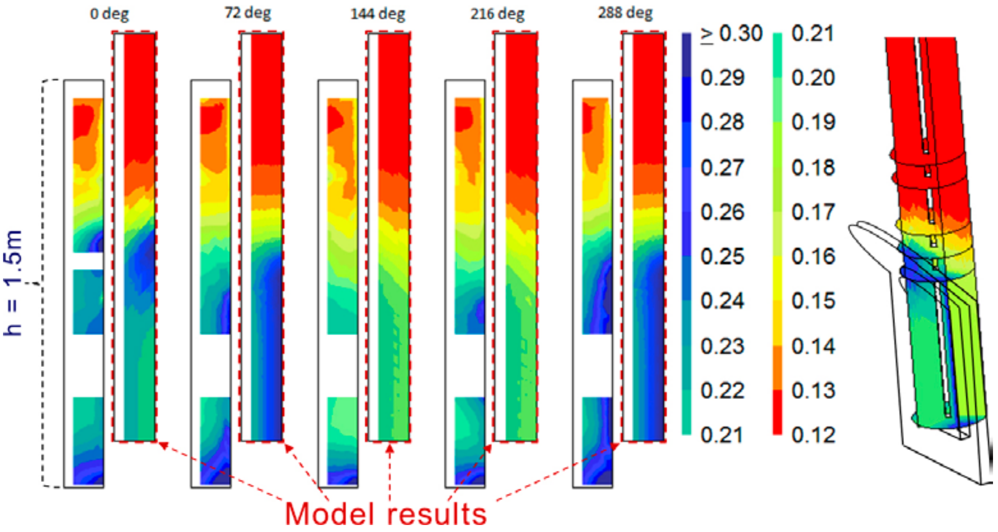

***Figure 3-8.** Contour plots of the water content in borehole 17 at the time of dismantling compared with experimental data. The red-dashed lines identify model results, the collage on the right-side of the figure is also model data.*

Above a height of 1 m the model is perhaps a bit dry, as essentially no water has entered the bentonite in the model, as compared to the experimentally measured values, which indicate some wetting. This discrepancy may in part be due to the thin outer column (which was not included in the model) which in the experiment was filled with water that in turn was absorbed by the buffer.

Borehole 18

The model T8D_2b, which was constructed to improve the model of borehole 18 contained a single intersecting fracture, which was based on the fracture detected in the pre-characterization of the borehole, but then thought to give very little water. The relative humidity evolution in the model is shown in Figure 3-9 (dashed lines) together with measured data (solid lines).

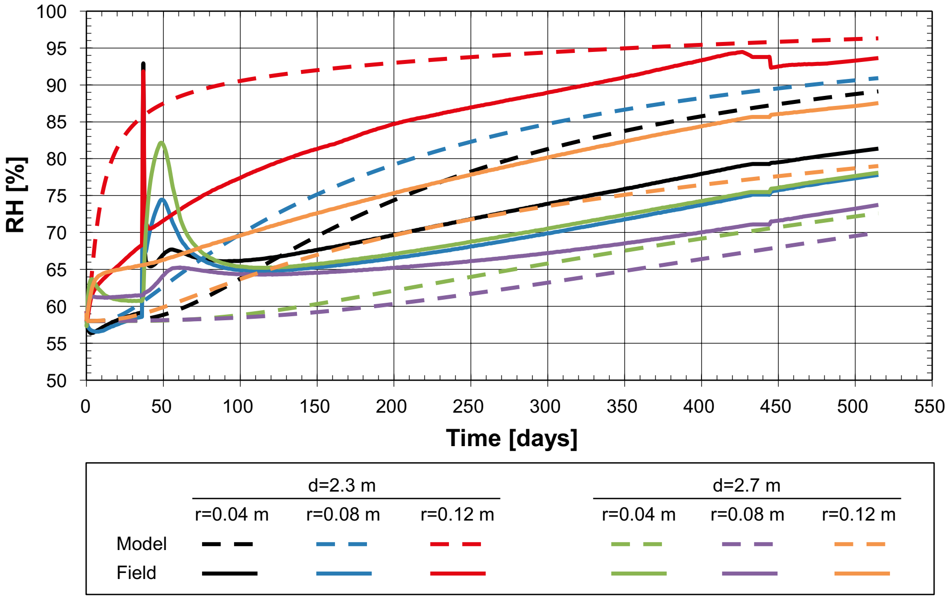

***Figure 3-9.** Model T8D_2b – Prediction (class B1) of the RH evolution in borehole 18. Dashed lines represent experimental data and solid lines model data. The data is from the original post-processing of the model, and hence the fracture position is incorrect.*

It should be pointed out that, similarly to borehole 17, the site characterization of borehole 18 did not determine the geometrical properties of the main fracture entirely correct. The data in Figure 3-9 is from the original post-processing. After the experiment had been excavated it was realized that both the fracture depth and dip angle was incorrect in the model. Due to limited resources it was decided to no construct a new large-scale geometry to correct for these errors. Instead the problem was handled in two ways: 1) a new post-processing was done of the model T8D_2b, and 2) a local-scale geometry was constructed (see Section 3.3). To correct for the errors in the fracture geometry in the new post processing we 1) rotated the sensors planes so that the orientation with respect to the fracture was corrected, and 2) shifted the depth of the lower sensor plane so that the distance to the lowest point of the fracture on the borehole wall was correct (as determined during the dismantling of the field experiment). It should be pointed out that, similarly to borehole 17, the site characterization of borehole 18 did not determine the geometrical properties of the main fracture entirely correct. The data in Figure 3-9 is from the original post-processing. The relative-humidity evolution in this new post-processing is shown in Figure 3-10.

The agreement is acceptable in three of the sensors. At the 2.3 m level the outermost sensor (red lines) shows good agreement between model and sensor data. The two sensors further in are, however, considerably wetter in the model as compared to what is seen in the sensors data.

At the 2.7 m level the two innermost sensors shows relatively good agreement with model data, if one takes into account the discrepancy of about 7 percentage points in relative humidity due to the uptake of water from the artificial water filling of the outer slot, which is not included in the model. The outermost sensor, however, shows a much stronger increase than what is seen in the model data.

In Figure 3-11 the water content at the time of dismantling from the calibrated model is shown and compared with the measured values. As can be seen the model is considerably drier in both the bottom and in the upper parts of the shown contour plots as compared to the experimental data. However, in the middle parts (e.g. approximately between a height of 0.3 and 1.2 m above the bottom plate) the model reproduces the measured water content relatively well. The discrepancy in the bottom is most likely caused by our simplified treatment of the geometry in this region, where the bottom plate is assumed to have the same radius as the borehole. This is further analyzed in Section 3.3.

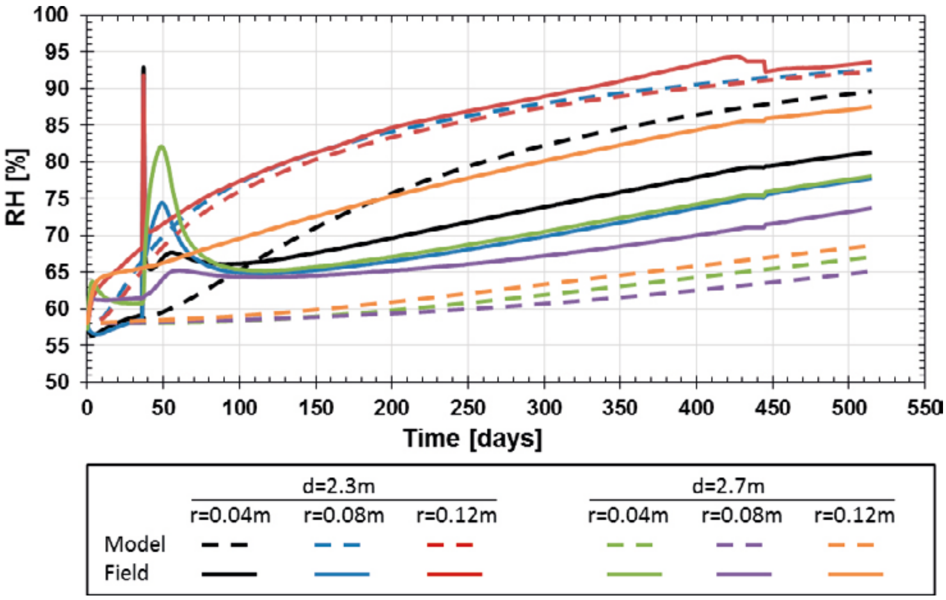

Figure 3-10. Model T8D_2b – Prediction (class B1) of the RH evolution in borehole 18. Dashed lines represent experimental data and solid lines model data.

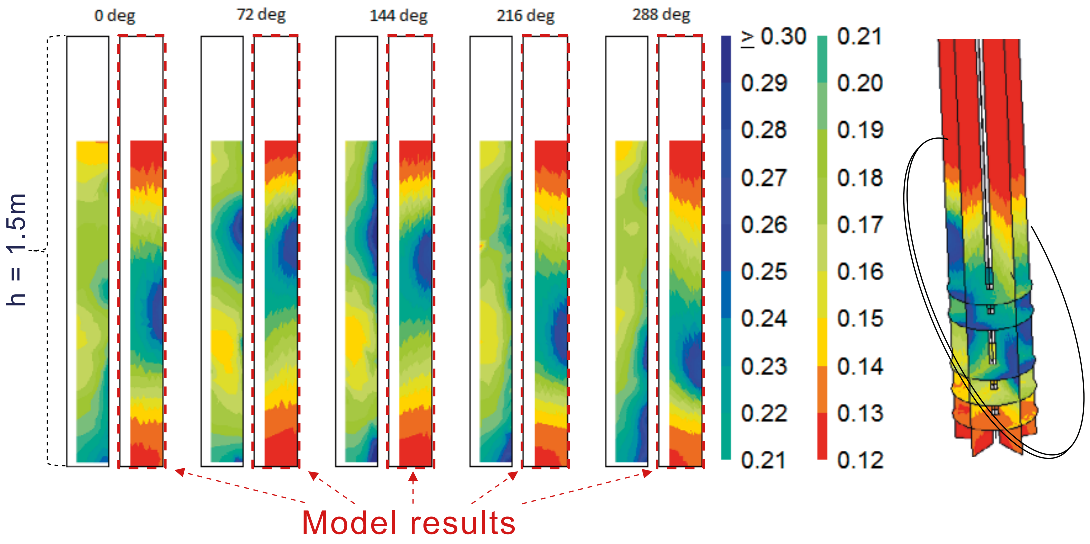

Figure 3-11. *Contour plots of the water content in borehole 18 at the time of dismantling compared with experimental data. The red-dashed lines identify model results, the collage on the right-side of the figure is also model data.*

3.2.3 Post-dismantling modelling using the large-scale geometry

Most of the post-dismantling modelling centered on analyzing borehole 18 using a local-scale model (see Section 3.3 below). However, one model focusing on the evolution in borehole 17 was also done, for which the large-scale geometry was used. The purpose of this model was to investigate the early increase in the measured relative humidity in all sensors.

Early experimental RH evolution in borehole 17

In Figure 3-12 the measured RH evolution during the first 50 days in borehole 17 is shown. Two remarks can be made:

1) There is an initial spike in relative humidity; this was caused by flooding of the central tube during the artificial water filling of the air slot in between the bentonite and rock. The water was then most likely transported to the sensors via the cables, which emanated from the central tube. Hence, this spike in RH was most likely a local effect around the sensors.
2) After the initial spike the RH goes down again, due to moisture redistribution. However, once the RH has reached a value of about 65 % it remains at this new base level. Hence, it would appear that a new equilibrium has been reached at a slightly higher relative humidity.

It would be easy to draw the conclusion that the increase in base-level relative humidity is caused by the wetting which caused the initial spike, however, this is probably not the case. Instead, the explanation can be found by analyzing the third water-uptake test. In it a single bentonite block (10 cm high), with similar geometrical properties to those of the blocks installed into the BRIE boreholes, was placed inside a steel cylinder. Around the block a 1 mm thick empty slot was present, just as the slot between the rock and bentonite in the field experiment. The slot was then artificially filled with water; effectively simulating the water-filling of the open slot in the field experiment, where after no more water was added.

The relative humidity was measured at the same radii as in the field experiment; the evolution can be seen in Figure 3-13. As is seen a rapid increase in relative humidity was observed in all sensors; after about 50 days the relative humidity in all sensors had increase by about 9-11 percentage points, where after they remained stable. The two outermost sensors reached steady state at essentially identical relative humidity values, while the innermost sensor registered a slight lower steady-state value.

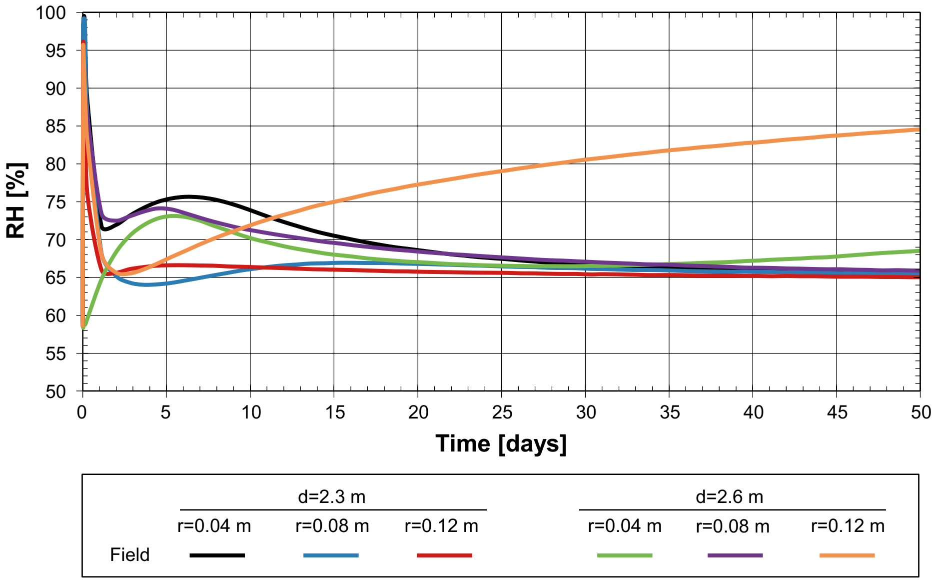

Figure 3-12. *Measured relative-humidity evolution during the first 50 days in borehole 17. All sensors initially started out at RH = 58 %, however after the initial spike the RH settles at a value of about 65 % in all sensors (except the outer sensor at 2.6 m which shows a significant increase in RH due to fracture wetting).*

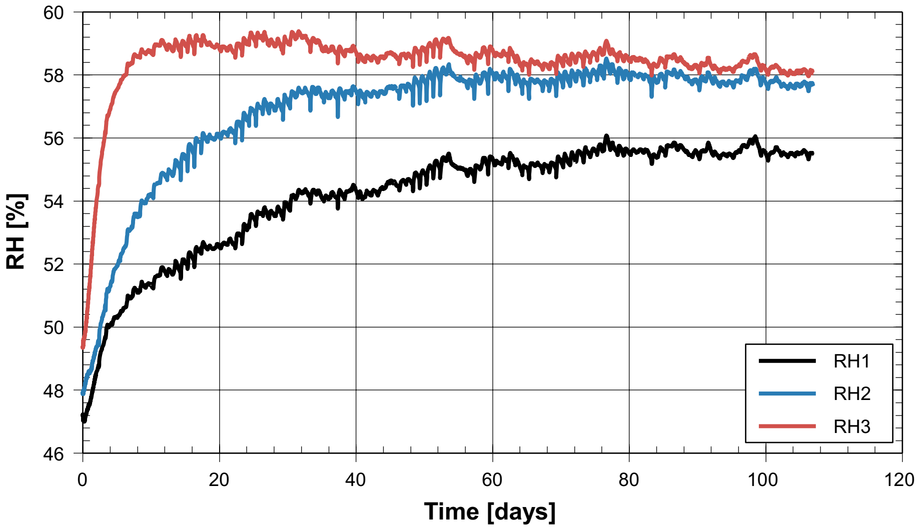

Figure 3-13. *The measured relative-humidity evolution in the third water-uptake experiment. Sensor RH1 was situated at r = 0.04 m, RH2 at r = 0.08 m and RH3 at r = 0.12 m.The experiment was terminated and dismantled after 107 days.*

After the experiment had been dismantled the water content was measured in five different directions. In Figure 3-14 the average value at each radii is plotted, together with the sample standard deviation. The measurements shows that although the relative humidity had increased, the water content had remained roughly unchanged at the radii where the relative humidity was measured ($r \leq 12$ cm). However, outside a radius of 12 cm a clear gradient in water content was seen, with the value increasing from about 12 % to 14.5 %.

The conclusion that can be drawn, given that the relative humidity measurements indicated that steady state had been reached well before dismantling, is that the bentonite was in moisture (suction) equilibrium, even though a water content gradient was present.

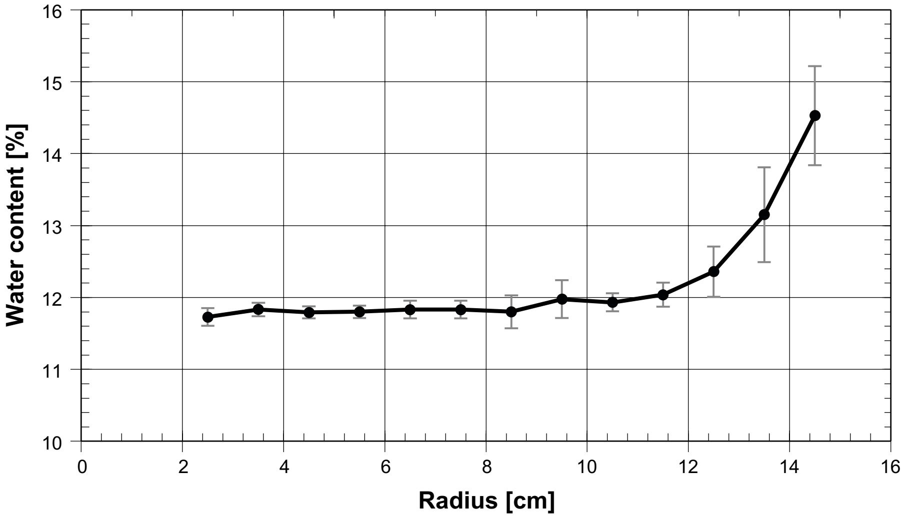

Figure 3-14. *The final measured water content in the third water-uptake experiment. The water content was measured in five different directions; for each directions the water content was measured at 13 different radii. The error bars represent the spread in measured water content in the different directions (calculated as the sample standard deviation). It can be pointed out that both measurement error and heterogeneous wetting (if, for example, the block was not exactly centred in the steel cylinder) contributes to the somewhat large standard-deviation values at the three outermost measurement points.*

To understand the cause of this one must take into account the hysteresis behaviour of the bentonites retention properties. This manifests itself in that the retention behaviour of bentonite is different depending on whether it is undergoing drying or wetting. This can be seen in measurements of the retention properties of bentonite.

This manifests itself in that the path in relative-humidity – water-content space is rather different depending on whether the bentonite sample is undergoing wetting or drying.

The results of the third water uptake experiment can be interpreted as if the outer parts underwent a quick and significant increase in relative humidity and water content as the water in the outer slot was taken up. This water was then transported further in, decreasing the relative humidity in the outer parts, while increasing it further in, until vapor pressure (or RH) equilibrium was reached. The drying in the outer parts led to a decrease in water content, but not all the way down to the original value. In contrast, the hydration of the inner parts appears to have been very limited even though the RH had increased from 47 to 56 %. This path dependence (hysteresis) therefore appears to have created a persisting water-content gradient. It seems reasonable to assume that a similar behavior took place in the field experiment, after the water-filling of the outer slot; i.e. that the uptake of the water in the outer slot led to an increase in relative humidity in the entire bentonite column, without any significant changes in water content, except in the outermost parts. A lesson that can be drawn from this is that it may be important to take hysteretic effects into account in the adoption of water-retention curve, especially for problems with a limited water supply.

It seems reasonable to assume that a similar behavior took place in the field experiment, after the water-filling of the outer slot; i.e. that the uptake of the water in the outer slot led to an increase in relative humidity in the entire bentonite column, without any significant changes in water content, except in the outermost parts. For an illustration of this see Figure 3-15.

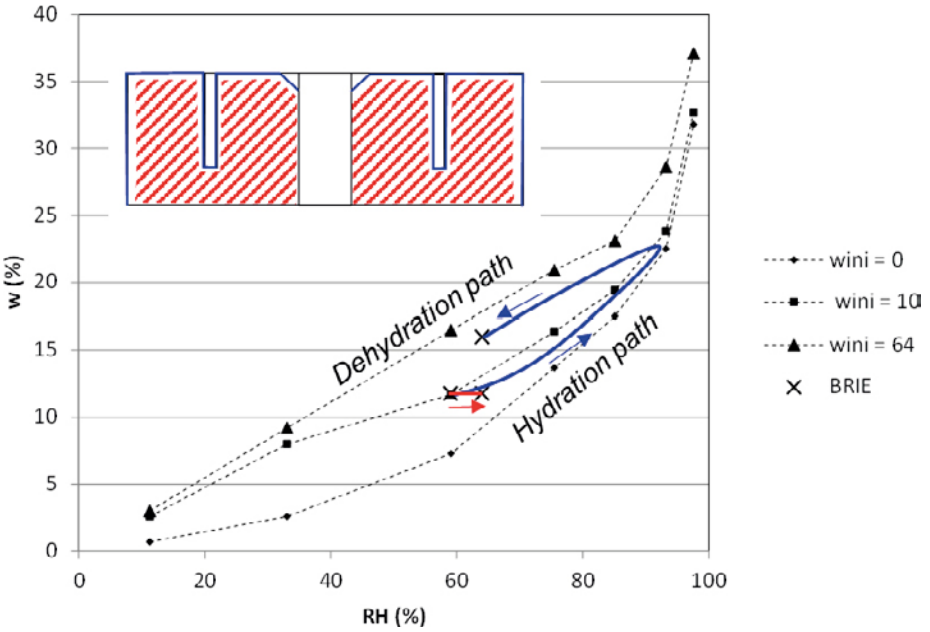

***Figure 3-15.** Schematic interpretation of equilibration subsequent to the filling of the outer slot and the flooding events. The filling of the outer slot implied that the peripheral parts of the blocks underwent a hydration/dehydration path (blue line) with a net increase in water content. In contrast, the inner parts could stay in equilibrium with slowly increasing RH levels without any significant water-content increase (red line). Laboratory data for different initial water content (0, 10 and 64 %) marked with dotted lines (from Dueck and Nilsson 2010).*

Low initial suction model

In order to investigate how the uptake of water from the slot, which is not directly included in our models, one model was simulated in which the initial suction of the bentonite was changed. As it was difficult to estimate exactly what value of initial suction to choose, a value corresponding to a relative humidity of 65 % was chosen, as this was the average value seen in the sensors in the dry part of borehole 17 after 100 days (at which point no further decrease in relative humidity was seen). A relative humidity of 65 % corresponds to a suction of 57.7 MPa (given the liquid-pressure dependence of the liquid density employed in our models), which in turn would lead to a change in initial degree of saturation if the original retention curve was used. Hence, this was slightly modified, in order to keep to the initial degree of saturation. The same form was used (standard van Genuchten) but the two shape parameters was changed to (original values in parenthesis) $P_0 = 9.43$ MPa (9.23 MPa) and $\lambda = 0.32$ (0.30).

The relative-humidity time evolution in borehole 17 from this simulation is shown in Figure 3-16. As can be seen the agreement between model and sensors data is excellent, with only the outermost sensor at the 2.6 m depth level showing any significant deviation from the experimental data. It should of course be emphasized that the results does not show that the change in relative humidity which occurs early on is caused by the uptake of slot water, only that this is a plausible explanation. The extensive tweaking of model parameters that had to be done to achieve the results in Figure 3-16 also shows that modelling even a rather simplified and well controlled case of natural wetting of bentonite is a very complex task.

In Figure 3-17 the water content from the model with low initial suction is shown together with the experimental data. These results can be compared with the original model, seen in Figure 3-8, as is seen the differences are relatively small.

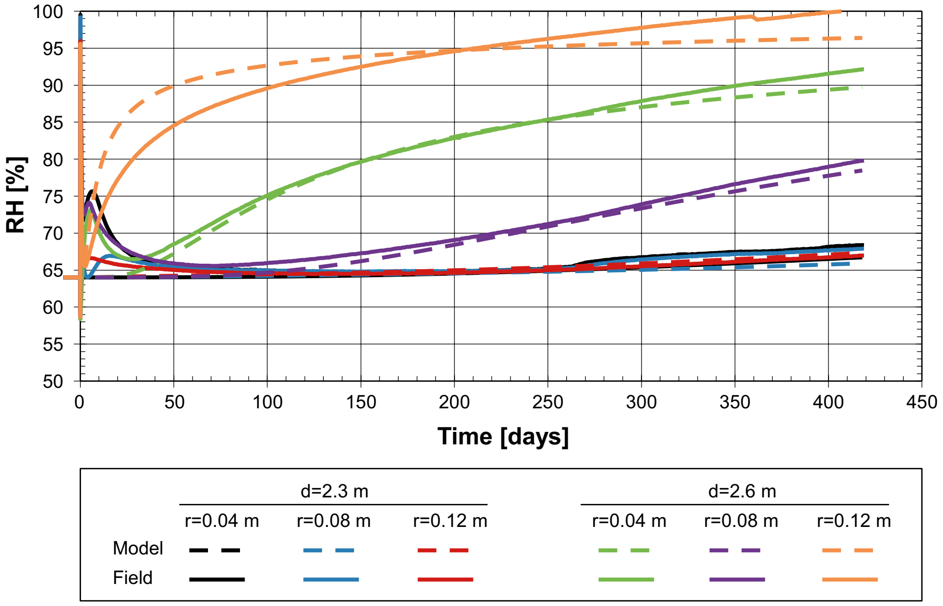

***Figure 3-16.** Relative-humidity evolution in the model of borehole 17 with an alternate retention curve and higher initial relative humidity. Solid lines represent experimental data and dashed lines model data.*

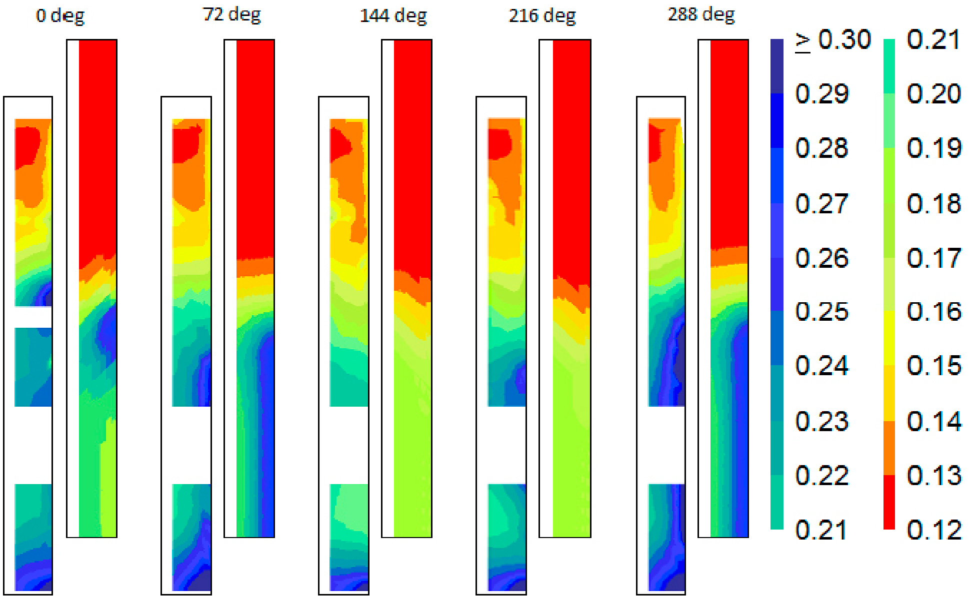

***Figure 3-17.** Contour plots of the water content in borehole 17 at the time of dismantling. Each pair of contour plots shows the data at the given direction, with experimental data on the left side and model data on the right side. The model results are taken from the simulation with an alternative retention curve, with a slightly higher initial relative humidity in the bentonite.*

3.3 Local-scale model of borehole 18

As shown in Section 3.2.2 the models of borehole 17 were rather successful in matching the experimental evolution, both in terms of relative-humidity measurements during the experiment as well as in the measured water contents after excavation/dismantling. However, in borehole 18 some rather significant discrepancies between the modelled and experimental results were present. By simple visual examination of the bentonite just after excavation it was clear that a lot of water-transporting fractures had contributed to the hydration of the buffer, contrary to the case in the model where only one fracture was present. Furthermore, the buffer blocks near the bottom of the borehole was significantly wetter than the model predictions.

Given the tool at hand (FE-solver Code_Bright with pre-processor/meshing program GiD) it would have been extremely time consuming to include further fractures in the original geometry and instead a small-scale model was constructed. This only included the buffer, and nearby rock out to a radius of 0.6 m, see Section 2.2.2. In Figure 3-18 the RH evolution in the local-scale-geometry model is shown (dashed lines) and compared with the evolution in the large-scale-geometry model(solid lines). In this model the local-scale geometry was constructed with identical fracture properties as in the large-scale geometry As can be seen the agreement is relatively good given the large simplifications in the local-scale model, and as such we judge that it can be used to further explore the wetting of the buffer in borehole 18.

Two local-scale model were constructed in order to check whether 1) an improved fracture setup around borehole 18 could explain the discrepancies between the large-scale model results and the field data, and 2) a thin gap between the borehole wall and the bottom plate could help explain the high water-contents seen in the buffer blocks in the bottom of the borehole. The geometries used in these models are shown in Figure F-1 in Appendix F where also all further details on the setup of the models are given.

In Figure 3-19 the relative-humidity evolution in the bentonite form the local-scale-geometry model with an improved fracture setup is shown. It shows a somewhat better agreement with measured data as compared to the original large-scale-geometry model (see Figure 3-10) but the effect is rather marginal. In summary it can be said that while an improved relative-humidity evolution could be achieved by additional fracture-setup tuning, it is beyond the scope of our modelling to attempt this, at it would be highly labor intensive with most likely very little gain in process understanding.

The model which analyzed the effect of the open slot around the bottom plate is here only reported in terms of the final water content, which is shown in Figure 3-21. In the model, the only transport of water to the open slot comes via the vertical fracture intersecting the borehole. The transmissivity of this fracture was increase in the model to the value of the transmissivity of the horizontal fracture. As is seen in the figure the open slot around the bottom plate led to considerably higher water content in the bottom blocks. The increase in the transmissivity of the vertical fracture also led to too much wetting in the 288 degree direction; this could in principle be remedied by decreasing the transmissivity in the upper parts of the fracture.

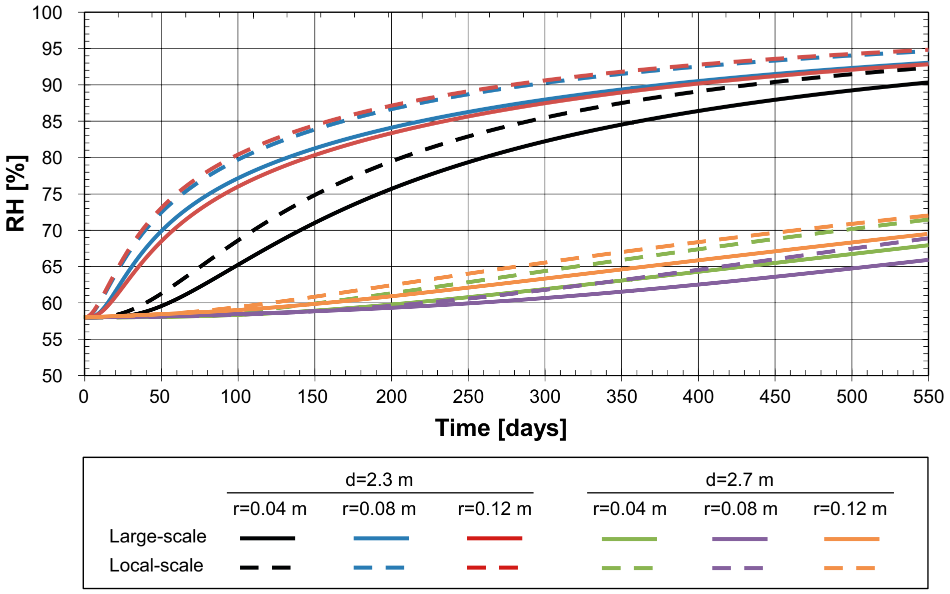

__Figure 3-18.__ RH senor evolution in the large-scale (solid lines) and local-scale (dashed lines) models. The geometry in the local-scale model presented in this graph was constructed so as to be identical to the large-scale-geometry model around the borehole. The two models agree relatively well with each other, although the local-scale model shows a slightly higher wetting rate.

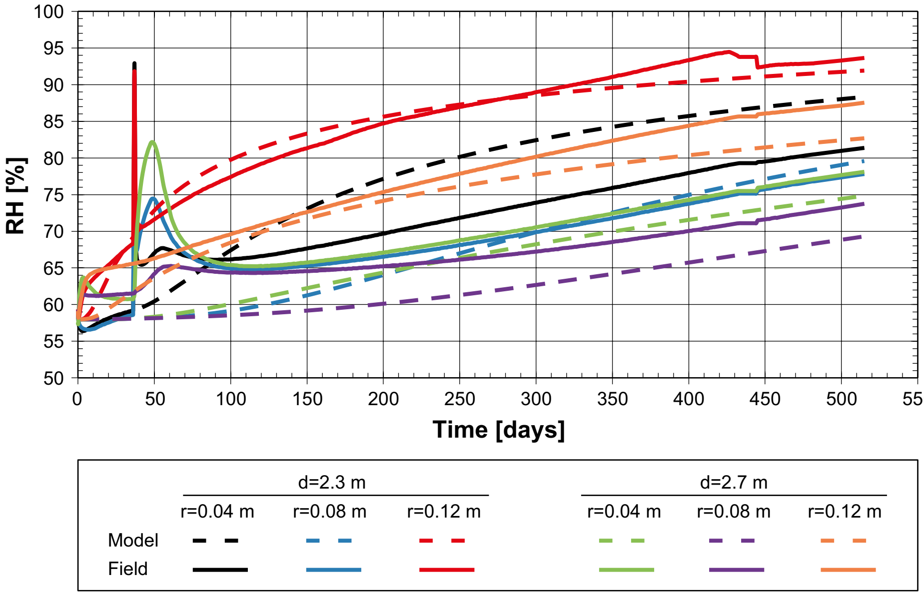

***Figure 3-19.** The relative humidity evolution in borehole 18. The model results comes from the simulation of the local-scale geometry with additional fractures intersecting the borehole.*

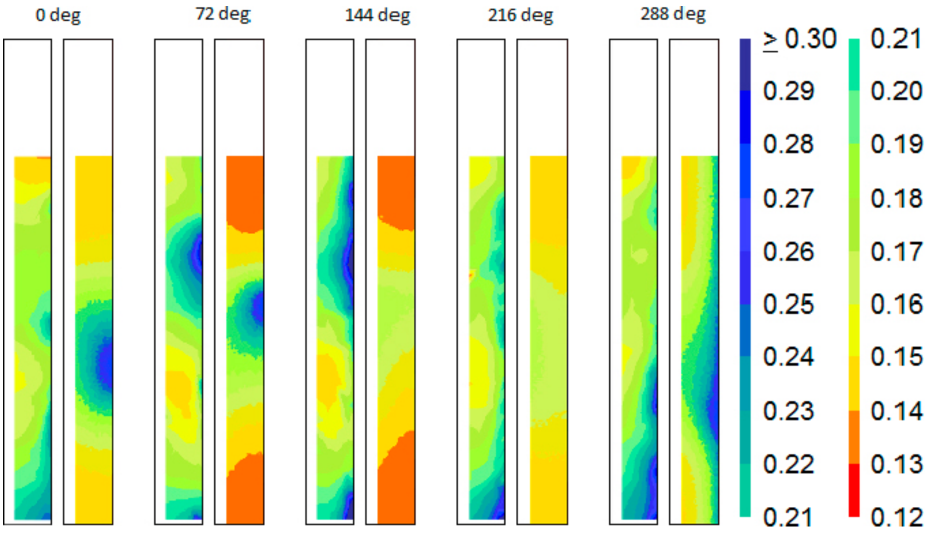

***Figure 3-20.** Contour plots of the water content in borehole 18 at the time of dismantling compared with measured data. Each pair of contour plots shows the data at the given direction, with experimental data on the left side and model data on the right side. The model results comes from the simulation of the local-scale geometry with additional fractures.*

The motivation for increasing the vertical fracture's transmissivity in the first place was that a model with the original transmissivity led to a much too small increase in the water content in the bottom parts. In principle the model could be made to reproduce the water content in the 288 degree direction better with additional tuning of the fracture transmissivity, however, this was considered beyond the scope of this report. The results nevertheless show, that in order to reproduce the water-content in the bottom parts of the borehole, the open slot around the bottom plate should be taken into account in the models.

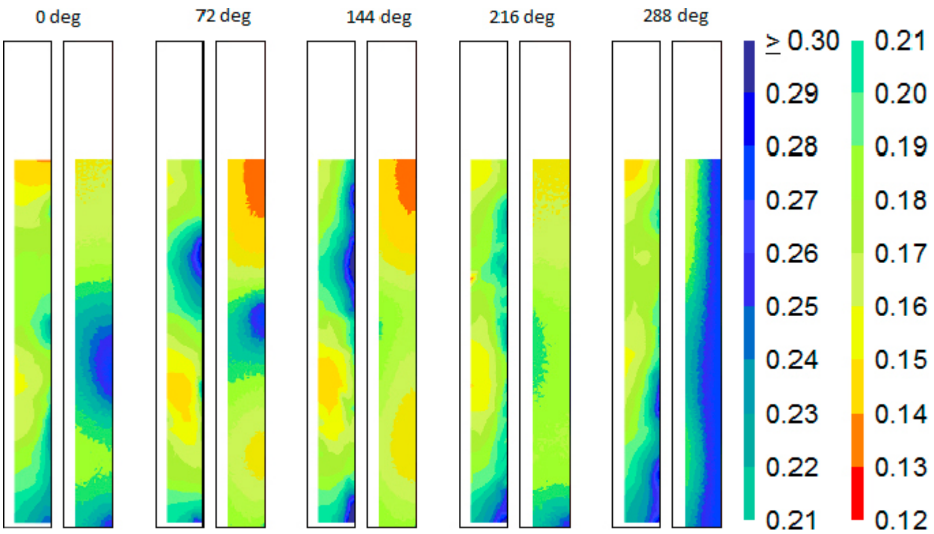

Figure 3-21. *Contour plots of the water content in borehole 18 at the time of dismantling. Each pair of contour plots shows the data at the given direction, with experimental data on the left side and model data on the right side. The model results comes from the model with an open column around the bottom plate and increased transmissivity of the vertical fracture.*

3.4 The relative permeability of the rock

The relative permeability of the rock is not as well studied as that of bentonite, at least not in the context of the Äspö granite. In the modelling done here a van Genuchten relation has been used. However, while this may be appropriate, some data on other types of granitic rock suggests that the shape of the relative permeability curve is actually quite different from a van Genuchten parameterization.

Vapor permeability measurements on granite mined on the Swedish west coast was presented in Hedenblad (1996). The measured data is shown in Figure 3-22 (left). Together with a specified water retention curve and an intrinsic permeability value, this data set was converted into the following relative permeability relation (see Figure 3-22 right, and Appendix H):

$$k_r(S) = \begin{cases} 5\cdot 10^{-4}\cdot S^2 & S<1 \\ 1 & S=1 \end{cases} \tag{3-1}$$

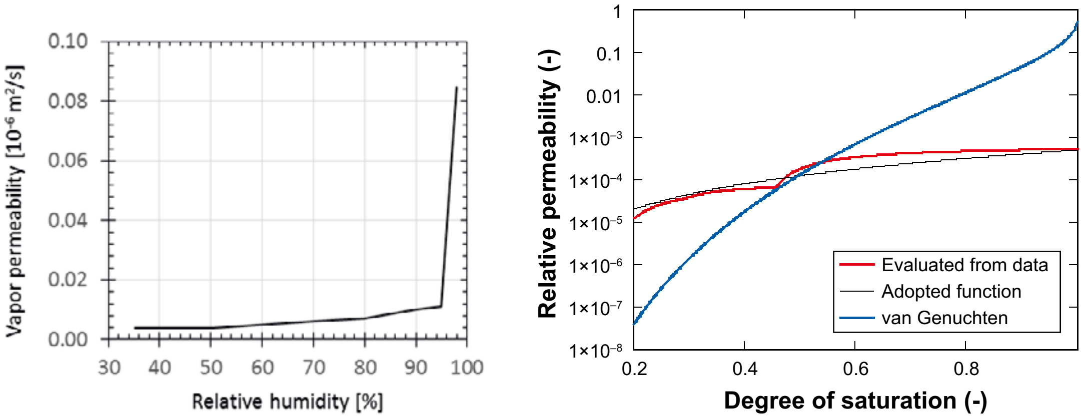

Figure 3-22. *Relation between vapor permeability and relative humidity as measured for granitic rock from the Swedish west coast left). Relative permeability relations (right): evaluated from vapor permeability data (red), adopted on the form in Equation 4-2 (black line), and the one provided with Task 8 (blue line).*

In combination with the DHR approach (see Section 2.2), this means that the DHR is essentially water saturated as soon as the pore pressure on the outside is slightly higher than atmospheric pressure. The flux through the DHR is therefore essentially proportional to the outside pressure. In particular, as the BRIE tunnel is open to the atmosphere, and hence there is a strong pressure gradient in the z-direction around the BRIE boreholes (see, for example, Figure 3-23), a relative permeability relation like that in Figure 3-22 would give rise to a strong depth dependence on the matrix flow.

As is seen in Figure 3-23 the pore pressure just outside the local drawdown around borehole 18 is about 10 bars near the bottom of the borehole, while it is zero at the top. If using a relative permeability relation like that in Figure 3-22 one would then expect a higher inflow in the bottom of the borehole.

In order to evaluate this new relative permeability relation a 2D axisymmetric model was constructed and simulated using COMSOL Multiphysics. The geometry of the model is shown in Figure 3-24. A variation of this geometry was also used, in which a single horizontal fracture at a depth of 2 m was included. In this figure the boundary conditions and hydraulic conductivity of the rock is also shown.

***Figure 3-23.** The average water pressures in the model about 3 months after installation of the bentonite.*

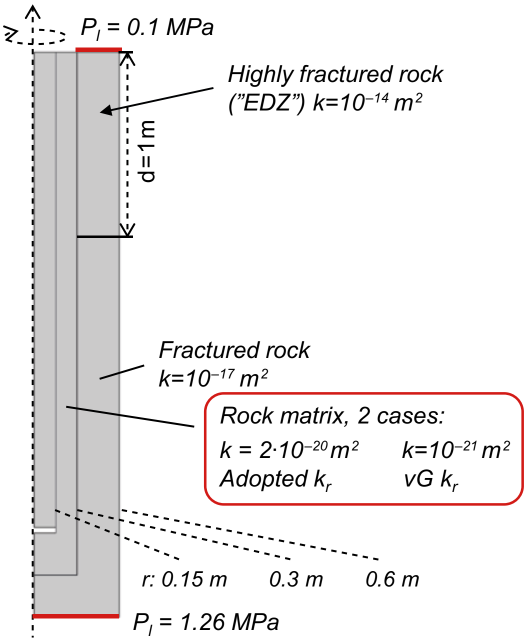

***Figure 3-24.** Geometry and boundary conditions in the 2D axisymmetric model simulated in Comsol Multiphysics. Also included in the picture is the hydraulic conductivity of the rock. The parameters of the bentonite was taken from the task description (see also Table 3-4).*

The buffer was modelled according to the task definition (see also Table 2-4); in the rock the relative permeability was set to $k_{rl} = 1$ in the (highly) fractured rock, while in the rock matrix both the standard van Genuchten relation (see Table 2-4) and a parameterization of the adopted new relation on the form:

$$k_{\mathrm{rl}} = \begin{cases} 5 \cdot 10^{-4} S_l^2 & S_l < 0.999 \\ f_{step}(S_l) & 0.999 < S_l < 1.0 \\ 1 & S_l \geq 1.0 \end{cases} \tag{3-2}$$

Here f_{step} (S_l) is a step function (Comsol built-in function) which defines a continuous function (with continuous first and second derivatives) between $5 \times 10^{-4} \times 0.99^2$ and 1. In total four models were simulated: for each geometry (with and without fracture) two models were simulated varying the relative permeability of the rock matrix. The results of the models, in terms of both the pressure profiles in the rock and water content in the buffer at the time of dismantling (after 420 days) are shown as contour plots over the entire geometry in Figure 3-25 (no fracture) and Figure 3-26 (fracture). In Figure 3-27 the axial water-content profiles are shown, together with experimental data (the error bars quantify the spread in experimental data in the five different directions in which the water content was analyzed).

As is seen in Figure 3-25 and Figure 3-26 the liquid pressure in the rock differs depending on which relative permeability relation is applied. The water content in the bentonite shows that while the van Genuchten relative permeability gives a rather constant axial water content distribution, the adopted relative permeability relation gives a strong depth dependence, where considerably more water has entered the bentonite which was situated at the bottom of the borehole than the bentonite situated further up. This picture is even more clearly seen in Figure 3-27 where the axial water content from the four models are plotted (r = 0.13 m) together with the measured water contents in the buffer in borehole 17.

The left panel shows the results from the model without a fracture, while the right panel shows the results when a horizontal fracture is included. As can be seen the red lines, which identify the models with the adopted relative permeability relation shows a clear depth dependence which, when adding a fracture, gives a water content profile that agrees rather well with measured data.

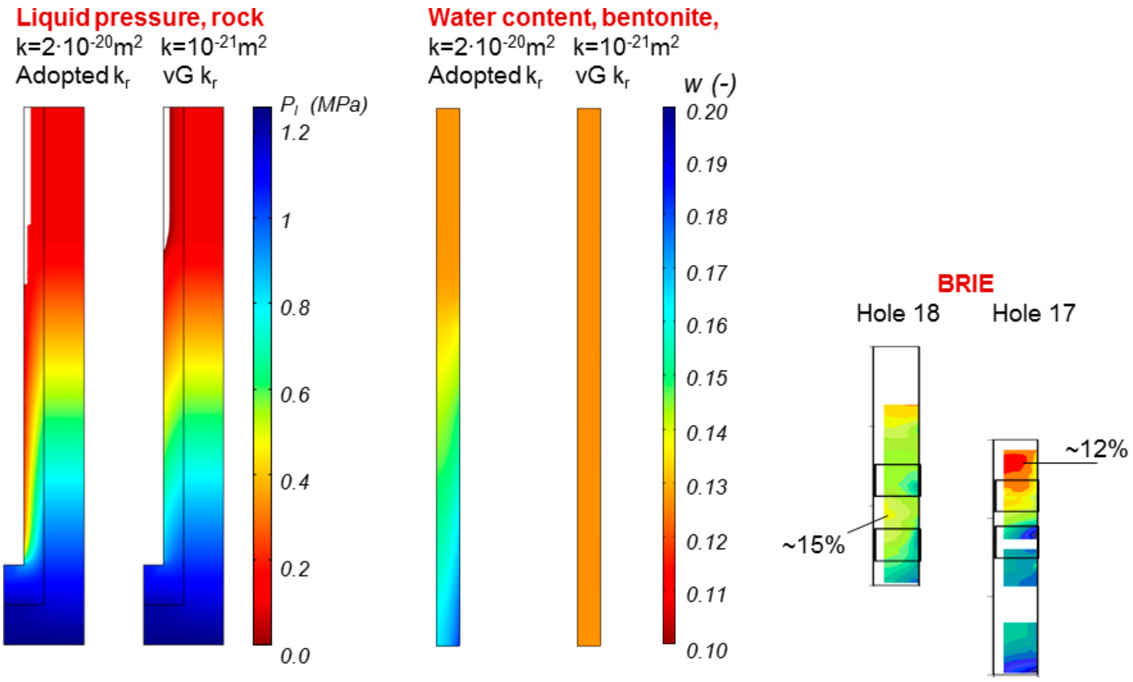

Figure 3-25. Water content after 420 days in the 2D axisymmetric model with no fracture.

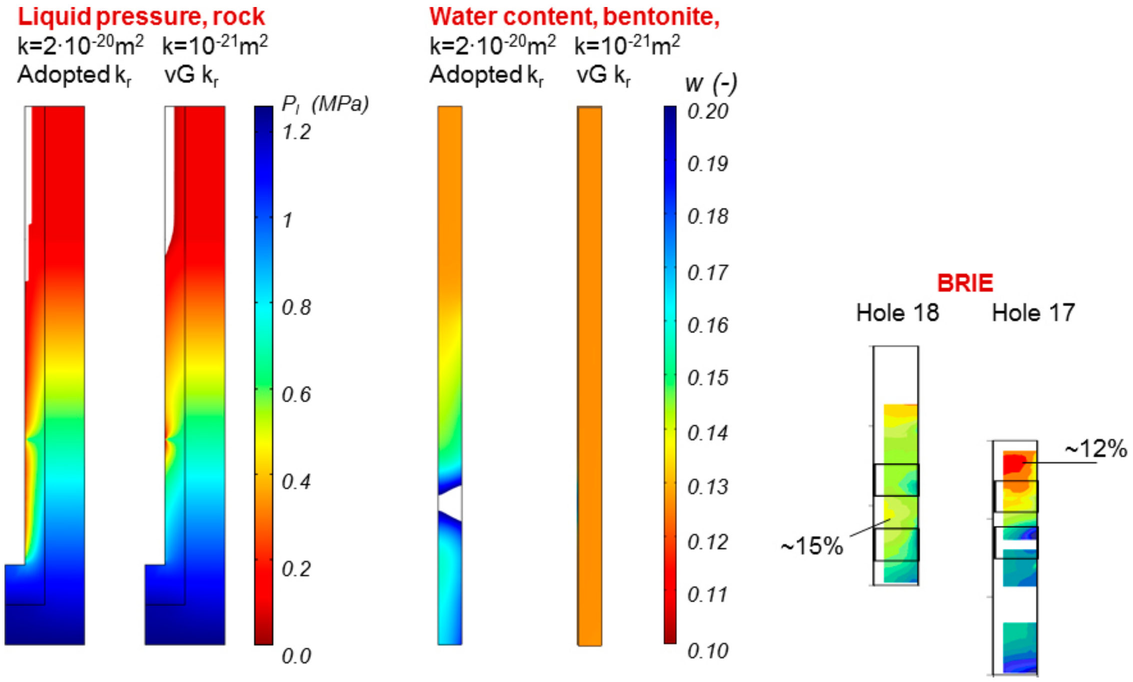

***Figure 3-26.** Water content after 420 days in the 2D axisymmetric model with a horizontal fracture.*

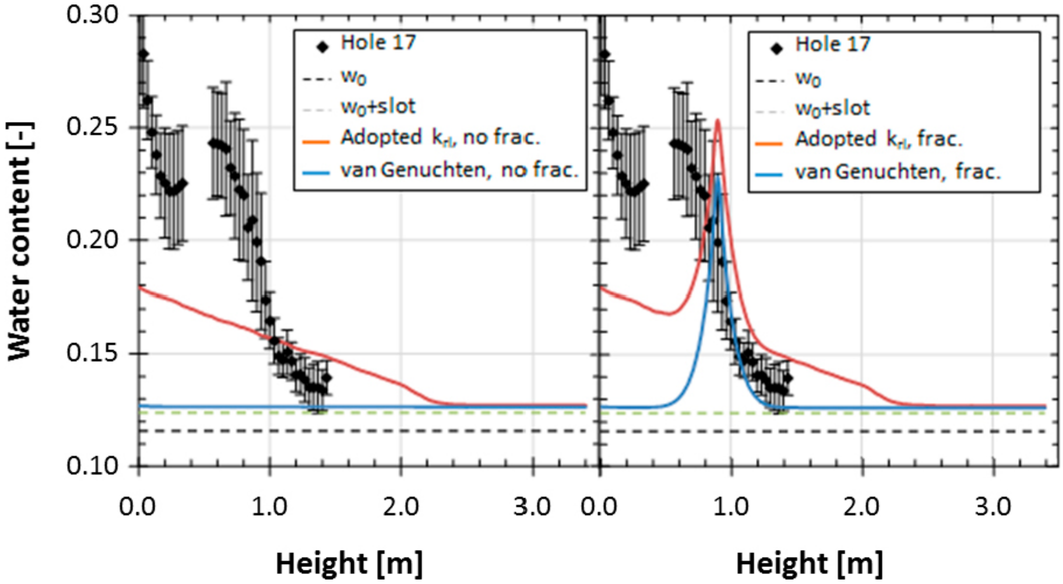

***Figure 3-27.** Axial water-content profiles 420 days in the 2D axisymmetric model without (left panel) and with (right panel) a horizontal fracture. The profiles are taken from a radius of r = 0.13 m (the buffer has an outer radius of 0.15 m). The black dots (with error bars) is the experimentally measured water content at the same radius at the time of dismantling in borehole 17.*

4 Discussion

Modelling the BRIE experiment has allowed us to develop our conceptual model of the rock and shown that it can be used to simulate the natural wetting of bentonite in a deposition hole, given that the inflow characteristics are known a priori. It is clear that modelling the wetting of bentonite in repository-like conditions is a very complex task, limited both by our understanding of the modelled system, as well as by uncertainties in the conceptual model and material parameterization and the site characterisation. In this section the, in our opinion, most important uncertainties are discussed.

4.1 Conceptual model uncertainty

When discussing the conceptual model used to construct our models, it is worth dividing it in to parts; the conceptual model of the bentonite and that of the rock.

The conceptual model of the bentonite which we use has been developed to represent the behaviour of the true system well.

As for the rock, the conceptual model is not meant to represent the full behaviour of the rock system, but instead to reproduce the inflow of water into the borehole/deposition hole, which it is able to do rather well during the saturation process of the bentonite. As such, while the behaviour of the rock system in the model is probably rather similar to that of the true system near the borehole, it is only correct to an order of magnitude on the large scale.

In the models used to predict the hydraulic evolution in the clay the major conceptual uncertainty is our treatment of the rock, with a radically different treatment of the near-field rock as compared to the large-scale rock.

The accuracy of this description of the rock was uncertain before the experiment (even if it had been used with success in our modelling of the Prototype repository), and parameter values used when implementing it (such as the matrix hydraulic permeability) was only known to an order of magnitude. Furthermore, this conceptualization meant that the accuracy of our predictions relied heavily on the field characterization, and thereby the uncertainties related to those measurements had a strong impact on the model uncertainties.

Using sensors data many of these uncertainties were reduced, and the comparison with experimental data shows that our treatment of the rock is able to reproduce the inflow characteristics in the field to a reasonably good degree.

The notion of a *bentonite-rock interface* was addressed in the objectives of BRIE and Task 8, and this topic therefore deserves a comment. In problems involving axial displacements in a deposition hole, it may be relevant to include so-called friction elements between the bentonite and the rock, but since the bentonite was axially confined in BRIE this was not necessary in Task 8. We realize that there may be zones with special hydraulic properties adjacent to the joint between the rock and the bentonite in the BRIE experiment, but these were handled either with the used material models or by disregarding them. For instance, the *initial gap* between the rock and the bentonite was filled with water immediately after installation, which in turn lead to its closure at an early stage. This was, together with the very small dimension of the gap, the motive for not including it in the model. Even if the filling of the gap was incomplete in some areas, and the moisture transfer across the gap in that case would be in the form of vapor diffusion, this would probably not mean that the water-uptake in the bentonite would be limited by the gap. A *dehydrated zone* in the rock close to the bentonite is another zone with special properties. And indeed, the flow coefficient of this zone may be crucial to for the overall hydration process (see Section 3.4). But the appropriate way to handle this is through the adoption of accurate material properties for the rock material, i.e. the water-retention curve and the relative permeability relation. The *high-resolution cylinder* (see Section 2.1) which is an important component in our conceptual model, can also be view as a zone between the bentonite and the overall rock mass. But in this case, it is the high-resolution cylinder that is represented with properties as accurate as possible, whereas the description of the homogenized treated fractured rock outside the cylinder is a simplification. There was therefore no motive for including any special interface material in our conceptual model during the course of the modeling task.

4.2 Site-characterisation and experimental uncertainties

The inflow into the boreholes was measured before installation. However, the values were uncertain, in particular with regards to the presence (or lack thereof) of a matrix flow. This resulted in a significant uncertainty in the matrix permeability in the early models of the experiment. The inflow values through the observed fractures reported in the task description were also uncertain. In particular in borehole 18 this led to a large discrepancy between model predictions and the actual evolution, as the initial characterization data was consistent with only matrix flow in the lower part of the borehole (assuming a matrix hydraulic permeability of about 10^{-20} m^2), and hence no fractures were included in the first set of models of this borehole.

Furthermore, the fracture mapping performed was not able to correctly determine the exact orientation and depth of the large fractures intersecting the boreholes, inevitably leading to large errors in the implementation of fractures intersecting the boreholes in our models. It also made it very difficult to calibrate the models using RH-sensors data, as their position with respect to the fractures were uncertain until the dismantling operation.

The implementation of the rock near the deposition hole, both in terms of matrix conductivity and fracture positions/flow were made directly from the characterization measurements of the BRIE site done before installation. The uncertainties in this characterization therefore directly translated in an uncertainty in the model prediction; both on the RH evolution at the instrumented positions and in terms of the predicted water content in the bentonite.

4.3 Parametrization uncertainty

All parameters used in our models are to some degree uncertain. What is interesting to discuss, however, is the parameters that have a significant impact on the hydraulic evolution.

Below we present a list of the parameters/features which, as evaluated from both the sensitivity analysis performed in Task 8a and our experiences during the modelling of Task 8d, are important to the saturation process and which we consider to be (highly) uncertain. A short qualitative analysis of how each of these parameters/features may contribute to the overall uncertainty in the prediction is also given.

- **Properties of the matrix flow:** By matrix flow we in general mean all water inflow into the borehole which does not enter through "large" fractures. This is a rather arbitrary definition, but in the context of the BRIE experiment we define the "large fractures" as those identified in the pre-characterization (2 in borehole 17 and 1 in borehole 18). The magnitude of the matrix flow is thus a very important factor in determining the hydraulic evolution; it is also perhaps the parameter which was most uncertain during the early modelling attempts, experimental measurements suggested that the hydraulic conductivity of the matrix should be in the interval $10^{-14} < k_m < 10^{-11}$ m/s. If the higher of these values were to represent a good parametrization the bentonite would probably be fully saturated within less than one year after installation (i.e. before dismantling), while a value in the lower range would mean that the time until saturation is set by the fracture inflow and can be expected to be at least several decades (conclusions on saturation times here comes mainly from the sensitivity analysis done in Task 8a).

- **Properties of the “main” fractures:** The “main” fractures are here defined as the borehole-intersecting fractures which were detected in the pre-characterization, as well as those identified in the post-dismantling analysis of the buffer. As was evident from the water-content distribution in the buffer, the water flow through these fractures is very high compared to the matrix flow, and as such they completely determine the water uptake in the bentonite near the fractures. Even though the flux which enters the bentonite via the fractures are limited by the low hydraulic conductivity of the bentonite, they, given the very low matrix flow, have a significant impact on the water content at dismantling even several decimetres above and below the fractures. The properties of these main fractures, both spatial and hydraulic, were rather uncertain at the time of installation, which directly translates into a large uncertainty in the predictive ability of the models.
- **Mapping of “small” fractures:** As was seen during the excavation of the bentonite, in particular borehole 18 appears to have been intersected by many small fractures which contributed to the wetting of the bentonite, but were not detected during the pre-characterization. If one is to make a detailed prediction of the water inflow into the buffer in a particular borehole, detailed knowledge of the fracture characteristics would be needed.

5 Summary and conclusions

5.1 Summary

In this report the modelling of 1) the BRIE water-uptake-laboratory experiment and 2) the BRIE field experiment has been described. Both experiments were modelled using the FEM code Code_Bright.

The water-uptake experiment was modelled using a simple one-dimensional axisymmetric model, only including the bentonite clay and not the surrounding steel container. The modelling results showed that the hydraulic evolution is well reproduced using Code_Bright, and that the swelling of the clay in order to fill the gap initially present at the outer edge does not have a significant effect on the hydraulic evolution. Hence, when modelling the field experiment 1) the initial gap can be ignored and 2) the hydraulic parameters from the task description can be used.

The BRIE field experiment was modelled in full 3D using two sets of geometries: a large-scale geometry with both the TASO and TASD tunnels included, as well as a large volume of the surrounding host rock and a local-scale geometry with the borehole and just the nearby rock included. Using Code_Bright it is not possible to implement a discrete fracture network, and as such the transport properties of the rock around the experimental boreholes had to be handled in a simplified way. Everywhere except just around the boreholes the host rock was treated as a homogeneous material with an effective hydraulic conductivity, which is set so as to “smear out” the heterogeneous fracture and matrix flow into a homogeneous flow with the same magnitude. Only just around the boreholes was the host rock treated in a more detailed way; with a cylinder of low-permeability rock matrix intersected by fractures. The geometry and transport properties of these fractures were taken from the characterization done in the field prior to installation of the bentonite and in later models calibrated so as to reproduce the relative-humidity evolution and measured water-content data after dismantling.

The results of the modelling of the field experiment showed that with the characterization data available to us in Task 8D it was possible to predict the evolution in the field reasonably well in one of the boreholes (borehole 17), while the prediction of the evolution in borehole 18 was rather poor.

Using updated models, calibrated both during the experiment from relative-humidity data, as well as after dismantling using water content data and updated fracture geometries, it was possible to achieve an excellent match between modelled and experimental data for borehole 17 and an acceptable match in borehole 18.

5.2 Comments and recommendations

During the modelling of BRIE we have had the opportunity to develop and test our model conceptualisation and implementation, as well as to lean what the key properties of the site are with respect to the hydraulic evolution. In this section we have listed the, in our opinion, most important lessons learned from the modelling of task 8, divided into three categories; bentonite properties, rock properties, and site characterization properties.

Model conceptualisation

- The conceptual model in which the rock is treated as a homogeneous material everywhere except in a small cylinder around the borehole (where the rock is treated as consisting of low-conductivity matrix intersected by fractures) has been shown to reproduce the water-transport into the borehole very well (given à priori knowledge of the fractures)
- The small cylinder used in this task had a thickness of 0.15 m. A motivation for this thickness was sought through an analysis of the fracture statistics provided in the task description, and this suggested that a relevant thickness is closely related to the total fracture intensity.
- The rock outside the small cylinder has essentially only the function of supplying water at a specific pressure level. This meant that the geometry for Task 8F could be significantly reduced to a hollow cylinder with a thickness of 0.3 m. This implied that the numerical problem could be greatly simplified.

Bentonite parameterisation:

- The importance of the hysteresis behaviour of the water-retention curve: This behaviour was well known before Task 8, but its importance became clearer during this project.
- One aspect of this was that the bentonite apparently can be in equilibrium with a slowly increasing relative-humidity level (increase of 8 percentage points), even though no water-content increase could be detected.
- Another aspect was that different bentonite blocks could exhibit different initial relative-humidity levels even though they were prepared from the same batch and had the same water content. This could possibly be related to the ambient climate during the manufacturing of the blocks.
- Verification of hydraulic material model: The modelling of the different water-uptake tests showed that our conceptual model of the bentonite, as implemented in Code_Bright, as well as the parameter set adopted for Task 8, is able to model the hydraulic evolution with a high degree of accuracy.

Rock parameterisation:

- The water-retention curve adopted for Task 8 from experimental data obtained in the BRIE project appears to work well. The corresponding retention curve provided in the initial phase of Task 8 was based on measurements at Grimsel Test Site (Finsterle and Pruess 1995).
- The value of the rock-matrix permeability was bounded to some extent during the course of the modelling task. In the last models of both Hole 17 and 18, which displayed the best agreement with experimental data, the matrix permeability was set to 10^{-21} m^2. In comparison, the corresponding hydraulic conductivity values measured on core samples in the BRIE project was generally higher (10^{-14}–10^{-11} m/s).
- A van Genuchten type relative permeability relation, motivated by the measurements at the Grimsel Test Site mentioned above, was used throughout the modelling task. An alternative relation was evaluated from vapour permeability data for granite samples found in the literature, and this relation was found to imply that the flux through the low-conductivity matrix was more sensitive to the pressure level outside the zone of influence. This could in turn mean that higher matrix permeability values, more consistent with independent conductivity measurements, could potentially be used for Task 8 with good agreement with experimental data. However, since the alternative is essentially discontinuous, it appears to be very difficult to use in a finite element code.

Site characterisation:

- A relevant site characterization is essential for making predictions of the hydration of buffer and backfilling a repository. The following measurements appears to be of importance:
  - Detailed mapping and quantification of the water inflow to the deposition holes and tunnels.
  - Quantification of the pressure distribution around the deposition holes and tunnels. This does not necessarily mean that extensive measurements are required, since large-scale flow models may be sufficient. Still, in order to calibrate the representation of fractures in the local model, it is necessary to relate the water inflow to a pressure distribution.
  - Characterization of the local fracture statistics. This may be important for assessing the size of the zone on influence in local model.
  - Active methods, e.g. pump tests, can potentially be valuable, although this has not been demonstrated in the modelling work.
- Uncertainties in the position/orientation if intersecting fractures makes it very difficult to calibrate models using sensor data.

Future work:

- It would be valuable to perform analyses of DFN models concerning: i) the equivalent conductivity and its scale-dependence, and ii) the zone of influence around deposition holes.
- It would also be valuable to perform vapor permeability measurements of rock samples from Äspö at well as from the Forsmark area.

References

SKB's (Svensk Kärnbränslehantering AB) publications can be found at www.skb.se/publications.

Arfvidsson J, Claesson J, 2000. Isothermal moisture flow in building materials: modelling, measurements and calculations based on Kirchhoff's potential. Building and Environment 35, 519–536.

Birgersson M, Karnland O, 2014. Summary of Clay Technology's work within FORGE. In Sellin P (ed). Experiments and modelling on the behaviour of EBS. FORGE Report D.3.38, 217–231.

Darcel C, 2003. Äspö Hard Rock Laboratory. True Block Scale continuation project. Assessment of the feasibility of tracer tests with injection in "background fractures" using a model based on a power law fracture length distribution. SKB IPR-03-41, Svensk Kärnbränslehantering AB.

Dueck A, 2004. Hydro-mechanical properties of a water unsaturated sodium bentonite: laboratory study and theoretical interpretation. PhD thesis. Lund University.

Dueck A, Nilsson U, 2010. Thermo-hydro-mechanical properties of MX-80. Results from advanced laboratory tests. SKB TR-10-55, Svensk Kärnbränslehantering AB.

Finsterle S, Pruess K, 1995 Solving the estimation-identification problem in two-phase flow modeling. Water Resources Research 31, 913–924.

Follin S, Stigsson M, Svensson U, 2005. Variable-density ground water flow simulations and particle tracking – numerical modelling using Darcy Tools. Preliminary site description Simpevarp subarea – version 1.2. SKB R-05-11, Svensk Kärnbränslehantering AB.

Fransson Å, Åkesson M, Andersson L, 2016. Bentonite Rock Interaction Experiment. Characterization of rock and installation, hydration and dismantling of bentonite parcels. SKB R-14-11, Svensk Kärnbränslehantering AB.

Hedenblad G, 1996. Materialdata för fukttransportberäkningar. Stockholm: Byggforskningsrådet. (In Swedish.)

Hedström M, Ekvy Hansen E, Nilsson U, 2016. Montmorillonite phase behavior. Relevance for buffer erosion in dilute groundwater. SKB TR-15-07, Svensk Kärnbränslehantering AB.

Lambe T W, 1973. Predictions in soil engineering. Géotechnique 23, 151–202.

Vidstrand P, Åkesson M, Fransson Å, Stigsson M, 2017. Task 8 of SKB Task Forces EBS and GWFTS: Modelling the interaction between engineered and natural barriers – An assessment of a fractured bedrock description in the wetting process of bentonite at deposition tunnel scale. A compilation of Task 8 descriptions. SKB P-16-05, Svensk Kärnbränslehantering AB.

Vilks P, 2007a. Forsmark site investigation. Rock matrix permeability measurements on core samples from borehole KFM01D. SKB P-07-162, Svensk Kärnbränslehantering AB.

Vilks P, 2007b. Oskarshamn site investigation. Rock matrix permeability measurements on core samples from borehole KLX03. SKB P-07-204, Svensk Kärnbränslehantering AB.

Åkesson M, Börgesson L, Kristensson O, 2010. SR-Site Data report. THM modelling of buffer, backfill and other system components. SKB TR-10-44, Svensk Kärnbränslehantering AB.

Appendix A

Theoretical foundation of Code_Bright

A.1 Theory

The modelling presented here has, with one exception, been purely hydraulic. Therefore, in the following description of the thermodynamic continuum formulation used in Code_Bright, only H-processes are considered. Thermal (energy balance) and mechanical (momentum balance) processes have been ignored.

The theory is based upon a traditional geomechanical porous formulation, in which the material is treated as a mixture of the constituents

- minerals,
- liquid water,
- dissolved air,
- water vapour, and
- dry air.

The constituents are then divided into: minerals (*m*), water (*w*), and air (*a*) and an assumption of immiscible phases (*p*): solid (*s*), liquid (*l*), and gas (*g*) are made. From the structural assumptions of the mixture, primitive entities may be defined

- mixture volume element (dv),
- solid volume (dv_s),
- pore volume (dv_p),
- liquid volume (dv_l), and
- gas volume (dv_g).

Further primitive entities, regarding mass and energy are introduced for the constituents

- solid mass ($dm_s^m = dm_s$),
- water mass in liquid (dm_l^w),
- air mass dissolved in liquid (dm_l^a),
- water mass in gas (i.e. water vapor mass) (dm_g^w),
- dry air mass in gas (dm_g^a).

With use of the primitive entities the definitions below are formulated

- porosity ($n = dv_p/dv$),
- solid density ($\rho_s = dm_s/dv_s$),
- liquid water mass per liquid phase volume ($\theta_l^w = dm_l^w/dv_l$),
- dissolved air mass per liquid phase volume ($\theta_l^a = dm_l^a/dv_l$),
- water vapor mass per gas phase volume ($\theta_g^w = dm_g^w/dv_g$),
- dry air mass per gas phase volume ($\theta_g^a = dm_g^a/dv_g$),
- liquid degree of saturation ($S_l = dv_l/dv_p$), and
- gas degree of saturation ($S_g = \mathrm{dv_g/dv_p}$).

Using the entities above, the water mass and air mass per mixture volume element can be expressed as,

$$\frac{dm^w}{dv} = \frac{dm_l{}^w + dm_g{}^w}{dv} = \theta_l{}^w S_l n + \theta_g{}^w S_g n \quad \text{and}$$

$$\frac{dm^a}{dv} = \frac{dm_l{}^a + dm_g{}^a}{dv} = \theta_l{}^a S_l n + \theta_g{}^a S_g n,$$

respectively. If introducing source terms $\{f^w, f^a\}$ and fluxes of water and air in the liquid and gas phase, $\{\boldsymbol{j}_l^w, \boldsymbol{j}_l^a\}$ and $\{\boldsymbol{j}_g{}^w, \boldsymbol{j}_g{}^a\}$, the continuity equations,

$$\frac{\partial}{\partial t}\left(\theta_l{}^w S_l n + \theta_g{}^w S_g n\right) + \nabla\cdot\left(\boldsymbol{j}_l{}^w + \boldsymbol{j}_g{}^w\right) = f^w \text{ and}$$

$$\frac{\partial}{\partial t}\left(\theta_l{}^a S_l n + \theta_g{}^a S_g n\right) + \nabla\cdot\left(\boldsymbol{j}_l{}^a + \boldsymbol{j}_g{}^a\right) = f^a ,$$

can be formulated for water and air mass, respectively.

To close the formulation, variables are selected as independent (p_l, p_g) or dependent and material specific constitutive relations are specified where dependent variables are given by expressions of independent variables. In the formulation used within Code_Bright a phenomenological approach towards specifying the constitutive relations is adopted. Below, when describing the used constitutive laws, functions that give values of variables are indicated with ~ above the variable name.

The advective mass fluxes are taken to be described by Darcy's law,

$$\boldsymbol{j}_l{}^w = \theta_l{}^w \boldsymbol{q}_l{}^w = \theta_l{}^w \frac{-\boldsymbol{k}k_{rl}}{\mu_l}(\nabla p_l - \rho_l \boldsymbol{g}) \text{ and } \boldsymbol{j}_g{}^a = \theta_g{}^a \boldsymbol{q}_g{}^a = \theta_g{}^a \frac{-\boldsymbol{k}k_{rg}}{\mu_g}(\nabla p_g - \rho_g \boldsymbol{g}),$$

where the relative permeabilities, k_{rl} and k_{rg}, are given by

$$\tilde{k}_{rl}(S_l) = A_l S_l{}^{\delta_l} \text{ or } \sqrt{S_l}\left(1-(1-S_l{}^{1/\lambda})^{\lambda}\right)^2 \text{ and } \tilde{k}_{rg}(S_g) = A_g S_g{}^{\delta_g},$$

respectively, and $\boldsymbol{g}=-9.81\boldsymbol{e}_z$.

The diffusive mass fluxes are taken as described by Fick's law,

$$\boldsymbol{j}_g{}^w = -\tau n \rho_g S_g D_m{}^w \boldsymbol{I}\nabla\left(\theta_g{}^w / \rho_g\right) \text{ and } \boldsymbol{j}_l{}^a = -\tau n \rho_l S_l D_m{}^a \boldsymbol{I}\nabla\left(\theta_l{}^a / \rho_l\right),$$

where the diffusion coefficients, $D_m{}^w$ and $D_m{}^a$, are given by,

$$\tilde{D}_m{}^w(p_g,T) = D^w(273.15+T)^n / p_g \text{ and } \tilde{D}_m{}^w(T) = D^a \exp(-Q/(R(273.15+T))),$$

respectively.

The liquid degree of saturation is related to the liquid pressure by use of a retention law, here an expression of van Genuchten:

$$\tilde{S}_l(p_l,p_g) = \left(1+\left(\frac{p_g-p_l}{p_0}\right)^{1/(1-\lambda)}\right)^{-\lambda},$$

and from the definitions, the gas degree of saturation is given by $\tilde{S}_g(p_l, p_g) = 1 - \tilde{S}_l(p_l, p_g)$.

Below it is used that $p_g = p_a + p_v$. The relation $\rho_l = \theta_l{}^a + \theta_l{}^w$ holds for the "liquid phase densities". Here,

$\tilde{p}_l(p_l, T) = p_{l0} \exp(\beta(p_l - 0.1) - \alpha T)$, $\tilde{\theta}_l{}^a(p_l,p_g,T) = \tilde{\rho}_l(p_l,T)(p_g - \tilde{p}_v(T))\dfrac{M_a}{HM_w}$, and

$\tilde{p}_v(T) = 136\,075 \exp(-5\,239.7(273.15+T))$ are used. The relation $\rho_g = \theta_g{}^a + \theta_g{}^w$ holds for the "gas phase densities". Here,

$$\tilde{\theta}_g{}^a(p_g,T) = \frac{(p_g - \tilde{p}_v(T))M_a}{R(273.15+T)} \text{ and } \tilde{\theta}_g{}^w(p_l,p_g,T) = \frac{\tilde{p}_v(T)M_w}{R(273.15+T)}\exp\left(\frac{-(p_g-p_l)M_w}{R(273.15+T)\tilde{\rho}_l(p_l,T)}\right)$$

are used.

Left to be specified are the viscosities of the liquid and gaseous phases,

$$\tilde{\mu}_l(T) = 2.1\cdot 10^{-12}\exp\left(\frac{1808.5}{273.15+T}\right) \text{ and } \tilde{\mu}_g(p_g,T) = 1.48\cdot 10^{-12}\left(\frac{\sqrt{273.15+T}}{1+\dfrac{119.4}{273.15+T}}\right)\frac{1}{1+\dfrac{0.14-1.2\cdot 10^{15}k}{p_g}}$$

respectively.

The now closed formulation may be solved for the adopted independent variables: liquid pressure and gas pressure. Here, however, a constant gas pressure ($p_g = 0.1$ MPa) has been used. Thus, liquid pressure becomes the unknown to be solved for.

Appendix B

BRIE water uptake experiment – Additional information on modelling setup

B.1 Task 8 – BRIE water uptake test

The BRIE water uptake test provides an excellent test bed of our hydraulic material model used to describe the buffer material.

Two types of models were done: 1) Hydro-Mechanical (HM) and Hydraulic (H) models with comparable parameters aimed at determining the influence of the gap between the bentonite and the confining wall on the hydraulic evolution, and 2) H models which explored the hydraulic parameters (in particular the relative permeability law) to find the best possible agreement with experimental data.

B.2 Objectives

The BRIE water uptake test gives us the opportunity to:

1) Check the influence of mechanical processes (i.e. swelling) on the hydraulic evolution.
2) Verify the hydraulic material model and parameters used to describe the buffer.

B.3 Approach

The water uptake experiment consists of a 100 mm thick buffer cylinder with a radius of 149 mm and a central hole with a radius of 20 mm. The buffer block is contained within a steel cylinder, with an inner radius of 150 mm and inner thickness of 100 mm. The inner hole in the buffer block is filled with a PVC dummy, representing the central tube in the field experiment. Thus, the water uptake experiment is to a high degree an exact representation of a 100 mm thick horizontal cut of the buffer in the field experiment. The buffer is given free access to water using a plastic filter on the outer vertical boundary.

B.4 Model setup

As outlined above two sets of models, with different objectives, were constructed. A brief description of the setup of the two types of models is given below. Further details can be found in Appendix B. Both sets of models were done using Code_Bright v4 and the bentonite block was represented using a one-dimensional axisymmetric geometry.

B.4.1 Initial-gap models – Material properties and geometry

Two sets of models were simulated, one purely hydraulic (H), and one coupled hydro-mechanical (HM). Only the HM model includes the outer gap, the H model is assumed to be radially homogenized and is only meant to act as a reference for the evolution in the HM model.

The retention curve is set according to the van Genuchten's relation (see (B-1), while the relative permeability is set using a power law (see Equation (B-2)).

$$S_l = \left[1 + \left(\frac{\Psi}{P_0}\right)^{1/_{1-\lambda}}\right]^{-\lambda} \tag{B-1}$$

$$k_{rl} = S_l^{\delta}, \tag{B-2}$$

The parameters used in these relations, together with the intrinsic permeabilities, are:

Material	K_0 [m/s]	P_0 [MPa]	λ [-]	δ [-]
Bentonite	6.4×10^{-14}	7.06	0.245	3
Gap	1×10^{-8}	0.1	0.3	0

The mechanical behavior of the bentonite is modelled using the Basic Barcelona Model (BBM). The elastic properties are:

Material	κ_{i0} **[-]**	κ_{s0} **[-]**	K_{min} **[MPa]**	ν **[-]**	α_{ss} **[-]**	α_{sp} **[-]**	α_i **[-]**	p_{ref} **[MPa]**
Bentonite	0.12	0.3	20	0.2	0	*	−0.01	1

*The α_{sp} parameter is replaced by an in-house development of the code (see Åkesson et al. 2010).

The yield surface is defined by the plastic parameters. These are set from the target void-ratio, e_T, which is here set rather high to allow for the substantial swelling which occurs early on in the gap. The parameters used are:

Material	e_T **[-]**	λ_0 **[-]**	r **[-]**	β **[MPa^{-1}]**	ρ **[°C^{-1}]**	k **[-]**	p_{s0} **[MPa]**	p_c **[MPa]**	M **[-]**	α **[-]**	e_0 **[-]**	p_0* **[MPa]**
Bentonite	1.3	0.37	0	0	0	0	0.298	1	0.4	0.5	0.752	2.601

The geometry of the model, with mesh and materials, is shown in Figure B-1. The mesh consists of 54 quadrilateral elements, with 52 in the bentonite and 2 in the gap.

B.4.2 Hydraulic-parameter evaluation models

The water-uptake test was modelled with a 1D axisymmetric geometry, see Figure B-2. The block was described as homogenized with a single constant porosity (44 %). The initial degree of saturation (42 %) was applied with an initial suction value of 90 MPa and the adopted retention curves. The initial water filling of the outer slot was taken into account by applying water saturated conditions from the start in the outer 5 mm of the bentonite (corresponding to an additional water volume of 0.12 liters for a height of 0.1 m). The liquid pressure at the outer boundary was kept constant at an atmospheric level (0.1 MPa) throughout the calculations. The used parameter values are shown in Table B-1. The models were run for 203 days, at a constant gas pressure of 0.1 MPa, at a constant temperature of 20 °C (which implies a constant viscosity), and with no gravity. The geometry was discretized as an array of 130 elements. Four different model cases were analyzed according to Table B-2.

The water-uptake was evaluated as the flow rate for the entire circumference, and adjusted for a block height of 0.1 m. Moreover, an initial inflow 0.2 litres was added to the water-uptake (0.08 litres representing the filter volume, and 0.12 litres volume of the outer slot, see above).

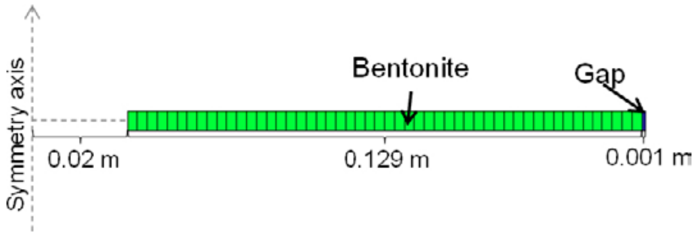

Figure B-1. *Geometry and mesh used when modelling the lab experiment.*

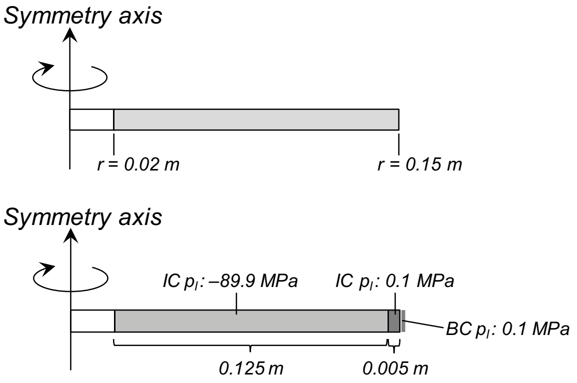

Figure B-2. *Model geometry (left) and model initial and boundary conditions (right).*

Table B-1. Parameter values.

Parameter		Value		
Porosity	n (-)	0.44		
Intrinsic permeability	k (m^2)	6.4×10^{-21}		
Relative permeability	k_r (-)	S_l^3	or	S_l^4
Water retention curve		van Genuchten law: P_0: 10 MPa; λ: 0.28	or	Square law1): P_0: 19.3 MPa
Water density	ρ_l (kg/m^3)	1 000		
Water viscosity	μ_l (Pa·s)	0.001		

[1] $S_l(\Psi) = (1 + \Psi/P_0)^{-1/2}$

Table B-2. Model cases.

Model	Relative permeability	Water retention curve
BRIEVUF_6	S_l^3	van Genuchten law: P_0: 10 MPa; λ: 0.28
BRIEVUF_7	S_l^4	van Genuchten law: P_0: 10 MPa; λ: 0.28
BRIEVUF_8	S_l^3	Square law: P_0: 19.3 MPa
BRIEVUF_9	S_l^4	Square law: P_0: 19.3 MPa

B.4.3 Boundary and initial conditions

The mechanical boundary conditions are: No vertical displacement is allowed on the outer horizontal borders, and no horizontal displacement is allowed on the outer vertical borders. For the hydraulic part, we prescribe zero suction over the gap at all times and no-flow over all boundaries except the outer vertical one, where atmospheric pressure ($P_l = 0.1$ MPa) is prescribed at all times.

In the experiment the bentonite had an initial void ratio of $e = 0.752$, corresponding to an intimal dry density of 1 587 kg/m^3, while the gap has $e = 999$ (its porosity is set to 0.999 to mimic air). The initial water content of the bentonite was 11.75 %; hence the initial saturation is set equal to 0.435. These initial conditions are prescribed for the HM model. For the pure hydraulic models the homogenized porosity of 0.44 is assumed from the start of the model, together with an initial saturation of 0.42.

The RH humidity measurements show that initially the RH was 51–52 % in the two blocks comprising Test 1 and 2. An RH value of 51 % corresponds to an initial suction of 90 MPa (from Kelvin's law with $\rho_l = 1\,000$ kg/m^3 and $T = 15$°C), which is taken as the starting point. The retention curve is chosen such that the initial suction and saturation values are correct, and also that it follows experimental data points in the in-situ retention data set (see Fransson et al. 2016).

B.5 Results

The results of the two sets of models are discussed separately below.

B.5.1 Initial-gap models

In Figure B-3 the total water intake in the HM model is compared with data from a pure H model (hence where no outer gap is included and the pore volume remains constant). As can be seen, the two are close to identical. It should also be pointed out that the gap in the model closes almost immediately after installation. Hence, its influence on the water transport, in the case where the gap is artificially saturated immediately after bentonite installation, is negligible.

B.5.2 Hydraulic parameter evaluation models

The model results are shown in Figure B-4 – Figure B-6. The modelled evolution of RH at the radii 0.04, 0.08 and 0.12 m are shown together with data from the RH sensors in Test 1 in Figure B-4. Modelled saturation profiles for day 0, 107 and 203 are shown in Figure B-5 together with measured saturation profiles at the dismantling of Test 1 and 2. The modelled water-uptake is shown in Figure B-6 together with the measured cumulative water-uptake in Test 1. The water-uptake was evaluated as the flow rate for the entire circumference, and adjusted for a block height of 0.1 m. Moreover, an initial inflow of 0.2 litres was added to the water-uptake (0.08 litres representing the filter volume, and 0.12 litres representing the volume of the outer slot).

The models with a cubic power law generally display a better agreement than the models with the fourth order power law concerning the experimental water-uptake data (Figure B-6). In contrast, the models with the fourth order power law generally display a better agreement with the measured RH-evolution (Figure B-4) and the measured saturation profiles (Figure B-5). In addition, it can be noted that the models with the van Genuchten retention curve generally display a faster hydration than the models with the square-law retention curve (e.g. see the red curves in Figure B-5).

The difference in adopted parameters for different data sets correspond to the minor inconsistency in the overall water balance for the water uptake tests, especially for Test 2, which may be caused by elastic expansion during the dismantling of the test, or that water was lost from the water supply reservoir during the test period (see Fransson et al. 2016).

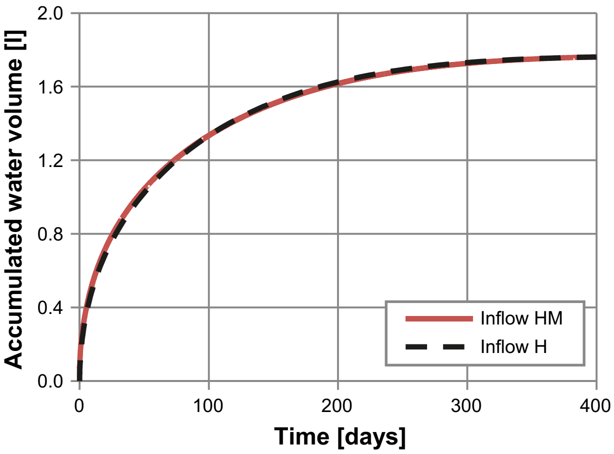

Figure B-3. Cumulative water uptake in the H and HM models. As can be seen the evolutions is almost identical, hence the influence of the gap on the hydraulic evolution is very small.

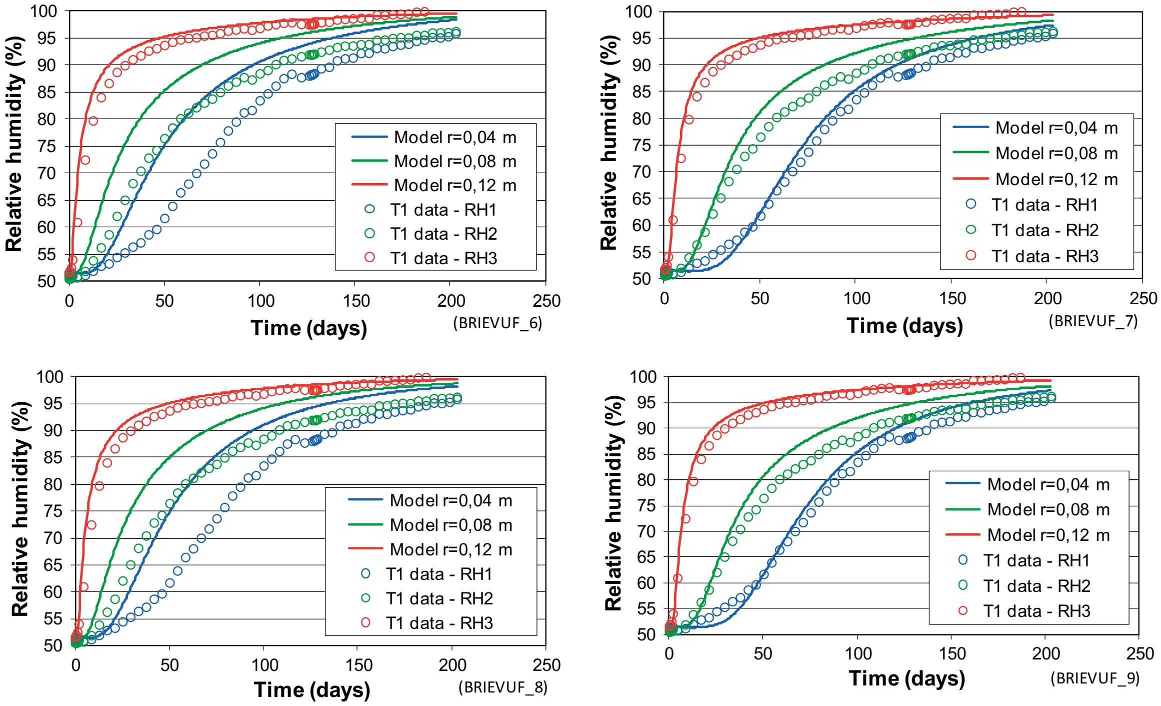

Figure B-4. *Modelled evolution of RH at three radii and data from RH sensors in Test 1; van Genuchten retention curve (upper graphs); square law retention curve (lower graphs).* $k_r(S_l) = S_l^3$ *(left graphs); and* $k_r(S_l) = S_l^4$ *(right graphs).*

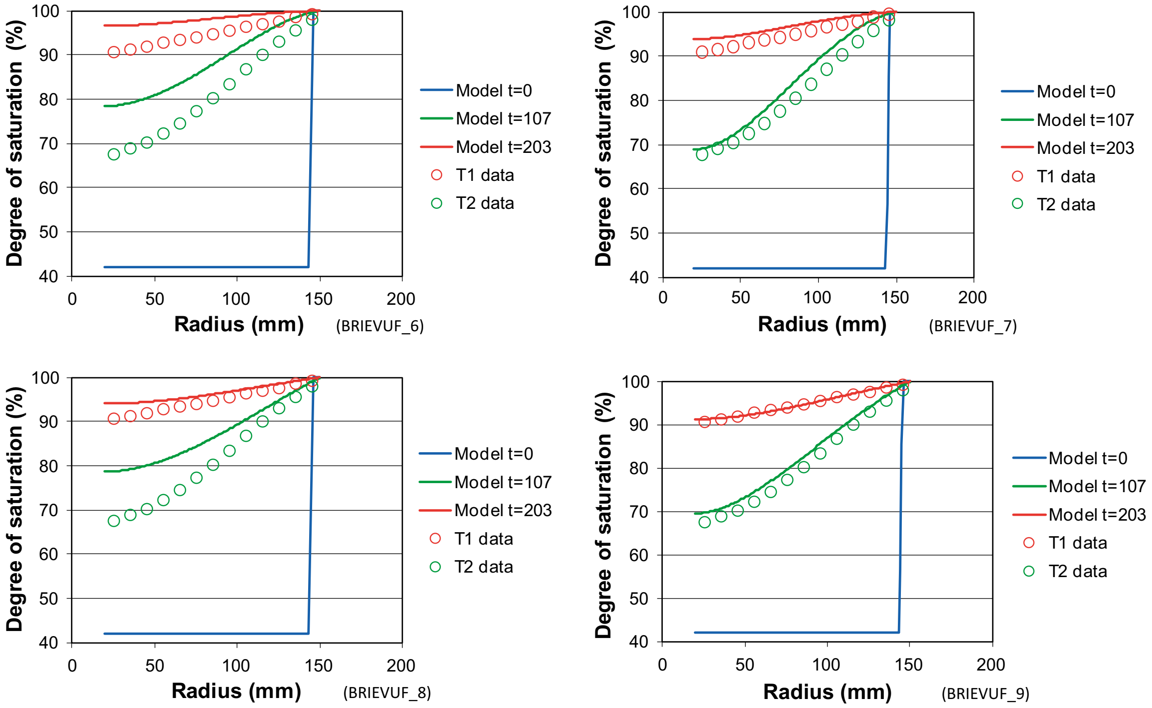

Figure B-5. *Modelled saturation profiles at day 0, 107 and 203 and measured data from Test 1 and Test 2; van Genuchten retention curve (upper graphs); square law retention curve (lower graphs).* $k_r(S_l) = S_l^3$ *(left graphs); and* $k_r(S_l) = S_l^4$ *(right graphs).*

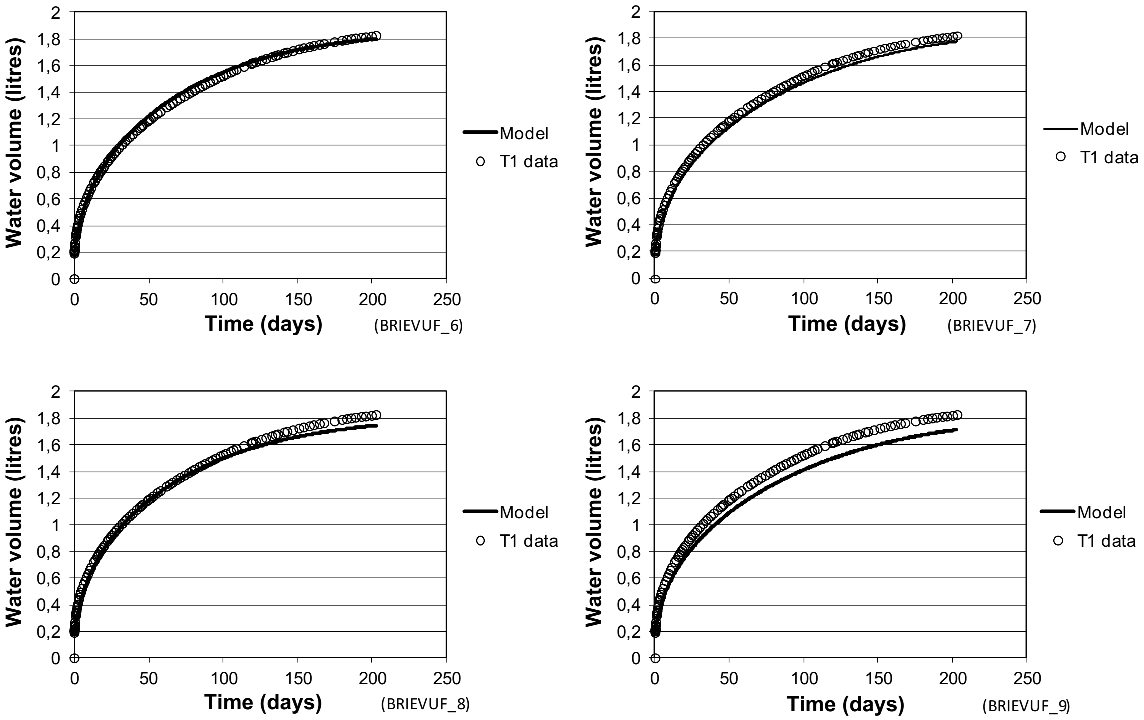

Figure B-6. *Modelled cumulative water uptake and measured data from Test 1; van Genuchten retention curve (upper graphs); square law retention curve (lower graphs).* $k_r(S_l) = S_l^3$ *(left graphs); and* $k_r(S_l) = S_l^4$ *(right graphs).*

B.6 Conclusions and recommendations

The modelling of the laboratory experiment allows us to draw two very important conclusions: 1) the initial gap can be neglected when modelling the field experiment, and 2) the hydraulic parameters suggested in the task definition is a good representation of the behaviour of the bentonite used in BRIE. These two conclusions are very valuable for the modelling presented in the rest of this report, which concerns the field experiment. Neglecting the initial gap means that we do not need to model mechanical processes; since solving a pure hydraulic problem is considerably easier than a coupled hydro-mechanical problem this is very important. Furthermore, since we can be confident in that the model of the bentonite is good we now know that the major uncertainty when modelling the field experiment will lie in the rock-material conceptualisation/parameterization.

Appendix C

Task 8a – Initial Scoping Calculation and sensitivity analysis

In task 8a, a single fracture intersects a deposition borehole (with a radius of 0.15 m) at mid height in a two-dimensional axisymmetric model. The influence of the fracture can be measured by the difference in buffer saturation as function of time at the height of the fracture and in at least one other point in the deposition borehole. Here we have chosen a point halfway in between the fracture and tunnel floor.

As part of the EBS TF, task 8a also included a sensitivity analyses used to determine how sensitive the model predictions are to uncertainties in parameter values in the constitutive relations used. The sensitivity analyses identified three key parameters in this context, which are further discussed below; the rock-matrix conductivity, K_R, the fracture transmissivity, T_F, and the bentonite's conductivity, K_B.

C.1 Objectives

From our perspective, the main purpose of task 8a is to understand which parameters are most important for the saturation process in our description of the rock and bentonite systems. Rather than evaluating this in a full 3D model, task 8a gives us the opportunity to better understand which material parameters are most important in terms of the saturation process using a simple 2D axisymmetric model.

C.2 Approach

The modelling was done using Code_Bright v3 and simulated only the hydraulic evolution in the rock and bentonite. A summary of the theory which Code_Bright is based on can be found in Appendix A. The model used is 2D-axisymmetric, and as such the tunnel (TASO) is not well represented. The geometry, and the mesh used, is shown in Figure C-1. In total, the mesh consisted of 1 209 quadrilateral elements, out of which 320 are placed in the buffer.

As part of this task, 22 models were done varying the properties of the surrounding rock and the bentonite buffer. The results are analysed by comparing the saturation evolution in two different points in the buffer.

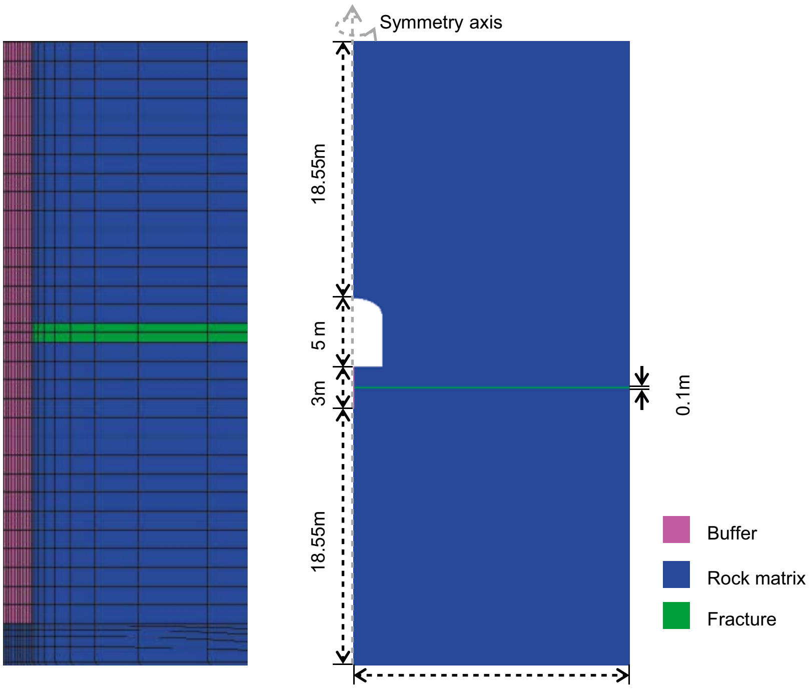

Figure C-1. *The left-hand panel shows a zoom-in at the buffer area, with the prescribed mesh. The right-hand panel shows the entire geometry with applied materials and dimensions.*

C.3 Model Setup

The model geometry, prescribed materials and the mesh in the area near the deposition borehole is shown in Figure C-1. The model includes three different materials; buffer, rock matrix and fracture.

The models are purely hydraulic and the liquid flux is modelled according to Darcy's law:

$$\boldsymbol{q}_\mathrm{l} = -\frac{kk_\mathrm{rl}}{\mu_\mathrm{l}}\nabla p_\mathrm{l} \;\; \text{m/s} \tag{C-1}$$

Here p_l, ρ_l and μ_l is the liquid pressure, density and viscosity respectively, while $\boldsymbol{k}$ and k_rl is the intrinsic and relative permeabilities. It should be noted that the effect of gravity is not included.

The liquid viscosity is defined as:

$$\mu_l = 2.1 \times 10^{-12} e^{1808.5/(273.15+T)} \tag{C-2}$$

Here T is the temperature (in °C) of the liquid. For our isothermal model with $T = 15$°C we have that $\mu_\mathrm{l} \approx 1.1 \times 10^{-9}$ MPa s.

The relative permeability is a function of the degree of liquid saturation, S_l, and is defined as:

$$k_{rl} = S_l^3 \qquad \text{(buffer)} \tag{C-3}$$

$$k_\mathrm{rl} = \sqrt{S_\mathrm{l}}\left[1 - \left(1 - S_\mathrm{l}^{1/\lambda}\right)^{\lambda}\right]^2 \qquad \text{(rock)}$$

Here λ is a fitting parameter and is defined in Table C-1. The liquid density is pressure dependent, and is defined as:

$$\rho_l = 1\,002.6 \times exp[4.5 \times 10^{-4} \times (p_l - 0.1)] \text{ kg m}^{-3} \tag{C-4}$$

Left to define is the retention capacity of the rock and buffer, as well as the materials' intrinsic permeabilities. Here we define these for the base case, and thereafter list how the parameters were varied in the sensitivity analyses.

C.3.1 Base case parameters

The retention properties of the buffer and rock are parameterized using van Genuchten's law:

$$S_\mathrm{l} = \left[1 + \left(\Psi/_{P_0}\right)^{\frac{1}{1-\lambda}}\right]^{-\lambda} \tag{C-5}$$

Here Ψ is the suction, while P_0 and λ are fitting parameters. Their values, as well as the intrinsic permeability's/fracture transmissivity in the base case are shown in Table C-1.

In one of the cases (#19) the extended form of van Genuchten's law is used:

$$S_\mathrm{l} = \left[1 + \left(\Psi/_{P_0}\right)^{\frac{1}{1-\lambda}}\right]^{-\lambda} \left[1 - \Psi/_{P_1}\right]^{\lambda_1} \tag{C-6}$$

Table C-1. Hydraulic parameters used in the base case.

Material	K [m/s]	T [m²/s]	P_0 [MPa]	λ [-]
Buffer	6.4×10^{-14}	-	9.23	0.3
Rock	1.0×10^{-12}	-	1.74	0.6
Fracture	-	5.0×10^{-10}	1.74	0.6

The initial conditions in the base case are:

Table C-2. Initial conditions prescribed in the base case (Void ratio, *e*; Porosity, *n*, and liquid pressure, P_l).

Material	*e/n* [-]	P_l [MPa]
Buffer	0.78/0.438	−99.9
Rock	$10^{-5}/10^{-5}$	2.0
Fracture	$10^{-3}/10^{-3}$	2.0

C.3.2 Sensitivity analyses

A sensitivity analysis was performed in order to determine the relative importance of different transport and retention parameters in terms of their effect on the saturation time of the bentonite. The parameters varied are specified in Table C-3.

In summary the cases can be divided into four different groups:

1) Case 1–16: Variation of the rock's hydraulic conductivity/the fracture's transmissivity.
2) Case 17–18: Variation of the bentonite's hydraulic conductivity.
3) Case 19–21: Variation of the retention capacity of all three materials.
4) Case 22: Variation of the rock's porosity.

The results from each of these different groups of models are discussed in detail in the next section.

Table C-3. Overview of parameter variation in the sensitivity analyses.

#	Transport parameters			Retention (P_0 [MPa], λ [-], P_1 [MPa], λ_1 [-])								
	K_R [m/s]	T_f [m²/s]	K_B [m/s]	$P_{0,R}$	λ_R	$P_{0,F}$	λ_F	$P_{0,B}$	λ_B	$P_{1,B}$	$\lambda_{1,B}$	n_R/n_F
1	1.0×10^{-12}	5×10^{-10}	6.4×10^{-14}	1.74	0.6	1.74	0.6	9.23	0.3	–	0	$10^{-5}/10^{-3}$
2	1.0×10^{-14}											
3	1.0×10^{-13}											
4	1.0×10^{-11}											
5	1.0×10^{-14}	1×10^{-12}										
6	1.0×10^{-13}	1×10^{-12}										
7		1×10^{-12}										
8	1.0×10^{-11}	1×10^{-12}										
9	1.0×10^{-14}	–										
10	1.0×10^{-13}	–										
11		–										
12	1.0×10^{-11}	–										
13	1.0×10^{-14}	1×10^{-8}										
14	1.0×10^{-13}	1×10^{-8}										
15		1×10^{-8}										
16	1.0×10^{-11}	1×10^{-8}										
17			3.8×10^{-14}									
18			1.3×10^{-13}									
19								6.258	0.21	400	1	
20						5.45×10^{3}	0.558					
21				80	0.45							
22												0.003/0.003

C.4 Results

C.4.1 Rock matrix conductivity

In the upper-left panel of Figure C-2 the saturation time evolution is shown for four different values of the rock-matrix conductivity: $K_R = 10^{-11}$, 10^{-12}, 10^{-13} and 10^{-14} m/s. The saturation is measured at two depths in the center of the deposition borehole: at the depth of the fracture (P_2, solid lines) and halfway in between the fracture and the tunnel floor (P_3, dashed lines).

The results show that the matrix conductivity is very important both in terms of the time until full saturation in the last point, as well as in terms of the ratio between the saturation time in points P_2 and P_3.

The ratio between the saturation time at P2 and P3 is a strong indicator of how important the fracture is for the hydration evolution in the bentonite. Hence, if for example $K_R = 10^{-11}$ m/s, this flow ratio through is close to one, meaning that the bentonite reach full saturation at all points at approximately the same point in time. Hence, for such high value of K_R the fracture has an insignificant effect on the saturation of the bentonite.

With decreasing values of the matrix conductivity, however, the fracture becomes successively more important. At very low values of K_R, it is reasonable to assume that almost all the water enters via the fracture, after which it is transported inside the bentonite. The magnitude of the latter flow is primarily set by the bentonite's conductivity.

C.4.2 Fracture transmissivity

As one part of the sensitivity analyses the fracture's transmissivity was varied by several orders of magnitude to determine the influence on 1) the total saturation time and 2) the variation in saturation time at different positions in the bentonite. The results are shown in the upper-right panel of Figure C-2 where it can be seen that changing the fracture transmissivity has a significant influence on the saturation time. However, the change in the total saturation time is significantly smaller here than what was seen when changing the conductivity of the rock matrix. Another important feature seen is that for transmissivities higher than 5×10^{-10} m^2/s no change in the saturation time at either point P_2 or P_3 can be seen. One can therefore deduce that for these transmissivities, the fracture provides more water to the bentonite than what can be absorbed per unit time. Hence, the fracture flow will be limited by the bentonite and thus in these cases the saturation time is set by the conductivity of the bentonite.

C.4.3 Bentonite conductivity

In the lower-left panel of Figure C-2 the saturation time-evolution is shown for varying bentonite conductivity. The conductivity of the rock matrix, as well as the transmissivity of the fracture, is kept constant between the three models. As expected, the hydraulic conductivity strongly influences the saturation time; in front of the fracture the change in saturation time is proportional to the change in conductivity. It should be noted that this behavior is seen because the relatively high rock-matrix conductivity/fracture transmissivity means that the bentonite has free access to water, and hence is the limiting factor with respect to how fast the saturation process goes. If the inflow to the bentonite was lower the bentonite properties would have less influence on the rate of saturation.

C.4.4 Retention capacity

The lower-right panel in Figure C-2 shows the effect of using different retention curves for all the different materials. As can be seen, the suggested variation of the bentonite and fracture materials' retention curves has no effect on the hydration evolution. The suggested alternative retention curve for the rock matrix does, however, have a small effect; it leads to a shorter saturation time in P_3.

C.4.5 Rock-matrix porosity

Finally, the model evaluating the effect which changing rock-matrix porosity has on the time until full saturation deserves mentioning. The results shows that the saturation time of the entire buffer, as well as the saturation time in the points P2 and P3, are unchanged when changing the rock matrix

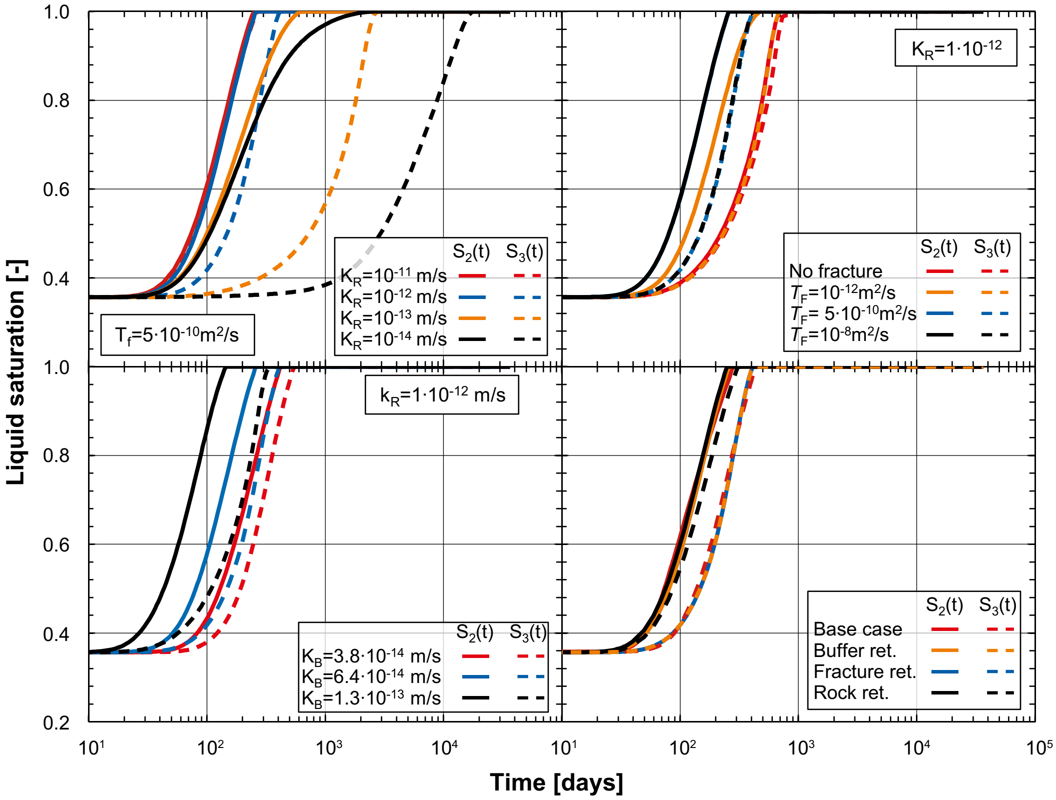

Figure C-2. *The time-evolution of liquid saturation is shown at the height of the fracture (P_2), and half in between the fracture and the tunnel floor (P_3), with varying rock matrix conductivity (upper-left panel), varying fracture transmissivity (upper right-panel), varying bentonite conductivity (lower-left panel) and varying retention parameters of both rock/fracture and bentonite (lower-right panel).*

porosity from 10^{-5} to 0.003. However, modelling the rock with a porosity of 10^{-5} led to severe numerical problems when using Code_Bright, which were not seen with the porosity set equal to 0.003. The latter value has thus been used in the modelling presented in the rest of this report.

C.5 Discussion

The sensitivity analyses presented here has shown that the matrix conductivity is the major component determining the saturation time given the model conceptualization of the experiment. However, it should be remembered that the geometry used is very simplified compared to the situation in the field, with a homogeneous and unfractured rock matrix on rather large scales. In reality, large fractures near the deposition boreholes could alter the situation, changing the effect that the matrix conductivity has on the hydration evolution in the bentonite.

The same is true for the fracture used. Intersections with other large fractures or deformation zones near the deposition boreholes could have an effect on the pressure profile in the fracture, and could, for example, potentially lead to less drying of the fracture (or vice versa) just after installation of the bentonite buffer. Furthermore, the fracture is here shaped as a disc around the deposition borehole. If the fracture only provides water over a small angular segment on the deposition borehole's wall, the area which is in contact with the bentonite decreases, which reduces the water inflow in the case of high flowing fractures.

As for the evaluation of the material properties of the bentonite it was shown that the hydraulic conductivity was important. It should, however, be remembered that the almost direct proportionality between the bentonite's conductivity and the saturation time is seen because both the rock-matrix conductivity ($K_R = 10^{-12}$ m/s) and the fracture transmissivity ($T_F = 5 \times 10^{-10}$ m/s^2) is set relatively high thus giving the bentonite almost free access to water. Using low values of the rock-matrix conductivity/fracture transmissivity would decrease the effect of the bentonite's conductivity on the saturation time.

C.6 Conclusions and recommendations

The modelling results show that the principal determinant for the saturation time is the magnitude of the flow entering through the rock matrix. However, in the case of very small matrix flow the fracture transmissivity and bentonite conductivity are the key ingredients in determining the saturation time.

Furthermore, the results quite clearly show that the retention parameters, within the range by which they were varied in this exercise, have small to none influence on the hydration of the bentonite. The same is true for the porosity of the rock material.

Thus, in terms of modelling the BRIE field experiment the sensitivity analyses has shown that great care must be taken when assigning a value on the hydraulic conductivity of the rock matrix, if an accurate prediction is to be made.

Appendix D

Task 8c – BRIE – Prediction for central deposition borehole

D.1 Objectives

The model implemented here includes a rather coarse treatment of the water transport properties of the host rock, and as such it cannot be used to predict inflows into the open probing/deposition boreholes. Thus, task 8c was not modelled following the strategy suggested in the task definition. Instead the field measurements available to us were used to calibrate 1) a model calibrated from the measured inflows to the small-scale probing borehole and 2) a model with the same rock-material calibration, with two full-size deposition boreholes (KO0017 and KO0018) with bentonite installed.

D.2 Approach

The models consider only hydraulic processes and were done using the FEM program Code_Bright_v3. Code_Bright can simulate flow in unsaturated media and is thus well suited at studying the hydration of the bentonite. It is, however, not practically possible to implement a fracture network in the rock material as Code_Bright does not allow for two-dimensional structures (i.e. plane fractures) in a three-dimensional geometry, as is used here.

The host rock, and in particular its water-transport properties, has therefore been conceptualized as homogeneous on the large scale and heterogeneous only very near the boreholes. This is implemented in the models by prescribing a homogeneous rock material (except for the two deterministic fractures which intersects TASD/O defined in the Task definition) with a rather high hydraulic conductivity everywhere except for in a cylinder with radius $r = 0.3$ m around the probing/deposition boreholes. The cylinders around the boreholes are assumed to have low hydraulic conductivities in order to represent the unfractured rock matrix. The fractures which are seen to intersect the deposition boreholes are represented as thin slices through the cylinder with a higher hydraulic conductivity. This approach allows us to reproduce both the liquid pressures around the TASO tunnel and boreholes as well as the measured inflows to the probing boreholes relatively well. It does, however, not allow us to predict the change in inflow due to expanding the probing boreholes into the larger deposition boreholes.

D.3 Model setup

Task 8c was divided into two main parts: 1) a full-scale, three-dimensional low-resolution model of the entire model domain[2], from which the results was used as boundary conditions for 2) a local, three-dimensional high-resolution model, only including one deposition borehole and the nearby host rock. This strategy allowed us to model the bentonite and near-field rock with the grid resolution needed to correctly resolve the inflows, without using excessive amount of CPU time. It also avoids severe convergence problems, which were common when simulating large-grid models using Code_Bright v3.

D.3.1 Large-scale model – implementation

As discussed above we treat the host rock as a homogeneous material everywhere except just around the boreholes (identified as **F**ractured **R**ock) with a conductivity that is significantly higher than that of the unfractured rock matrix ($K_{FR} = 10^{-9}$–10^{-10} m/s). These values are motivated by 1) the modelling of the prototype repository, in which the fractured-rock conductivity was calibrated from flow measurements into the tunnel, and 2) to achieve correct flows and heads into the BRIE boreholes.

In the proximity of the probing boreholes, the "average approximation" used for the fractured rock breaks down (see Figure D-1) and the inflows into these are primarily set by individual fractures as well as possibly via flow through the rock matrix. To account for this, each probing borehole is surrounded with a material identified as Deposition-hole rock (DHR), ($K_{DHR} = 10^{-14}$ m/s). In the probing boreholes where fractures have been found (KO0014 and KO0017), thin planes with higher conductivities are introduced at the fracture depths.

---

[2] The model domain as defined in the Task definition.

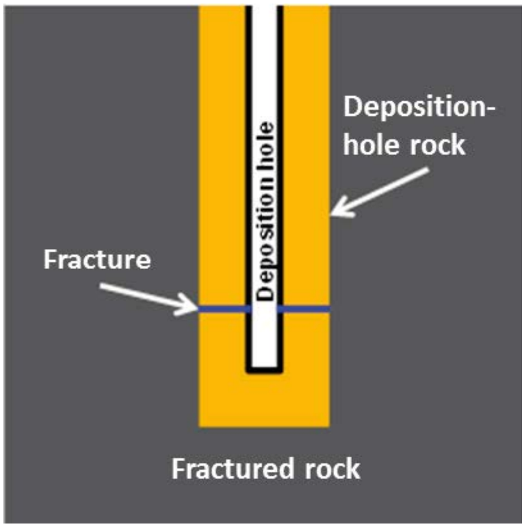

Figure D-1. *Schematic overview of the conceptual model used near the boreholes.*

The large-scale model is used to determine the boundary conditions and material parameters needed to match the measured inflows into the open probing boreholes, as well as the heads measured when the boreholes are packed off. The modelling parameters which are less well determined, and hence can be adjusted in this exercise are 1) the conductivity of the fractured rock, 2) the transmissivity of the fractures intersecting the rock matrix, and 3) the liquid pressure at the outer boundary of the model. In principle the thickness of the DHR material around the probing boreholes could also be adjusted, however, this involves significant changes to the geometry and mesh, and as it should have a similar effect as to changing the value of K_{DHR}, it has not been further explored here.

The liquid pressure at the outer boundary is prescribed in the task definition. However, there the pressure field varies over the boundary surfaces, a feature which is highly impractical to prescribe when using Code_Bright. Instead a constant pressure has been prescribed over the surfaces; the exact value is calibrated so as to match the measured heads in the boreholes, while still remaining within the limits of the values given in the task definition.

D.3.1.1 Geometry and material parameters

The geometry is taken from the task description (see Figure D-2 for an overview). The green cube, which identifies the large-scale model domain is 40 × 40 × 40 meters, and the model is meshed with tetrahedral elements, with a total of about 10^5 nodes. The constitutive laws and associated material parameters used are shown in Table D-1 – Table D-2.

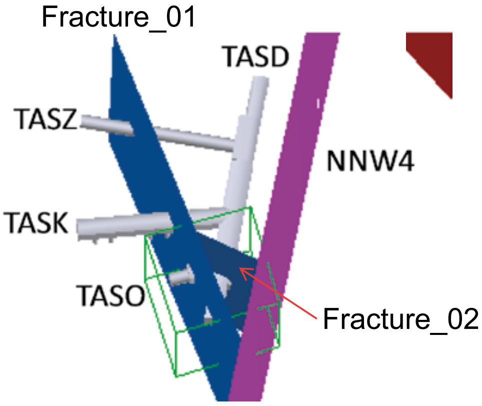

Figure D-2. *Schematic overview of the geometry used in the large-scale model.*

Table D-1. Hydraulic constitutive laws and parameters used for the buffer and nearby rock Task 8c.

		Parameter	Bentonite	DHR	Fractured rock
Liquid advective flux	$\boldsymbol{q}_l = -\frac{kk_{rl}}{\mu_l}(\nabla P_l - \rho \boldsymbol{g})$	k [m^2]	1.2×10^{-21}	1.0×10^{-21}	1.0×10^{-16}
		k_{rl} =	S^3	$\sqrt{S_l}\left(1-\left[1-S^{1/\lambda}\right]^{\lambda}\right)^2$	
Liquid density	$\rho_l = 997.5e^{[4.5 \times 10^{-4}(p_l - 0.1)]}$				
Liquid viscosity	$\mu_l = 1.051 \times 10^{-9}$ MPa s				
Retention curve	$S(\Psi) = \left[1 + \left(\frac{\Psi}{P_0}\right)^{1/1-\lambda}\right]^{-\lambda}$	P$_0$ [MPa]	9.23	0.6	
	$\Psi = p_g - p_l$	λ	0.30	0.24	

Table D-2. Hydraulic constitutive laws and parameters used for the large fractures (Task 8c).

		Parameter	Fracture_01	Fracture_02	NNW4
Liquid advective flux	$\boldsymbol{q}_l = -\frac{kk_{rl}}{\mu_l}(\nabla P_l - \rho \boldsymbol{g})$	T [m^2/s]	2.0×10^{-8}	2.0×10^{-9}	6.5×10^{-7}
	$K = \frac{T}{\text{Aperture}}, k = K\frac{\mu_l}{\rho \boldsymbol{g}}$	k_{rl} =	$\sqrt{S_l}\left(1-\left[1-S^{1/\lambda}\right]^{\lambda}\right)^2$		
Retention curve	$S(\Psi) = \left[1 + \left(\frac{\Psi}{P_0}\right)^{1/1-\lambda}\right]^{-\lambda}$	P$_0$ [MPa]	2.0×10^3	4.3×10^3	6.3×10^2
	$\Psi = p_g - p_l$	λ	0.558		

Table D-3. Hydraulic constitutive laws and parameters used for the borehole-intersecting fractures.

		Parameter	KO0014	KO0017
Liquid advective flux	$\boldsymbol{q}_l = -\frac{kk_{rl}}{\mu_l}(\nabla P_l - \rho \boldsymbol{g})$	T [m^2/s]	1.9×10^{-10}	3.0×10^{-11}
	$K = \frac{T}{\text{Aperture}}$	k_{rl} =	$\sqrt{S_l}\left(1-\left[1-S^{1/\lambda}\right]^{\lambda}\right)^2$	
Retention curve	$S(\Psi) = \left[1 + \left(\frac{\Psi}{P_0}\right)^{1/1-\lambda}\right]^{-\lambda}$	P$_0$ [MPa]	1.6×10^3	2.4×10^3
	$\Psi = p_g - p_l$	λ	0.558	

D.3.1.2 Initial and boundary conditions

The initial conditions in the model are the porosities and the initial liquid pressure. These are listed in Table D-4.

Table D-4. Initial conditions used when simulating Task 8D.

Parameter	Bentonite	Intact rock	Fractured rock	Fractures	
				Large-scale fractures	Borehole-intersecting fractures
Porosity	0.44	0.003	0.003	0.003	0.003
Liquid pressure [MPa]	−45.9	0.1	3.3	3.3	0.1

As for the prescribed boundary conditions, the outer boundaries are kept at a constant liquid pressure of 3.3 MPa at all times with the exception of the boundary which intercept TASD. This is given a no-flow condition at all times. The liquid pressure on the tunnel walls are kept equal to atmospheric pressure at all times. No inflow of water is allowed from the tunnels into the rock. The boreholes are initially assumed to be sealed off, a condition which is mimicked by prescribing a no-flow condition on the walls and bottom part. To measure the inflow into the probing boreholes, atmospheric pressure is prescribed on the walls and bottom parts on each of the five boreholes separately, for two days each.

D.3.2 Local-scale model – Implementation

When studying the flow field in the large-scale model, it can be seen that the flow in the fractured rock from the outer boundary towards the probing boreholes is mostly perpendicular to the tunnel floor. In order to facilitate a numerically less demanding model we can therefore to a good approximation cut out a thin vertical slice from the large-scale model as illustrated in Figure D-3. This geometry is still a 3D model, although the flows are mostly 2D, except just around the borehole (due to the curved shape of the latter).

D.3.2.1 Geometry and boundary conditions

The local model consists of a thin vertical slice out of the large-scale model; the geometry with mesh and materials is shown in Figure D-4. Its purpose is to study the wetting of the bentonite in test hole KO0017. The outer permeable material is needed to correctly match the pressure gradient from the large-scale model. The model is meshed with hexahedral elements, with a total of 41 000 nodes.

Six materials are included in the model. In general the materials have the same properties as in the large-scale model (see Table D-1 – Table D-3), although the permeability of the DHR material was varied a bit ($k = 5 \times 10^{-13} – 10^{-14}$ m^2). The two additional materials included in the local-scale model are the outer permeable material (see Figure D-3) and the bottom plate in the borehole (included in some simulations). The properties of these two materials are listed in Table D-5.

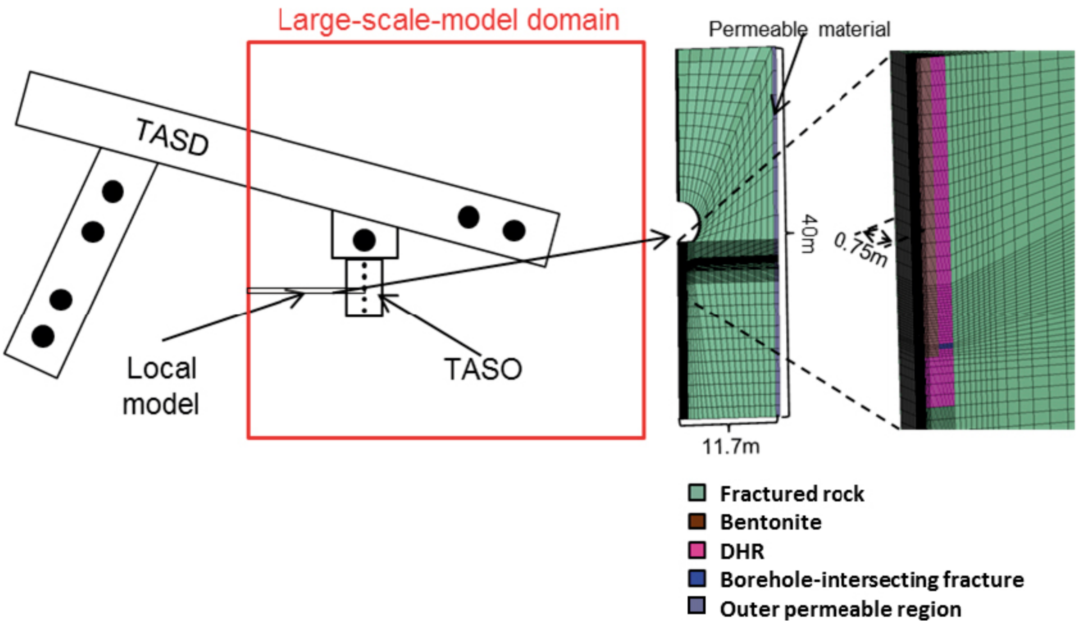

Figure D-3. *In the left panel the modelling domain defined in Task 8c is shown as the red square and the sub-domain used in the local-scale model is shown in grey. In the right part of the figure the meshed local-scale model and the materials used in its implementation is shown.*

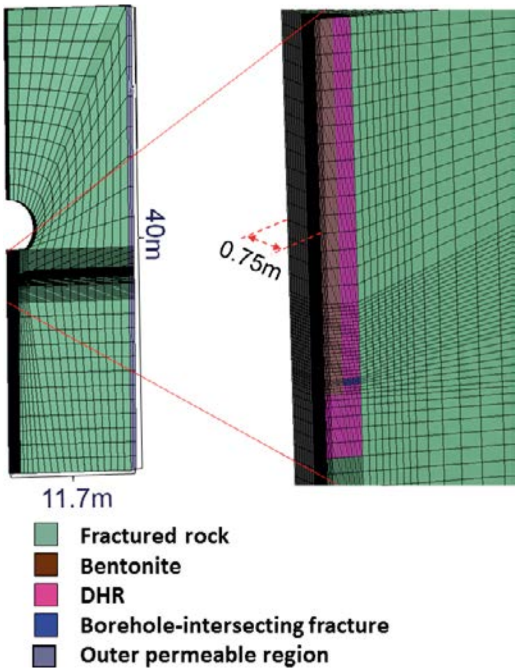

Figure D-4. *Overview of the geometry of the local model, with materials and mesh included.*

Table D-5. Hydraulic constitutive laws and parameters used for the additional local-scale materials.

		Parameter	Outer permeable material	Bottom plate
Liquid advective flux	$\boldsymbol{q}_l = -\frac{kk_{rl}}{\mu_l}(\nabla P_l - \rho \boldsymbol{g})$	k [m/s]	7.5×10^{-9}	10^{-23}
		k_{rl} =	$\sqrt{S_l}\left(1 - \left[1 - S^{1/\lambda}\right]^{\lambda}\right)^2$	
Retention curve	$S(\Psi) = \left[1 + \left(\frac{\Psi}{P_0}\right)^{1/_{1-\lambda}}\right]^{-\lambda}$	P_0 [MPa]	0.6	0.01
	$\Psi = p_g - p_l$	λ	0.24	0.3

D.3.2.2 Boundary and initial conditions

The liquid pressure on the outer horizontal boundaries is kept at 3.3 MPa at all times. The outer vertical boundary is a no-flow boundary. The installation of the bentonite is handled as follows: At first the bentonite material is set to be excavated in Code_Bright (the elements/nodes assigned to the buffer are inactive) while the liquid pressure on the walls of the test hole is kept at atmospheric pressure. The installation is handled by ramping down the liquid pressure on the walls of the test hole, after which the bentonite material is activated. After this, all pressure criteria except those on the outer wall, are removed, allowing the bentonite to take in water. The porosities of the materials are the same as in the large-scale geometry models (see Table D-4).

D.4 Results

The results of the large-scale and local-scale models are discussed separately in the two following sub sections.

D.4.1 Large-scale model

In Figure D-5 the pressure field near the packed-off boreholes is shown. The red lines outline where the highest inflows have been measured in the field experiment (i.e. the most likely location of water-bearing fractures). The head at these points are 3 bars in KO0014 and 10 bars in KO0017. These values agree well with those measured in the field.

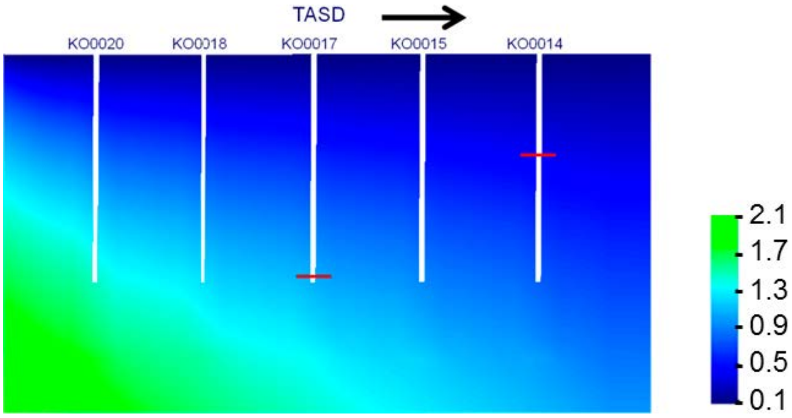

Figure D-5. *Liquid-pressure field around the packed-off boreholes in the large-scale model of the BRIE experiment done as part of task 8c. The red lines identify the most likely positions of the two most prominent water-bearing fractures detected in the field experiment.*

The fracture flow is determined by the head over the fracture and its transmissivity, T_f. In steady state the flow, Q, is given by:

$$Q = \frac{2\pi T_f \times h}{ln[r_o/r_i]} \text{ m}^3/\text{s}. \tag{D-1}$$

Here h is the head over the fracture, while r_o and r_i are the outer and inner radii respectively. Given the measured heads and inflows, the transmissivities of the two fractures should be:

Material	T_f
Frac KO0014	1.9×10^{-10} m^2/s
Frac KO0017	3.0×10^{-11} m^2/s

In Figure D-6 we show the inflows into the empty probing boreholes when using these transmissivities. In the model, the boreholes are successively opened to atmospheric pressure for two days. The inflows agree well with the measured values in the field, which are 1.0 ml/min in KO0014 and 0.5 ml/min in KO0017.

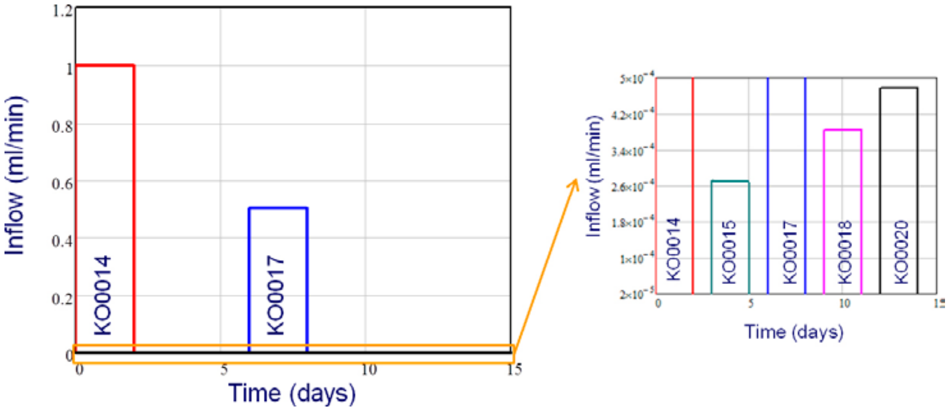

Figure D-6. *The measured inflows into the open probing boreholes. Each borehole is opened up to atmospheric conditions separately for two days each.*

The large-scale model can successfully reproduce the measured flows and heads in the boreholes, given single fractures at the observed depths in the boreholes, with calibrated transmissivities in the model. For the BRIE field experiment, boreholes KO0017 and 18 will be enlarged to a radius of 0.15 m and then filled with bentonite. It is not possible to accurately predict what the inflows into these deposition boreholes will be using our model. Too many unknowns exists, such as how the presently known fractures will react, as well as to whether new fractures will be intercepted by the larger deposition boreholes. As no measurements of the inflow into the deposition boreholes were available at the time of modelling, however, increasing the radius of the boreholes and taking the resulting inflow as a prediction was the only choice. It is important to remember that the radius of the rock matrix surrounding the hole is kept constant (at $r = 0.30$ m), causing its thickness to be reduced when increasing the radius of the probing bore hole. This in itself will cause a change in the flow through the fracture.

When increasing the radius to 0.15 m, we find an increase in the inflow into test hole KO0017, with $Q = 1.4$ ml/min. This value was used in the local model discussed below, as the best approximation we could make given our knowledge at that point in time.

D.4.2 Local-scale model

In Figure D-7 the saturation in the bentonite is shown both as contour plots at t = 0.5 and t = 1.0 years (left panel), and in a graph showing the vertical saturation profile in the center of the borehole at eight different times (right panel). Two sets of lines are included; results when a bottom plate is included (solid lines) and when no such plate is included (dashed lines). The conductivity of the deposition-hole rock material around the deposition borehole is $K_{\mathrm{DHR}} = 10^{-14}$ m/s, while the single fracture has a transmissivity of $T = 3.0 \times 10^{-11}$ m^2/s. Only close to the fracture (situated at a depth of 2.9 m) can a change in the degree of saturation be seen. After one year, however, the bentonite has not yet been fully saturated at any height. It is interesting to note that after day 200 the peak in saturation does not occur at the depth of the fracture. Instead, the bentonite at the bottom reaches the highest degree of saturation. The bottom plate has essentially no effect on the saturation profiles in this case.

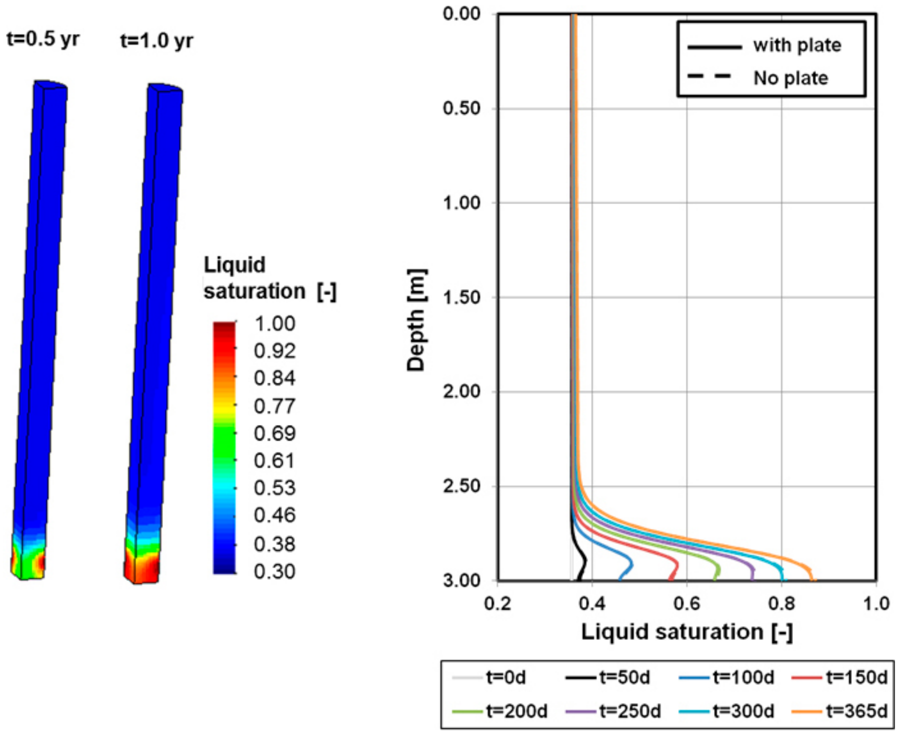

Figure D-7. Buffer saturation after 0.5 and 1.0 years respectively (left panel), as well as vertical saturation profiles (right panel) at eight different times. The conductivity in the low-permeable material surrounding the test hole was in this model set to 10^{-14} m/s. The fracture is located at a depth of 2.9 m.

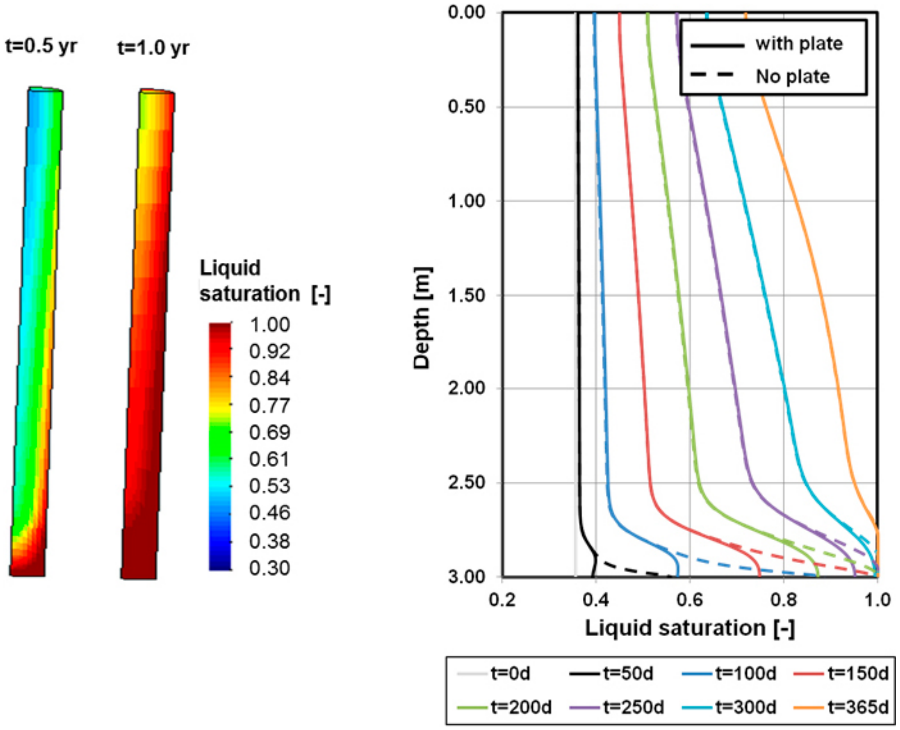

Figure D-8. *Buffer saturation after 0.5 and 1.0 years respectively (left panel), as well as vertical saturation profiles (right panel) at eight different times. The conductivity in the low-permeable material surrounding the test hole was in this model set to* 5×10^{-13} *m/s. The fracture is located at a depth of 2.9 m.*

In Figure D-8 the same model as above has been simulated, with the only change that the conductivity of the deposition-hole rock material is increased to $KDH_R = 5 \times 10^{-13}$ m/s. Such an increase does not significantly change the inflow into the empty boreholes, and hence the fracture transmissivity does not need to be changed. A radically different evolution after the installation of bentonite is, however, seen. First of all, the inclusion of the bottom plate now causes a significant reduction of the flow through the bottom. In models without the plate (dashed lines), the bentonite becomes fully saturated at the depth of the fracture within just 150 days. In models without the bottom plate the time until full saturation at the floor is reached increase by a factor of two, to 300 days.

The matrix inflow is in general significantly increased compared to the previous model. For example, just below the tunnel floor, which is the driest point in the model, the saturation reach as high as $S = 0.64$ on day 365. This can be compared to the model with $K_{DHR} = 10^{-14}$ m/s, where the saturation at the same point and time was equal to the initial value of $S = 0.36$.

D.5 Discussion

While the models done as part of Task 8c is in great need of better defined parameters, the results have shown that the task is numerically feasible. Calculations of the hydration phase of the bentonite shows a strong dependence on a few key model parameters, such as on the conductivity of the intact rock matrix near the test hole, as well as on the properties of fractures intersecting the borehole(s).

The modelling has also shown that the presence of fractures close to the bottom of the deposition borehole may complicate our understanding of the influence of fracture flow in this region, as the peak in saturation produced by the fracture may be hidden by inflow from the bottom. However, as shown in the models, the bottom plate that is included in the field experiment significantly reduces the influence of this effect. The modelling of Task 8c has shown that it should be possible to make relevant predictions of the evolution in the field using the implemented model conceptualization, however, not without significantly more detailed data from the characterization of the experimental site.

D.6 Conclusions and Recommendations

It is not possible to make a direct prediction on the evolution in the field from the results presented above, since the model conceptualization is too uncertain. However, some important conclusions can be drawn:

- The matrix conductivity near the probing borehole has a very high impact on the saturation evolution in the bentonite.
- Fractures close to the bottom (as is the case in KO0017) may be hard to distinguish from the flow through the bottom of the test hole if the matrix flow is significant. This effect can, as is seen in our models, be significantly reduced by using a bottom plate in the field experiment.

Appendix E

Task 8d – Prediction of inflow and wetting of KO0017G01 and KO0018G01 based on detailed characterization data

E.1 Objectives

The modelling described in this section was done using more extensive information from the characterization done at the site of the field experiment. For example, inflow mapping of the deposition-boreholes' walls were used, as well as updated geometrical information on the fractures intersecting the deposition boreholes.

Furthermore, a more detailed evaluation of the results could be done, as relative humidity (RH) and dismantling data was available at the time of writing this report.

The modelling was, however, done during the operation of the field experiment, and as such the results can be considered a semi-blind prediction (data from the RH-sensors were used to evaluate and improve the models) of the state at dismantling.

E.2 Approach

During the modelling of Task 8d Code_Bright version 4 was made available. This update included major improvements to the numerical stability of the code, which allowed us to abandon the hierarchical modelling strategy (with large-scale and local-scale models) and instead include the entire suggested model domain with a high grid resolution of the rock near the deposition borehole and the bentonite. During the course of the modelling several different calibrations of the transport properties of the rock near the deposition borehole was tested, here only the best ones (in terms of reproducing the RH data) are presented. The results considering deposition borehole KO0017 were presented at the joint EBS TF meeting in Lund in November 2012, while the model of KO0018 was done for and presented during the meeting of the BRIE steering group in Lund in September of 2013.

E.3 Model setup

At the time of modelling the characterization data available to us were:

1) Open deposition borehole inflow mapping based on nappy measurements in KO0017.
2) Open deposition borehole inflow into the lower part of KO0018.
3) The fracture at a depth of 2.6 m in KO0018 mostly provides water in the upper part.
4) Three fractures (two in KO0017 and one in KO0018) dominate the fracture inflow.
5) Detailed information on the position of the deposition boreholes and their depth.

The geometry used in the models was constructed with these points in mind; Figure E-1 shows the entire geometry and Figure E-2 shows the implemented geometry near the deposition boreholes.

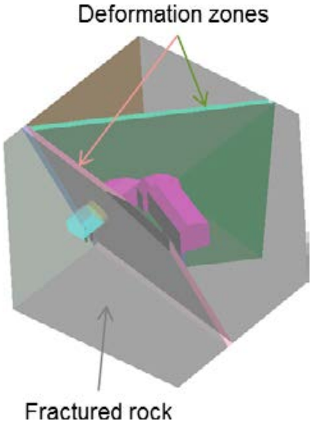

Figure E-1. Entire model domain used when simulating Task 8D.

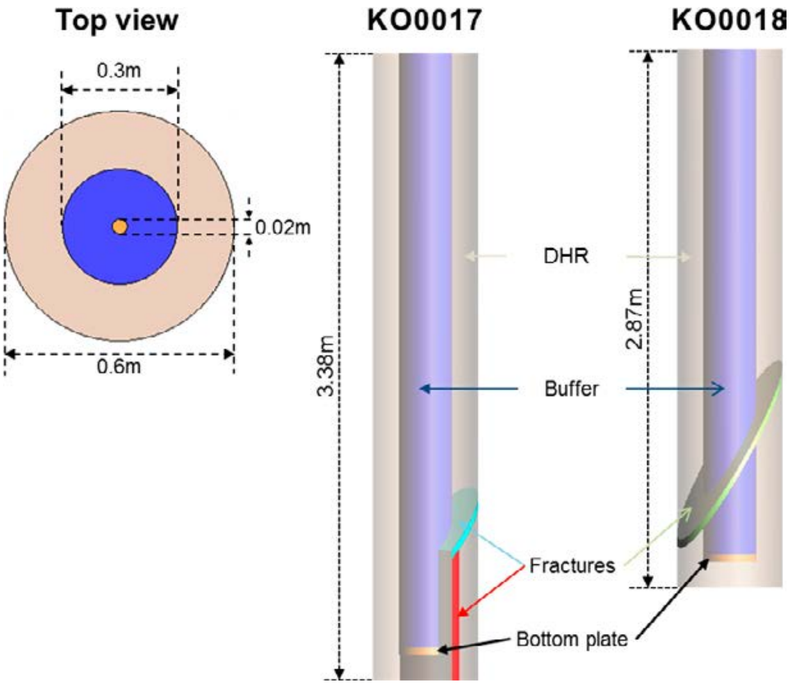

Figure E-2. *The geometry and materials used to describe the deposition boreholes and nearby rock when modelling Task 8d.*

The constitutive laws and material parameters used are summarized in Table E-1 – Table E-2 and the initial conditions in Table E-3. The material parameters for the two large deformation zones are not included here; they are identical to the parameters defined in the task definition.

To allow for a sufficiently high numerical accuracy, two models were constructed with increased resolution for deposition borehole KO0017 in one and increased resolution for deposition borehole KO0018 in the other one.

Table E-1. Hydraulic constitutive laws and parameters.

		Parameter	Bentonite	DHR	Fractured rock
Liquid advective flux	$\boldsymbol{q}_l = -\frac{kk_{rl}}{\mu_l}(\nabla P_l - \rho \boldsymbol{g})$	k [m^2]	1.2×10^{-21}	1.0×10^{-21}	1.0×10^{-17}
		k_{rl} =	S^3	$\sqrt{S_l}\left(1 - \left[1 - S^{1/\lambda}\right]^{\lambda}\right)^2$	
Liquid density	$\rho_l = 997.5e^{[4.5 \times 10^{-4}(p_l - 0.1)]}$				
Liquid viscosity	$\mu_l = 1.051 \times 10^{-9}$ MPa s				
Retention curve	$S(\Psi) = \left[1 + \left(\frac{\Psi}{P_0}\right)^{1/_{1-\lambda}}\right]^{-\lambda}$	P$_0$ [MPa]	9.23	0.6	
	$\Psi = p_g - p_l$	λ	0.30	0.24	

Table E-2. Hydraulic constitutive laws and parameters.

		Parameter	KO0017		KO0018
			Fracture @ 2.6 m	Bottom fracture	Fracture @ 2.3 m
Liquid advective flux	$\boldsymbol{q}_l = -\frac{kk_{rl}}{\mu_l}(\nabla P_l - \rho \boldsymbol{g})$	k [m^2]	7.62×10^{-18}	7.77×10^{-18}	8.55×10^{-19}
		k_{rl} =	$\sqrt{S_l}\left(1 - \left[1 - S^{1/\lambda}\right]^{\lambda}\right)^2$		
Liquid density	$\rho_l = 997.5e^{[4.5 \times 10^{-4}(p_l - 0.1)]}$				
Liquid viscosity	$\mu_l = 1.051 \times 10^{-9}$ MPa s				
Retention curve	$S(\Psi) = \left[1 + \left(\frac{\Psi}{P_0}\right)^{1/_{1-\lambda}}\right]^{-\lambda}$	P_0 [MPa]	2440		
	$\Psi = p_g - p_l$	λ	0.558		

Table E-3. Initial conditions used when simulating Task 8D.

Parameter	Bentonite	Intact rock	Fractured rock	KO0017		KO0018
				Fracture @ 2.6 m	Bottom fracture	Fracture @ 2.3 m
Porosity	0.44	0.003	0.003	0.003	0.003	0.003
Liquid pressure [MPa]	–69.9	0.1	3.3	0.1	0.1	0.1

E.4 Results

Here only the results considering the calibration of rock properties are discussed; the results from the models of the hydraulic evolution in the bentonite is discussed in Section 3.2.

The measured pressures in several probing boreholes surrounding the deposition boreholes are shown in the left panel of Figure E-3, and a snapshot from the models of the same region is shown in the right panel. The agreement is rather good from the tunnel entrance (left side in Figure E-3) up to the position of borehole 18. However, further down the tunnel the model predicts higher water pressures than what is seen in the field. Although the match is far from perfect the agreement must still be considered good due to the homogeneous structure of the rock in the models, as compared to the very heterogeneous structure in the field.

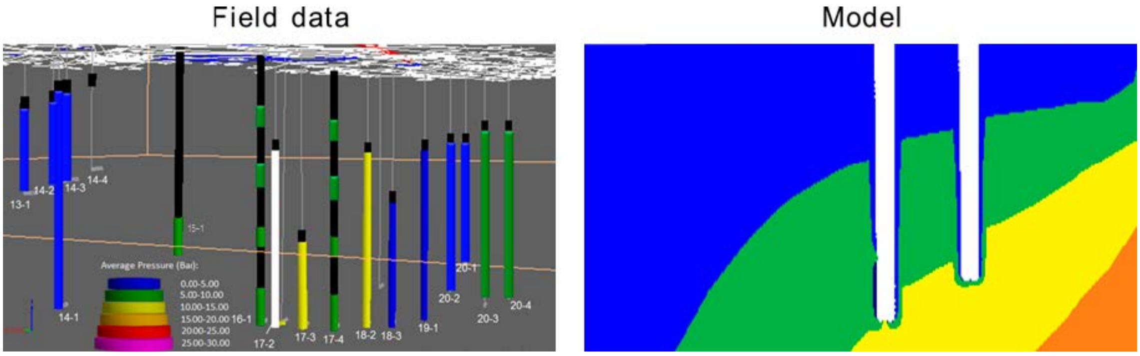

Figure E-3. The left panel shows the average water pressures in the field as measured during the time frame three to six months after installation of the bentonite. The measured pressures were taken from the "Task 8 additional information package". In the right panel the water pressure from the same time period and position in the model is shown.

In Table E-4 the measured and modelled inflows are compared. As can be seen, they agree well with each other. The total inflow in the models is identical to the total measured inflow, although the distribution with depth in KO0017 shows some small discrepancies.

Table E-4. Measured and modelled inflows into the two deposition boreholes.

	Depth [m]	Q_{model} [ml/min]	$Q_{measured}$ [ml/min]
KO0017	2.10–3.50	0.200	0.20
	2.25–2.95	0.050	0.05
	2.95–3.25	0.056	0.05
	3.25–3.45	0.042	0.05
	3.45–3.50	0.052	0.05
KO0018	2.10–3.10	0.01–0.03	0.01–0.03

Appendix F

Local-scale models of BRIE

F.1 Objectives

The local-scale models of BRIE were constructed to investigate the effect of small-scale geometrical changes on the hydraulic evolution, such as additional borehole-intersecting fractures and an open column around the bottom plate. The benefits of doing this using a local-scale geometry is that it allows for a much faster implementation of the changes to the geometry, and allows for using irregular meshes without causing too much added numerical complexity (a requirement when implementing more fractures using Code_Bright).

F.2 Model Setup

Only borehole 18 was modelled using a local-scale geometry, and as such the dimensions of this borehole was used to create the geometry.

F.2.1 Geometry and material properties

The geometry is shown in Figure F-1. The left-panel shows the entire geometry, which was used in all models, while the right panel shows the geometry of the bottom plate.

An outer column with a radial thickness of 10 mm was implemented, in one model this column was given a high permeability and porosity to simulate the effect of an open column around the bottom plate, while in the other models the properties of the column was set identical to that of the bottom plate (hence no spacing between the plate and rock wall was assumed).

The material properties are essentially the same as in Task 8D, but are included in Table F-1 for convenience, the constitutive laws used are, however, not repeated.

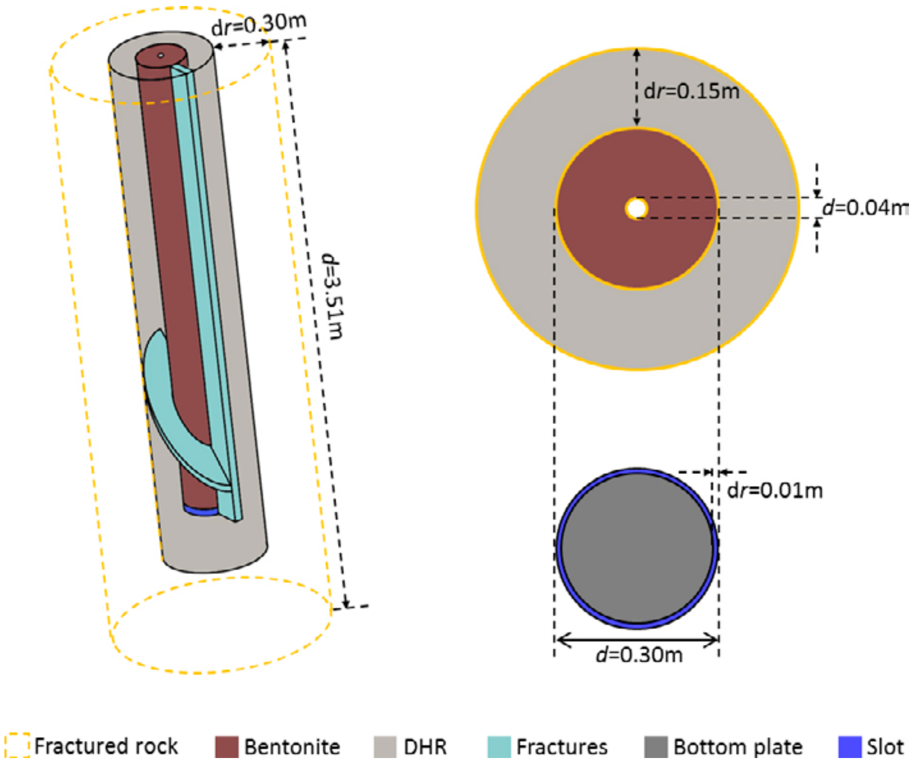

Figure F-1. *Local-scale model geometry.*

Table F-1. Hydraulic constitutive laws and parameters.

	Parameter	Bentonite	Bottom plate[2]	DHR	Fractured rock	DH fractures Horizontal	 Vertical[3]
Liquid advective flux	k [m^2]	6.4×10^{-21}	10^{-29} 10^{-17}	10^{-21}	1.0×10^{-17}	4.8×10^{-19}	1.95×10^{-19} 4.8×10^{-19}
	k_{rl} =	S^3		$\sqrt{S_l}\left(1-\left[1-S^{1/\lambda}\right]^{\lambda}\right)^2$			
Retention curve	P_0 [MPa] λ	9.23[1] 0.30[1]	0.1 0.3	0.6 0.24		2440 0.558	

[1] In one model a slightly different parameter set was used with P0 = 9.43 MPa, and λ = 0.32.

[3] The high permeability value was used in the open slot around the bottom plate in one model.

[3] The high permeability value was used in the model analyzing the open slot around the bottom plate.

Table F-2. Initial conditions.

Parameter	Bentonite	Bottom plate Plate	 Slot	Rock
Porosity	0.44	0.001	0.9	0.003
Liquid pressure [MPa]	−69.9	−69.9	0.1	3.3

Appendix G

Comsol models

G.1 Objectives

The objective of the models simulated using Comsol Multiphysics was to investigate the effect of an alternate relative permeability law in the DHR material (and hence in the rock matrix). Comsol Multiphysics was used so as to allow for the implementation of this law. The liquid flow was handled using the same formulation as in Code_Bright. The theoretical and experimental foundation behind the chosen relative permeability law is given in Appendix H.

G.2 Model Setup

The model is a very simplified version of borehole 17, but in many ways based on the local-scale models discussed in Appendix F.

G.2.1 Geometry and material properties

The geometry is a 2D axisymmetric representation of the local-scale geometry, but here with dimensions based on borehole 17 (some simplifications were, however, made).

The material parameters used are given in Table G-1 and Table G-2.

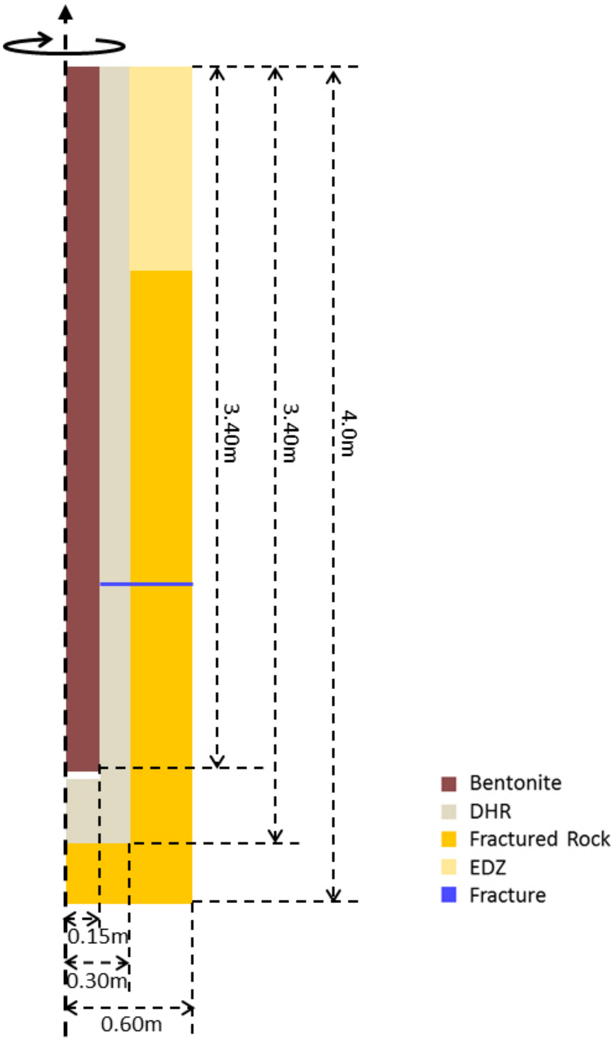

***Figure G-1.** Geometry used in the 2D axisymmetric models simulated in Comsol Multiphysics.*

Table G-1. Hydraulic constitutive laws and parameters.

		Parameter	Bentonite	Fractured rock	EDZ	Fracture
Liquid advective flux	$\boldsymbol{q}_l = -\frac{k k_{rl}}{\mu_l}(\nabla P_l - \rho \boldsymbol{g})$	k [m^2]	1.2×10^{-21}	10^{-17}	10^{-13}	7.62×10^{-18}
		k_{rl} =	S^3	1		
Liquid density	$\rho_l = 1\,000$ kg/m^3					
Liquid viscosity	$\mu_l = 10^{-9}$ MPa					
Retention curve	$S(\Psi) = \left[1 + \left(\frac{\Psi}{P_0}\right)^{1/(1-\lambda)}\right]^{-\lambda}$	P_0 [MPa]	9.23	0.6		
	$\Psi = p_g - p_l$	λ	0.30	0.24		

Table G-2. Hydraulic constitutive laws and parameters.

	Parameter	DHR vG	Adopted_kr[1]
Liquid advective flux	k [m^2] k_{rl} =	10^{-21} $\sqrt{S_l}\left(1 - \left[1 - S^{1/\lambda}\right]^{\lambda}\right)^2$	2×10^{-20} $\begin{cases} 5 \cdot 10^{-4} S_l^2 & S_l < 0.999 \\ f_{step}(S_l) & 0.999 < S_l < 1.0 \\ 1 & S_l \geq 1.0 \end{cases}$
Retention curve	P_0 [MPa] λ	0.6 0.24	

[1] Here $f_{step}(S_l)$ is a step function (Comsol built-in function) which defines a continuous function (with continuous first and second derivatives) between $5 \times 10^{-4} \times 0.99^2$ and 1.

G.2.2 Initial and boundary conditions

The initial conditions used are given in Table G-3.

Table G-3. Initial conditions used when simulating Task 8D.

Parameter	Bentonite	Rock
Porosity	0.44	0.003
Liquid pressure [MPa]	−69.9	0.1

The only boundary conditions prescribed are the liquid pressures on the top and bottom of the fractured rock cylinders: atmospheric pressure on the top and 12.6 bars liquid pressure on the bottom.

Appendix H

Evaluation of a relative permeability relation from vapor permeability data

H.1 Background

The relative permeability relation provided to be used for the rock material in Task 8 follows the van Genuchten type formulation, and this was originally motivated by measurements at the Grimsel Test Site. No evaluation of this property have to the authors knowledge been performed on rock material from the Äspö laboratory or any other granitic rock in Sweden. During the course of the Task 8 it was however noticed that measurements of *vapor permeability* performed on granite samples (from the west coast of Sweden) had been reported in the building material engineering literature (Hedenblad 1996). These measurements were performed by putting a sample on top of a cup with a saturated salt solution with a specific RH (Figure H-1, left). The cup and the sample was then placed in a climate chamber with a fixed RH (usually 35 %), which means that a gradient in vapor content was maintained over the sample. And by measuring how much water that was lost from the salt solution during a certain time period a flow coefficient could be evaluated. By repeating this procedure for 8 different salt solutions, a relation between the vapor permeability and the RH could be evaluated (Figure H-1, right). This memo presents a procedure to convert this relation to a relative permeability relation.

H.2 Conversion of vapor permeability data into relative permeability

The following evaluation is based on the notion that the moisture flux ($\bar{g}$) is proportional to the gradient of any moisture state variable (ϕ), and that the flow coefficient for this depends on the moisture state: $\bar{g}=-D_{\phi}(\phi)\cdot\nabla\phi$. This means that we can always (under isothermal conditions) evaluate a flow coefficient for another moisture state variable (ϕ') from the relation $D_{\phi'}(\phi')=\frac{d\phi}{d\phi'}\cdot D_{\phi}(\phi)$ (Arfvidsson and Claesson 2000). In our case, the flow coefficient for a gradient of vapour content is converted to a corresponding coefficient for a gradient in water pressure. This approach is not based on any assumptions about the physical processes on the pore level, but is simply a consequence of the Fickian description of the moisture flow.

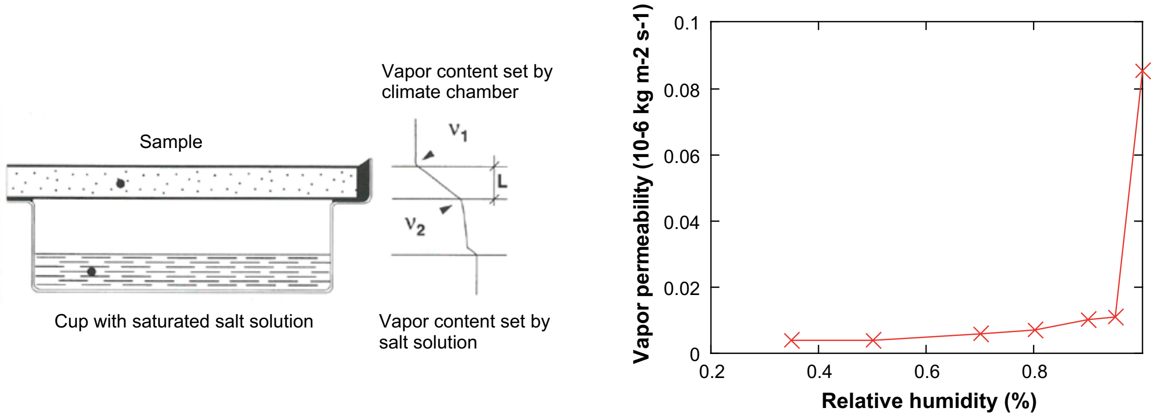

Figure H-1. *Schematic test setup for vapor permeability measurements (left), and experimental data for granite (Bohus, röd Bratteby) presented by Hedenblad (1996).*

The vapor permeability (δ_v, $m^2 \cdot s^{-1}$) is defined as:

$$g = -\delta_v \cdot \frac{\partial \nu}{\partial x} \qquad \text{(H-1)}$$

where g is the vapor flux ($kg \cdot m^{-2} \cdot s^{-1}$), ν is the vapor content ($kg \cdot m^{-3}$) and x is a coordinate (m).

A corresponding mass flux is defined by Darcy's equation as:

$$g = -\frac{\rho_w \cdot k \cdot k_r}{\mu} \cdot \frac{\partial P}{\partial x} \qquad \text{(H-2)}$$

where ρ_w is the density of water ($kg \cdot m^{-3}$), k is the intrinsic permeability (m^2), k_r is the relative permeability (-), P is the water pressure (Pa), and μ is the water viscosity ($Pa \cdot s$). It should be noted that $P < 0$ for unsaturated conditions.

By equation Equations (H-1) and (H-2) we get:

$$\delta_v \cdot \frac{\partial \nu}{\partial x} = \frac{\rho_w \cdot k \cdot k_r}{\mu} \cdot \frac{\partial P}{\partial x} \qquad \text{(H-3)}$$

And from this we can identify a relation between the relative permeability and the vapor permeability which includes the derivative of the vapor content with respect to the water pressure:

$$k_r = \frac{\delta_v \cdot \frac{d\nu}{dP} \cdot \mu}{\rho_w \cdot k} \qquad \text{(H-4)}$$

In order to evaluate this as a function of the saturation degree (S), we introduces a water retention curve which follows the van Genuchten type. Both the original form, and the inverse function are considered:

$$S(P) = \left(1 + \left(\frac{p_g - P}{P_0}\right)^{\frac{1}{1-\lambda}}\right)^{-\lambda} \leftrightarrow P(S) = p_g - P_0 \cdot \left(S^{-\frac{1}{\lambda}} - 1\right)^{1-\lambda} \qquad \text{(H-5)}$$

where p_g is the gas pressure (Pa); and P_0 (Pa) and λ (-) are parameters:

In addition, the Kelvin's law is introduced which gives a relation between the relative humidity (RH,-) and the water pressure:

$$RH(P) = \exp\left(\frac{-(p_g - P) \cdot M_w}{RT \cdot \rho_w}\right) \qquad \text{(H-6)}$$

where T is the temperature (K), R is the universal gas constant ($J \cdot mol^{-1} \cdot K^{-1}$) and M_w is the molecular weight of water ($kg \cdot mol^{-1}$).

From this a relation between the vapor content and water pressure can be defined:

$$\nu(P) = \nu_{sat} \cdot RH(P) \qquad \text{(H-7)}$$

where ν_{sat} is the saturated vapor content.

From Equation (H-6) and (H-7) we can calculate the sought derivative:

$$\frac{d\nu}{dP} = \frac{M_w \cdot \nu}{RT \cdot \rho_w} \qquad \text{(H-8)}$$

Together with Equation (H-4) we can define the relative permeability as function of saturation degree:

$$k_r(S) = \frac{\delta_v(S) \cdot \nu(S)}{k} \frac{M_w \cdot \mu}{RT \cdot \rho_w^2} \qquad \text{(H-9)}$$

It can be noted that the saturation dependence of both the vapor permeability and the vapor content presupposes a water retention curve RH(S), which therefore has to be specified. In addition, an intrinsic permeability has to be specified.

It should be noted that the evaluated k_{rel} relation (H-9) doesn't necessarily reach the value of 1 when $S \rightarrow 1$. This is due to the fact that the measured vapor permeability at high vapor contents doesn't correspond to the specified intrinsic permeability value. This therefore leads to a discontinuity close to saturation.

H.3 Application to Task 8 conditions

The relative permeability function was quantified for a case which was based on the vapor permeability data for granite, as provided by Hedenblad (1996), as well as for the intrinsic permeability and water retention curve, as provided in Task 8.

The following parameters were specific for Task 8: $k=2\cdot 10^{-20}$ m², $P_0=0.6$ MPa, and $\lambda=0.24$, while the following values are general (at 20 °C): $T=293$ K; $\nu_{sat}=0.017$ $kg\cdot m^{-3}$; $\mu=0.001$ Pa·s; $R=8.314$ $J\cdot mol^{-1}\cdot K^{-1}$; $M_w=0.018$ $kg\cdot mol^{-1}$; and $\rho_w=1\,000$ $kg\cdot m^{-3}$.

The evaluated function is shown in Figure H-2 (red line). It can be noted that it is generally lower than 10^{-3} and that is displays a discontinuous step at saturation. In order to have a more applicable expression a function of the following for was adopted (see black line in Figure H-2):

$$k_r(S) = \begin{cases} 5\cdot 10^{-4}\cdot S^2 & S<1 \\ 1 & S=1 \end{cases} \tag{H-10}$$

This can be compared with the relation provided to be used for the rock material in Task 8 (see blue line in Figure H-2):

$$k_r(S) = \sqrt{S}\cdot\left[1-\left(1-S^{\frac{1}{\lambda}}\right)^{\lambda}\right]^2 \tag{H-11}$$

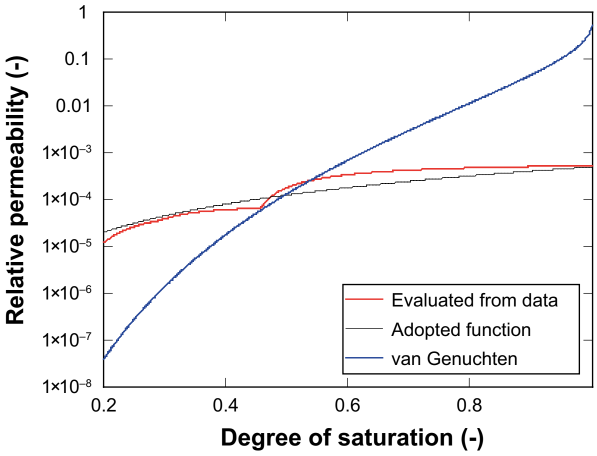

Figure H-2. *Relative permeability relations. As evaluated with from data with Equation H-9 (red line), adopted on the form in Equation H-10 (black line), and the one provided with Task 8 (blue line).*

Appendix I

Scale-dependence of an equivalent hydraulic conductivity, and a tentative motivation for a simple porous media representation of fractured rock

I.1 Background

Models of the hydration of the BRIE experiment (i.e. Task 8) show that the fractured rock around the bentonite parcels can be successfully represented with basically two zones: one close to the bentonite with a low permeability media (denoted the matrix) intersected by permeable narrow paths or discs; and one beyond a limited distance, with a homogenous porous media with a fairly high hydraulic conductivity. With this simple approach, the matrix conductivity should be consistent with results from laboratory measurements, the effective transmissivity of paths and discs should correspond to actual fracture transmissivities close to the bentonite, and the high hydraulic conductivity of the second zone should reflect the averaged effective conductivity of the fractured rock. To the author's knowledge however, no attempt has been made: i) to motivate a specific thickness of the intersected low permeability zone; and ii) to derive a simple relation between the fracture statistics (as in the Task 8 definition) and an equivalent hydraulic conductivity. This memo presents an attempt to address these issues.

I.2 Fracture distribution and transmissivity relations

This analysis is essentially based on two relations describing the fracture network: the size distribution of the fracture intensity, and a relation between size and transmissivity. The intensity of fractures is here described with the P_{32} quantity, which denotes the fracture area per unit volume and therefore has the unit m^{-1}. The size distribution of fracture intensity is described by Vidstrand et al. (2017) with the following power law relation:

$$P_{32,r_a-r_b} = P_{32,r_1-r_2} \cdot \frac{r_a^{2-k_r} - r_b^{2-k_r}}{r_1^{2-k_r} - r_2^{2-k_r}} \tag{I-1}$$

This denotes the intensity of fractures within the radii interval $r_a \rightarrow r_b$. The corresponding intensity for the interval $r_1 \rightarrow r_2$ is specified as a constant ($P_{32,r1-r2}$), and the decreasing frequency with radius is described with the parameter k_r. For simplicity, this is reformulated by equating both r_a and r_1 with a constant lower radius limit r_0; by equating r_2 with infinity, and by renaming r_b and $P_{32,r1-r2}$ with the notation r and P_{32}^{TOT}, respectively:

$$P_{32}(r) = \frac{P_{32}^{TOT}}{r_0^{2-k_r}} \cdot (r_0^{2-k_r} - r^{2-k_r}) \tag{I-2}$$

The intensity is thus only dependent on one variable. The derivative of this function is denoted $p_{32}(r)$ and can be calculated as:

$$p_{32}(r) = \frac{dP_{32}}{dr} = -(2-k_r) \cdot \frac{P_{32}^{TOT}}{r_0^{2-k_r}} \cdot r^{1-k_r} \tag{I-3}$$

The relation between the fracture radius (r) and the transmissivity (T) is described with the following relation:

$$T(r) = T_{ref} \cdot \left(\frac{r}{r_{ref}} \right)^{\lambda} \tag{I-4}$$

where T_{ref} and r_{ref} are reference values, and λ a parameter.

I.3 Derivation of equivalent hydraulic conductivity and dimension

In this section the intensity quantity P_{10} is considered and this denotes the number of fractures per unit length and has the unit m^{-1}. A fracture set is considered to be composed of fractures which are grouped in intervals with n defining radii, denoted r_i with index i ranging from 0 to $n-1$. The intensity of fractures in an interval with two successive radii $P_{10}(r_i,r_{i+1})$ is for simplicity denoted $\Delta P_{10,i}$. The total intensity can in this way be described with the following sums of intensities:

$$P_{10}^{TOT} = \sum_{i=0}^{n-1} P_{10}(r_i, r_{i+1}) = \sum_{i=0}^{n-1} \Delta P_{10,i} \tag{I-5}$$

The transmissivity for the fractures in an interval with two successive radii can be estimated as the average of the transmissivity of the bounding radii:

$$T_i \approx \frac{T(r_i)+T(r_{i+1})}{2} \tag{I-6}$$

It should be noted that the accuracy of this estimate increases with increasing number of intervals. With this notation a specific fracture radius (i = j) is considered. The equivalent conductivity of all fractures with radii smaller than the radius r_j can be calculated as the following sum (see Figure I-1):

$$K_j = \sum_{i=1}^{j-1} T_i \cdot \Delta P_{10,i} \tag{I-7}$$

The characteristic distance between fractures with radii larger than the radius r_j can be calculated as the inverse of the intensity of all fractures exceeding that radius (see Figure I-1):

$$L_j = \frac{1}{\sum_{i=j}^{n-1} \Delta P_{10,i}} = \frac{1}{P_{10}^{TOT} - \sum_{i=0}^{j-1} \Delta P_{10,i}} \tag{I-8}$$

By increasing the number of intervals to infinity, the equivalent conductivity can be expressed with the following integral:

$$K(r) = \int_{r_0}^{r} T(\rho) \cdot \frac{dP_{10}}{d\rho} \cdot d\rho = \int_{r_0}^{r} T(\rho) \cdot p_{10}(\rho) \cdot d\rho \tag{I-9}$$

The intensity interval (ΔP_{10}) is here expressed with the derivative of the intensity (i.e. $dP_{10}/dr \cdot \Delta r$). Correspondingly, the characteristic distance is expressed in terms of the intensity for all fractures with radii smaller than r:

$$L(r) = \frac{1}{P_{10}^{TOT} - P_{10}(r)} \tag{I-10}$$

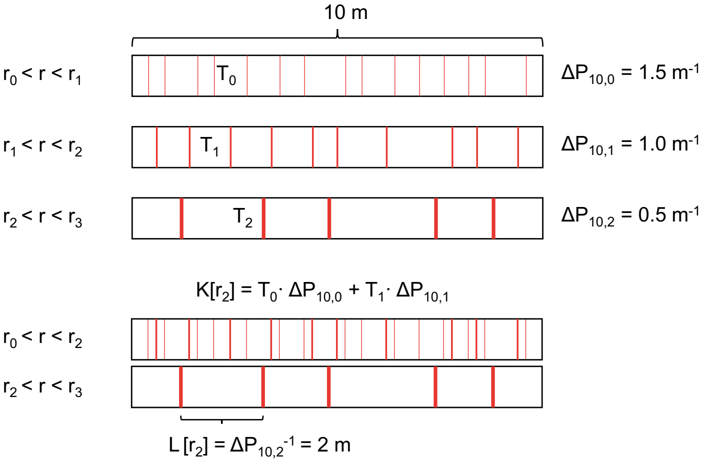

Figure I-1. *Fracture set with three intervals and four defining radii (n = 4), with intensities given for the number of illustrated fractures and the given length (upper graph). Equivalent conductivity for the two lower intervals (j = 2) and the inverse intensity and characteristic distance for fractures with radii larger than r2 (lower graph).*

I.4 Scale dependence of the equivalent hydraulic conductivity

The derived relations for the equivalent conductivity and the characteristic distance is here assumed to be valid for the P_{32} intensity as well as for P_{10}. This means that Equations (I-9), (I-3) and (I-4) can be combined in the following way:

$$K(r) = \int_{r_0}^{r} T(\rho)\cdot p_{32}(\rho)\cdot d\rho = \frac{2-k_r}{\lambda+2-k_r}\cdot\frac{P_{32}^{TOT}}{r_0^{2-k_r}}\cdot\frac{T_{ref}}{r_{ref}^{\lambda}}\cdot\left(r_0^{\lambda+2-k_r} - r^{\lambda+2-k_r}\right) \qquad \text{(I-11)}$$

Correspondingly, Equations (I-10) and (I-2) can be combined as:

$$L(r) = \frac{1}{P_{32}^{TOT} - P_{32}(r)} = \frac{1}{P_{32}^{TOT}}\frac{r_0^{2-k_r}}{r^{2-k_r}} \qquad \text{(I-12)}$$

From this relation, the radius r is expressed in terms of L:

$$r = \frac{r_0}{\left(P_{32}^{TOT}\cdot L\right)^{\frac{1}{2-k_r}}} \qquad \text{(I-13)}$$

Moreover, a new parameter can be defined in terms of k_r and λ:

$$\alpha = -\frac{\lambda+2-k_r}{2-k_r} \qquad \text{(I-14)}$$

Finally, a constant conductivity value is defined as:

$$K_c = \frac{P_{32}^{TOT}}{\alpha}\cdot T_{ref}\cdot\left(\frac{r_0}{r_{ref}}\right)^{\lambda} \qquad \text{(I-15)}$$

Equations (I-11) and (I-13)–(I-15) can then be combined to describe the equivalent conductivity as a function of the characteristic distance. A minimum conductivity value (K_{min}) is added since the derived relation otherwise would reach zero when L approaches the inverse of the total intensity:

$$K(L) = \begin{cases} K_c\cdot\left(\left(P_{32}^{TOT}\cdot L\right)^{\alpha} - 1\right) + K_{\min} & L \geq P_{32}^{TOT^{-1}} \\ \\ K_{\min} & L < P_{32}^{TOT^{-1}} \end{cases} \qquad \text{(I-16)}$$

I.5 Application to Task 8 conditions

The derived relations were applied to conditions representative for the BRIE experiment and Task 8. Parameters describing the fracture statistics for Task 8 (defined by Vidstrand et al. 2017, Table 8-1), were used in this analysis with: $r_0 = 0.25$, $k_r = 2.6$ and $P_{32}^{TOT} = 3.85$ (sum for three fracture sets). Correspondingly, parameters values for a relation between transmissivity and radius, similar to Equation (I-3), adopted by Follin et al. (2005), were used in this analysis with: $T_{ref} = 1.6\cdot10^{-11}$ (m²/s); $r_{ref} = 1$ m; and $\lambda = 2$. This was fairly similar to compiled empirical data presented by Vidstrand et al. (2017) (Figure I-2).

This parameter set results in the following values of the defined parameters in Equation (I-14) and (I-15): $\alpha = 2.33$ and $K_c = 1.65\cdot10^{-12}$ m/s. From these and an assumed K_{min} value of 10^{-13} m/s, an equivalent conductivity as function of the characteristic distance (Equation (I-16)) is evaluated and shown in Figure I-3. It can be noted that the function has the value of K_{min} for all distances lower that 0.26 m which is the inverse value of the total intensity P_{32}^{TOT} (from here on denoted the minimum characteristic distance L_0). Above this value, the equivalent conductivity increase rapidly with distance, for instance at 1 m the equivalent conductivity exceeds 10^{-11} m/s.

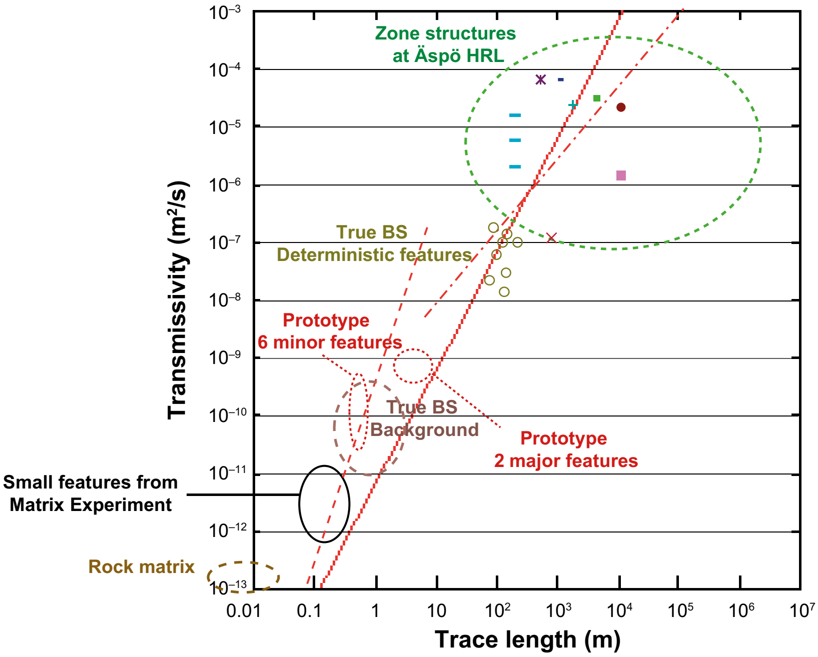

Figure I-2. *Transmissivity-trace length relations. Red solid line corresponds to the parameter set presented by Follin et al. (2005). The trace length was assumed to be π/2 times the fracture radius. The rest of the plot was presented by Vidstrand et al. (2017).*

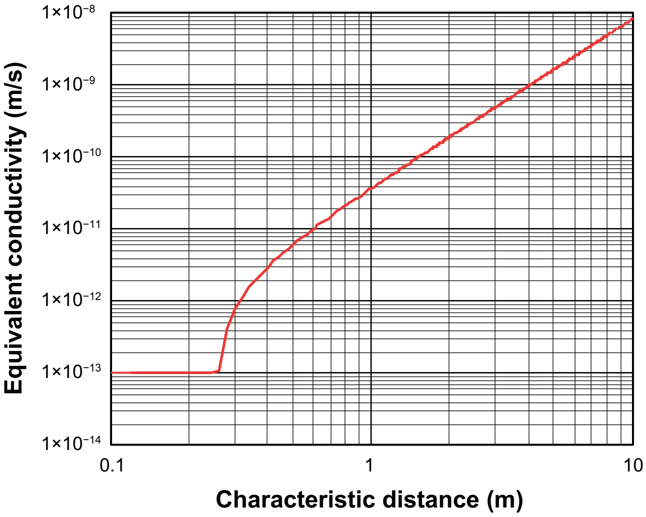

Figure I-3. *Equivalent conductivity as function of the characteristic distance.*

I.6 Pressure drawdown around borehole

In order to assess the relevance of the notion that the drawdown around a deposition hole can be disregarded at a specific distance from the hole, an analysis of radial flow is considered:

$$q = -\frac{2\pi \cdot r \cdot K}{\gamma} \cdot \frac{\partial P}{\partial r} \tag{I-17}$$

where γ is the unit weight of water (0.01 MPa/m), K is the hydraulic conductivity, and q is the flow rate per unit length at steady-state. It is obviously important that the scale-dependence of K in Equation (I-16) is addressed, and that the characteristic distance somehow increases with an increasing radius. In this analysis this is taken into account by equating the characteristic distance with the arc length (θ·r), where different angle values θ are analyzed. Even though an arc is a bent line, it make sense to use this quantity since what is needed is a conductivity value representative for a specific radius, and since the flow rate perpendicular to an arc at this radius should be closely related to the length of this arc. Three angle values are analyzed (Figure I-4, left): 2π, L_0/r_H and $L_0/(r_H+L_0)$. The first value represents the entire circumference and will give the highest conductivities and flow rates. The second value is defined so that the arc length at the hole radius (r_H) equals the minimum characteristic distance (L_0). The third value is defined so that the arc length at the radius r_H+L_0 (corresponding to a hollow cylinder close to the borehole with the thickness of L_0) equals the minimum characteristic distance. The last case implies a zone around the hole with the K_{min} conductivity value precisely throughout is thickness.

Equation (I-17) can be rearranged and integrated to calculate the flow rate per unit length at steady state by assuming an unaffected pressure level P_o at r_o and a zero pressure at the hole radius (Figure I-4, right):

$$q(\theta) = \frac{P_o}{\displaystyle\int_{r_H}^{r_o} \frac{\gamma}{2\pi \cdot K(\theta \cdot r) \cdot r} \cdot dr} \tag{I-18}$$

And with some further rearrangement a pressure profile can be calculated as:

$$P_i(r_i, \theta) = P_o - \frac{\displaystyle\int_{r_i}^{r_o} \frac{dr}{K(\theta \cdot r) \cdot r}}{\displaystyle\int_{r_H}^{r_o} \frac{dr}{K(\theta \cdot r) \cdot r}} \tag{I-19}$$

The relations for flow rates and pressure profiles (Equations (I-18 and (I-19) were applied to conditions representative for the BRIE experiment, which involves the K(L) relation shown in Figure I-3, a hole radius of 0.15 m, and an undisturbed pressure level of 1 MPa, for this calculation fixed at a radius of 1 000 m. The results are shown in Figure I-5. The flow rate per unit length generally range from 10^{-3} to a few ml/min/m. It can be noted that the flow rates measured in Hole 18 was 0.01–0.03 ml/min at 2.1–3.1 m depth and in Hole 17 it was 0.12–0.25 ml/min at 2.1–3.5 m depth. These flow rates are approximately equal or slightly higher than the calculated flow rate values for the cases with angles based on the L_0 values. The pressure profiles for the analyzed angles show that the drawdown is limited to a radius of 1 m. For the cases with angles based on the L_0 values, the pressures are unaffected beyond a radius of around 0.5 m (which is slightly more than r_H+L_0). It can be mentioned that the drawdown would be more extensive for angles smaller than those analyzed.

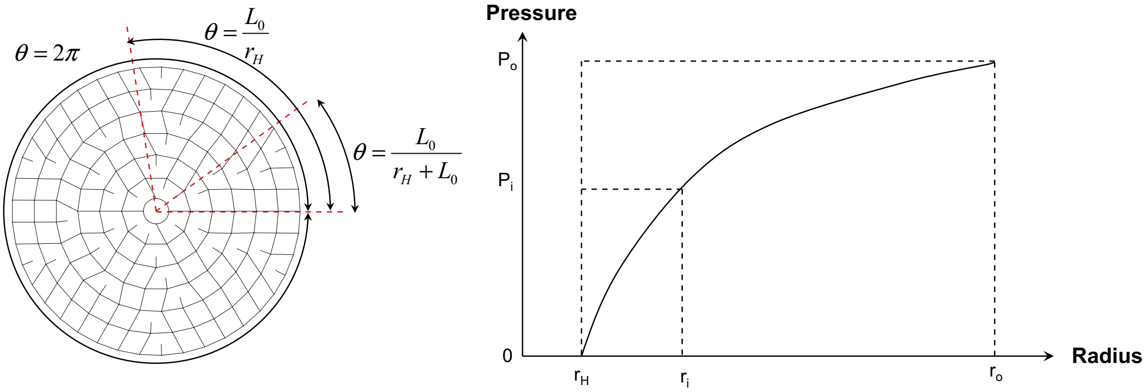

Figure I-4. *Schematic representation of fractured rock around a bore hole with different analyzed angles (left). Illustration of drawdown around a borehole (right).*

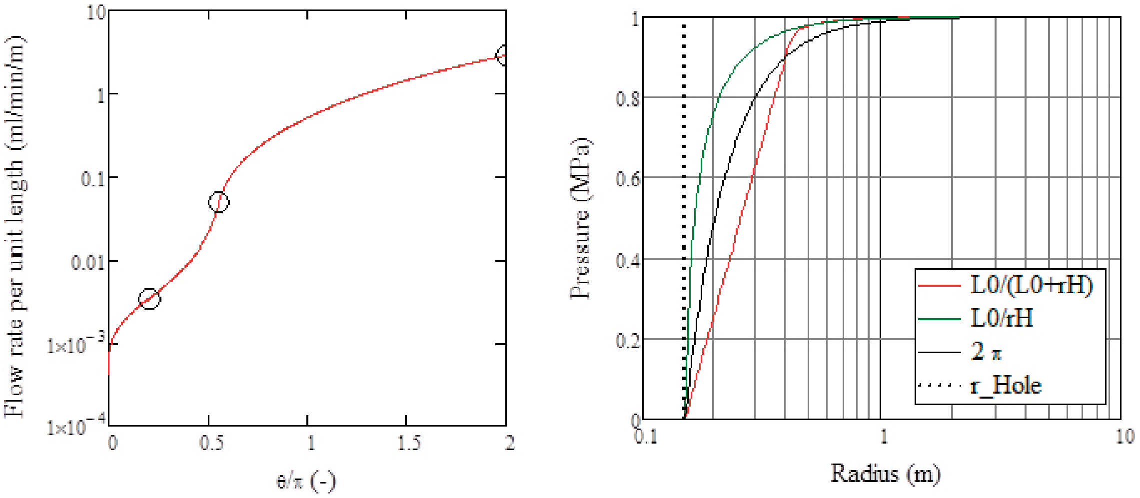

***Figure I-5.** Flow rate per unit length as a function of angle (left) and pressure profiles for analyzed angles.*

I.7 Discussion

It should be stressed that the presented analysis was based on several simplifications, and that the significance of these are difficult to assess. For instance, neither fracture orientation nor connectivity were taken into account, which could imply that the evaluated conductivities are over-estimated. Moreover, the analysis was based on the assumption that the derived relations for the equivalent conductivity and the characteristic distance are valid for the P_{32} intensity, even though they were derived for P_{10} intensities. Nevertheless, from the model realizations presented by Vidstrand et al. (2017) it was found that the evaluated P_{32} value was approximately only 70 % higher than the corresponding P_{10} value, and this may suggest that the impact of this simplification is limited.

The assessment of the drawdown around a borehole was based on the assumption that the characteristic distance can be equated with the arc length at a certain radius and for a certain angle and this approach can possibly be regarded as a way to account for the variability of the fracture network, where 2π represents a "homogenous" distribution of the network, whereas the smaller angles represents a more probable "heterogeneous" distribution. It should be noted that the equivalent conductivity can be regarded as an idealized mean value, and that both higher and lower values are possible in a certain volume. Finally, the drawdown assessment did not take any axial dimension into account for the quantification of the characteristic distance. Neither was any axial flow considered since this was simplification with pure radial flow.

Nevertheless, this analysis supports the notion that the drawdown around a deposition hole can be disregarded at a fairly small distance from the borehole. One of the most important parameters for the fracture set is the total intensity, which directly gives the minimum characteristic distance (L_0), which in turn appears to be the relevant thickness for a low permeability zone, intersected by permeable narrow paths or discs, close to a bore hole. Since this observation can be of importance for calculating the hydration time for the buffer and backfill in a repository, it is recommended that the results presented here will be compared with flow rates and drawdowns resulting from a regular DFN implementation of the provided fracture description.

Appendix J

Model overview

Table J-1. Overview of models presented as part of the Task 8 modelling done at Clay Technology.

Model ID	Model(s)	Geometry	Borehole(s)	Task	Date simulated	First presented	Date presented	Comment
T8AC1–C23	T8AC1–C23	8a def	Generic	8a	April–May 2011	EBS TF Meeting Barcelona	1/6-2011	Uncertainty analysis
T8C_1a	T8C1AC2A5	Large-scale	Inflow calib.	8c	9/11-2011	EBS TF Meeting Toronto	22/11-2011	Several models were used to calibrate the inflows in the boreholes, only the final one is reported here
T8C_1b	T8C1AD2	Large-scale	Inflow pred.	8c	10/11-2011	EBS TF Meeting Toronto	22/11-2011	Simplistic model to estimate the change in borehole inflow – Not realistic
T8C_2a		Intermediate scale	Generic	8c		EBS TF Meeting Toronto	22/11-2011	Thin-slice 3D geometry to model the evolution in a generic BRIE borehole (fracture characterization was not available)
T8C_2b		Intermediate scale	Generic	8c		EBS TF Meeting Toronto	22/11-2011	Thin-slice 3D geometry to model the evolution in a generic BRIE borehole (fracture characterization was not available)
T8D_1a	T8D_LS_NS_E3	Large-scale	17 and 18	8d	23/11-2012	EBS TF Meeting Lund	28/11-2012	Class B prediction of the RH evolution in borehole 17 and 18 (high matrix conductivity; 5×10^{-13} m/s)
T8D_1b	T8D_LS_NS_E7	Large-scale	17 and 18	8d	25/11-2012	EBS TF Meeting Lund	28/11-2012	Class B prediction of the RH evolution in borehole 17 and 18 (medium matrix conductivity; 1×10^{-13} m/s)
T8D_2a	T8D_LON_A2	Large-scale	17	8d	23/4-2013	EBS TF Meeting London	22/5-2013	Class B1 prediction of the evolution in borehole 17 (low matrix conductivity)
T8D_2b	T8D_KO0018_pred2	Large-scale	18	8d	19/2-2014	Report	7/3-2014	Class B1 prediction of the evolution in borehole 18 (low matrix conductivity, fracture flow added)
T8F_1	KO0018_BT_VF3	Local-scale	18	8f	28/11-2014	EBS TF Meeting Berkeley	11/12-2014	Class C prediction of the evolution in borehole 18 (additional vertical fracture included)